

Dissertation zur Erlangung des Doktorgrades  
der Fakultät für Chemie und Pharmazie  
der Ludwig-Maximilians-Universität München

# Single Molecule Spectroscopy on Native and Reconstituted Peridinin-Chlorophyll-Protein Light-Harvesting Complexes

Stephan Wörmke  
aus  
Flensburg

2008



---

## Erklärung

---

Diese Dissertation wurde im Sinne von §13 Abs. 3 bzw. 4 der Promotionsordnung vom 29. Januar 1998 von Prof. Dr. C. Bräuchle betreut.

### **Ehrenwörtliche Versicherung**

Diese Dissertation wurde selbstständig, ohne unerlaubte Hilfe erarbeitet.

München, den 23.6.2008

Stephan Wörmke

Dissertation eingereicht am 23.6.2008

1. Gutachter: Prof. Dr. C. Bräuchle

2. Gutachter: Prof. Dr. H. Scheer

Mündliche Prüfung am 17.7.2008



## Meinen Eltern

Come, my friends,  
'T is not too late to seek a newer world.  
Push off, and sitting well in order smite  
The sounding furrows; for my purpose holds  
To sail beyond the sunset, and the baths  
Of all the western stars, until I die.  
It may be that the gulfs will wash us down:  
It may be we shall touch the Happy Isles,  
And see the great Achilles, whom we knew.  
Tho' much is taken, much abides; and tho'  
We are not now that strength which in old days  
Moved earth and heaven, that which we are, we are;  
One equal temper of heroic hearts,  
Made weak by time and fate, but strong in will  
To strive, to seek, to find, and not to yield.

from Ulysses by Alfred Lord Tennyson



---

# Contents

---

1	Introduction	1
2	Single Molecules and Spectroscopy	5
2.1	Photophysics of Single Molecules	5
2.1.1	Dipole Approximation	6
2.1.2	Radiative Properties of an Emitting Dipole	6
2.1.3	Lifetimes and Decay Rates	8
2.1.4	Frequency Shifts and Spectral Dynamics	9
2.2	Dipole-Dipole Interactions and Energy Transfer	9
2.2.1	A Dimer Model	9
2.2.2	Strong Interaction and Excitons	10
2.2.3	Weak Interaction and Förster Energy Transfer	12
2.3	Principles of Fluorescence	14
2.3.1	Excitation	14
2.3.2	Fluorescence Emission	15
2.4	Principles of Single Molecule Microscopy	17
2.5	Experimental Techniques	20
2.5.1	Confocal Microscopy	20
2.5.2	Wide-field Microscopy	23
2.5.3	Comparison	23
3	Photosynthesis and the Peridinin Chlorophyll Protein	25
3.1	Oxygenic Photosynthesis	25
3.2	Light-Harvesting Antennae	27
3.3	Building Blocks of PCP Antennae	28
3.3.1	Chlorophylls	28
3.3.2	Peridinin - the Major Pigment in PCP	31
3.4	Peridinin Chlorophyll Protein (PCP)	34
3.4.1	PCP Structure	34
3.4.2	Reconstitution of PCP	34
3.4.3	Steady-State Spectroscopy	35
3.5	Energy Transfer Pathways in PCP	37
3.5.1	Peridinin to Chlorophyll Energy Transfer	38

---

3.5.2	Chlorophyll to Chlorophyll Energy Transfer	39
3.6	Conclusion	40
4	Materials and Methods	43
4.1	Reconstitution of PCP	43
4.1.1	Extraction and Purification of N-domain Apoprotein	43
4.1.2	Materials for Reconstitution	44
4.1.3	Homo- and Hetero-Chlorophyllous Reconstitution	44
4.1.4	Atomic Coordinates	45
4.2	Sample Preparation	45
4.2.1	List of Chemicals	45
4.2.2	Preparation	45
4.2.3	Cover Slips and Silver Island Films	45
4.3	Ensemble Spectroscopy	47
4.3.1	Absorption	47
4.3.2	Fluorescence Spectra and Lifetimes	47
4.4	Single Molecule Spectroscopy	48
4.4.1	Confocal Setup	48
4.4.2	Wide-field Setup	49
4.5	Excitation Schemes	50
5	Spectroscopy of Homo-Chlorophyllous PCP	53
5.1	Ensemble Spectroscopy	53
5.1.1	Absorption and Circular Dichroism	53
5.1.2	Fluorescence Emission Spectra	55
5.1.3	Fluorescence Excitation Spectra	55
5.1.4	Fluorescence Lifetime and Quantum Yield	57
5.2	Single Molecule Spectroscopy	58
5.2.1	Native PCP	59
5.2.2	Homo-Chlorophyllous N-PCP	59
5.3	Stepwise Photobleaching	61
5.4	Polarisation-resolved SMS	66
5.5	Solvent Effects on Stability	67
5.6	Protein-Pigment Interaction	71
5.7	Conclusion	74
6	Spectroscopy of Hetero-Chlorophyllous N-PCP	75
6.1	Ensemble Spectroscopy	75
6.1.1	Absorption and Circular Dichroism	76
6.1.2	Fluorescence Emission Spectra	77
6.1.3	Fluorescence Excitation Spectra	78
6.2	Energy Transfer between Chlorophylls	81
6.3	Single-Molecule Spectroscopy	82
6.4	Simulation of Chl-Chl Energy Transfer	86

---

6.5	Conclusion	88
7	PCP at the Interface of Metallic Nanostructures	89
7.1	Metal Nanoparticles	89
7.2	Fluorophore Metal Interactions	92
7.2.1	Local Field Enhancement	95
7.2.2	Metal-Dipole Interaction	96
7.2.3	Enhancement of Radiative Rate	97
7.3	Single PCP Complexes on SIF	98
7.4	Ensemble Characterisation	101
7.5	Enhancement Mechanism	102
7.6	Conclusion	106
8	Summary and Conclusions	107
	Bibliography	111
A	Miscellaneous	121
A.1	Source Code	121
A.1.1	Förster Energy Transfer	121
A.1.2	Monte Carlo Simulation	122
A.2	List of Publications	123
A.3	Contributions to Conferences and Seminars	124
A.4	Lebenslauf	126



# CHAPTER 1

---

## Introduction

---

The sun's energy is the source of life on Earth. More than three billion years ago, long before any green plants appeared on our planet, certain cyanobacteria invented photosynthesis to drive their life processes. Ever since these days evolution has optimised strategies and developed means to form a highly efficient photosynthesis apparatus found in many variations in organisms like green plants, bacteria and algae. The conversion of mainly visible light into chemical energy is carried out by a vast and complex machinery. This remarkable process, directly or indirectly, provides the foundation of all life and has profoundly altered the geology of Earth itself [1]. Early research on photosynthesis tried to understand the exact nature of the basic building blocks behind these processes. The characteristic green colour of plants is testimony to a key role of chlorophylls. Other, more hidden, participating molecules are carotenoids giving rise to the red and yellow colours of plants as in some fruits and vegetables. Such molecules that absorb light and impart colour to living matter and other materials are called pigments. In 1932 Emerson and Arnold conducted experiments on certain algae with a home-built flashlamp [2, 3]. They have shown that after each flash, the algae produced some amount of oxygen. However, it turned out that some 2500 chlorophyll molecules are involved to produce just a single oxygen atom. The true significance of these experiments became clear only at later time. Today it is known that photosynthesis relies on pigment-proteins, so called light-harvesting antenna-systems, constituted of pigments like chlorophylls and carotenoids. Such complexes efficiently capture sunlight and transport it to central reaction centres where photochemistry takes place and the photosynthetic conversion of energy is initiated. Many experimental and theoretical methods of biology, chemistry and physics have been employed to explain the molecular basis behind the efficient operation associated with photosynthetic building blocks. A recurring central question was how their structure relates to their function.

High-resolution crystal structures strongly stimulated experimental and theoretical investigations on photosynthesis. The Nobel prize for chemistry in 1988 was awarded to Deisenhofer, Huber and Michel for the determination of the three-dimensional structure of a photosynthetic reaction centre [4, 5]. In 1995 Cogdell *et al.* solved the structure of the peripheral light-harvesting complex 2 (LH2) [6]. Today many such structures are known and provide a

detailed atomic basis to understand photosynthesis. In 1996 Hofmann *et al.* solved the crystal structure of the light-harvesting antenna that is at the heart of this thesis [7]: the peridinin chlorophyll protein (PCP), a water-soluble complex found in the marine dinoflagellate *Amphidinium carterae*. These algae live in the oceans at some metres below the sea-level. At such depths most of the red part of the sun's spectrum is filtered away, leaving only green-blue light. PCP features a broad absorption in the spectral window ranging from 450 to 550 nm that is mostly attributable to its main light-harvesting pigment: the highly-substituted carotenoid peridinin. In this respect PCP is unique as carotenoids only in few cases play an active role in light-harvesting. In most other antennae, however, they are indispensable to photoprotection strategies. In its native structure PCP is a trimer comprised of three monomeric subunits. In each of these subunits two clusters of four peridinins are bound. These are in van der Waals contact to another central pigment of PCP: chlorophyll *a*. Chlorophyll molecules exist in slightly different chemical structures in various photosynthetic organisms, e.g. as chlorophyll *a* in plants or algae, and as bacteriochlorophyll *a* or *b* in photosynthetic bacteria. The two chlorophylls *a* in a single monomer feature a distance of 17.4 Å, distances between chlorophylls *a* in different monomers range from 40 to 54 Å. All pigments are enclosed in a hydrophobic protein cavity.

Crystal structures provide the basis to understand how energy is transported to the reaction centres after initial absorption by a light-harvesting antenna. Energy transfer processes are central to the function of these complexes. Pigment molecules like chlorophyll and carotenoids are excited by light into energetically higher electronic states. Such states decay via fluorescence or other means if no neighbouring pigment is in their close vicinity. However, the crystal structures indicate that the pigments bound in light-harvesting complexes are just a few nanometers apart and thus, could serve as donors and acceptors of the excitation energy. Energy transfer was described theoretically by the work of Förster in 1948 [8]. He showed that energy transfer crucially depends on distance and relative orientations of the pigment molecules, as well as on spectral overlap of fluorescence and absorption spectra of donor and acceptor, respectively. The protein cavities provide a stable environment, in which the pigments are arranged such to yield fast and efficient energy transfer pathways. Furthermore, the spectral overlap between donor and acceptor pigments imparts an energetic directionality and excitation is funnelled down in the energetically favourable direction. For example, in PCP the excitation by green-blue light is transported to the central chlorophylls by energy transfer from the peridinins. After usually some energy transfer steps energy is finally funnelled down to the reaction centres. However, crystal structures feature only static information. In order to gain a deeper understanding of how pigment-protein complexes harvest light so efficiently, it is necessary to employ spectroscopic tools that directly reveal the dynamics and efficiency of energy transfer and the nature of the excited energy states associated with the pigments.

Spectroscopy, in general, allows to determine parameters that describe the electronic structure of light-harvesting antennae [9, 10]. However, even isolated complexes, as they are studied in this thesis, are rather complex systems and on many such examples it has been proven difficult to analyse the excited state properties in detail. This is mainly due to the vast number of atoms bound in pigment-protein complexes that easily extend to 32 kDa in the case of PCP and impart

pronounced disorder. In recent years such difficulties have been overcome by single molecule spectroscopy [11–13]. The advantage of this technique is that it allows to measure spectral properties of individual complexes. Many such measurements yield distributions of spectral observables that clearly contain more information than just average values obtainable by conventional ensemble spectroscopy. Another important advantage is that in single molecule spectroscopy there is no need for synchronisation. Thus, dynamical processes can be followed over time. Single molecules undergo a temporal development of different states but are at any time in a distinct, well-defined state. Recording the whole sequence of steps allows for identification of short-lived intermediate states that might be essential for the function of the molecule but would be completely masked in ensembles. These advantages render single molecule spectroscopy a valuable tool that extends and complements conventional spectroscopy.

In less than an hour more radiation hits our planet than is consumed by mankind in a whole year. The highly efficient machinery that is behind photosynthesis has triggered interest to employ sunlight to solve our future energy needs. Much research has started in recent years aiming to copy the successful mechanisms into artificial photosynthetic systems. The development is parallel with the advent of metal nanoparticles that feature unique optical properties [14, 15]. These are the result of plasmonic resonances or collective oscillations of electrons associated with the surface of these particles. Research showed that chromophores placed in close vicinity to silver and gold nanoparticles experience enhanced local fields and alter radiative and non-radiative properties [16]. Hybrid-structures constituted of light-harvesting systems and metal nanoparticles could be used to mimic photosynthesis and resemble the high efficiency found in the native systems for technological applications. A first attempt to combine the light-harvesting complex PCP with silver nano islands was achieved in this thesis. Controlled nanofabrication promises to construct hybrid systems that could be used in future solar cells.

## Synopsis

This thesis presents the results of ensemble and single molecule spectroscopy obtained for a light-harvesting complex, PCP. The spectroscopic studies were aided by the ability to make systematic alterations in the structures of PCP by reconstitution with chlorophylls. This allowed to examine how these structural changes manifest themselves in the spectroscopic observables and dynamics of energy transfer. In particular, in close collaboration with the group of Prof. H. Scheer (Department of Biology, LMU), experiments were conducted on native and reconstituted PCP samples containing two alike chlorophylls or two different chlorophylls in a single complex. Chapter 2 establishes the theoretical framework, in which all spectral changes are interpreted. These involve interactions among the chlorophylls and the protein, energy transfer between peridinin and chlorophylls, as well as between chlorophylls. The experimental techniques used to measure these effects are introduced. Chapter 3 provides a short introduction to photosynthesis with a focus on PCP and its main pigments. It concludes with an overview of recent literature on PCP. Chapter 4 discusses the experimental details of reconstitution, the

experimental setups and sample preparation. Chapter 5 and 6 present the results on PCP reconstituted with two alike chlorophylls and mixtures of different chlorophylls, respectively. Chapter 7 highlights how the spectral properties of PCP are externally altered by plasmonic interactions to silver nanoparticles in close vicinity to the complexes.

# CHAPTER 2

---

## Single Molecules and Spectroscopy

---

In recent years single molecule spectroscopy (SMS) and microscopy provided a wealth of information about the behaviour of single molecules in complex nanoscale environments. The observation of individual molecules extend and complement conventional ensemble techniques. It removes ensemble averaging and allows for construction of histograms of spectral properties. Such distributions contain much more information than available through recording average values. Furthermore, in SMS there is no need for synchronisation while time-dependent processes can be studied molecule by molecule. SMS has had a major impact on such diverse areas as physics, chemistry, material science and biology and has been subject to numerous reviews [17–21].

In this thesis, experiments on single light-harvesting complexes are presented. The studied effects include dipole interactions and energy transfer between the pigments as well as metal enhanced fluorescence of the pigments. Section 2.1 presents a theoretical framework that describes the above-mentioned effects. The first application follows in Section 2.2 which targets dipole-dipole interactions and energy transfer. Single molecules are probed by tuning a laser into an electronic transition resonant with the excitation wavelength. The resulting fluorescence is a measure of the properties of individual molecules. The principles of fluorescence are briefly discussed in Section 2.3. Detection of single molecules has to be achieved in the presence of billions of solvent molecules and experimental noise. This is realised by microscopy methods whose basic principles and experimental implementations are discussed in Sections 2.4 and 2.5, respectively.

### 2.1 Photophysics of Single Molecules

This section presents a theoretical framework (after [22]) describing the processes studied in this thesis, i.e. energy transfer, pigment-pigment interactions and metal enhanced fluorescence (MEF). For this purpose a classical approach based on electrodynamics is used whenever possible. For that matter, a single molecule that is small compared to the wavelength

is represented by discrete and spatially separated charges giving rise to a charge density

$$\rho(\mathbf{r}) = \sum_n q_n \delta[\mathbf{r} - \mathbf{r}_n] \quad (2.1)$$

and current density

$$\mathbf{j}(\mathbf{r}) = \sum_n q_n \dot{\mathbf{r}}_n \delta[\mathbf{r} - \mathbf{r}_n], \quad (2.2)$$

where  $\mathbf{r}_n$  denotes the position vector of the  $n$ th charge and  $\dot{\mathbf{r}}_n$  its corresponding velocity.

### 2.1.1 Dipole Approximation

A molecule undergoes interactions with its environment, e.g. an incident laser excitation field or a nearby molecule, which are represented by an electromagnetic field  $\mathbf{E}_{\text{inc}}$ . The corresponding electric potential of the charge distribution reads

$$V_E = - \int \mathbf{P} \cdot \mathbf{E}_{\text{inc}} dV, \quad (2.3)$$

where  $\mathbf{P}$  denotes the polarisation of the molecule [23]. In general, this potential features a complicated hyper-surface but can be expanded using a Taylor series of  $\mathbf{E}_{\text{inc}}$  at the centre of the charge distribution  $\mathbf{r} = 0$ . For the sake of this thesis it is sufficient to only keep the second term in that series and the electric potential simply reads

$$V_E = -\boldsymbol{\mu} \cdot \mathbf{E}_{\text{inc}}(0), \quad (2.4)$$

where  $\boldsymbol{\mu}$  corresponds to the electric dipole moment

$$\boldsymbol{\mu} = \sum_n q_n \mathbf{r}_n \quad \text{or} \quad \boldsymbol{\mu} = \int \rho(\mathbf{r}') (\mathbf{r}' - \mathbf{r}) dV'. \quad (2.5)$$

Higher order terms are omitted as they strongly depend on field gradients. However, throughout this thesis it is assumed that electric fields are sufficiently homogeneous on the scale of particles involved and thus gradients vanish. This *dipole approximation* leads to a set of selection rules encountered in optical spectroscopy and are discussed later.

### 2.1.2 Radiative Properties of an Emitting Dipole

The preceding section has established that any charge neutral system, like a molecule, that is smaller than the wavelength of the interacting radiation, can be treated to first order approximation as a dipole. Consequently the optical properties are described in classical terms based on the radiating dipole approximation as well. In a homogeneous, linear and isotropic

space the radiation properties of a dipole are derived from a harmonically oscillating current density  $\mathbf{j}(\mathbf{r}, t)$  that reads

$$\mathbf{j}(\mathbf{r}, t) = \frac{d}{dt} \boldsymbol{\mu}(t) \delta[\mathbf{r} - \mathbf{r}_0] = -i\omega \boldsymbol{\mu} \delta[\mathbf{r} - \mathbf{r}_0]. \quad (2.6)$$

An elegant way to derive the field of such a dipole is realised by Green's function  $\mathbf{G}(\mathbf{r}, \mathbf{r}_0)$ . Essentially,  $\mathbf{G}$  is defined by the electric field at the field point  $\mathbf{r}$  generated by an oscillating dipole located at some origin at  $\mathbf{r}'$  [22]. The electric field is

$$\mathbf{E}(\mathbf{r}) = \omega^2 \mu_0 \mathbf{G}(\mathbf{r}, \mathbf{r}_0) \boldsymbol{\mu} = \frac{1}{4\pi\epsilon_0} (3(\boldsymbol{\mu} \cdot \mathbf{n})\mathbf{n} - \boldsymbol{\mu}) \frac{1}{r^3}, \quad (2.7)$$

where  $\mathbf{n}$  denotes the norm along the dipole vector. The oscillating dipole field radiates a power equal to  $P(t)$ . It is determined by integration over the Poynting vector  $\mathbf{S}(\mathbf{E}, \mathbf{B})$ , a quantity that describes the density and direction of energy transport associated with an electromagnetic wave. Thus,

$$P(t) = \int_{\partial V} \mathbf{S}(t) \cdot \mathbf{n} \, da = \frac{1}{4\pi\epsilon_0\epsilon} \frac{2n^3}{3c^3} \left[ \frac{d^2}{dt^2} |\boldsymbol{\mu}(t)|^2 \right]. \quad (2.8)$$

Averaged over time a harmonically oscillating dipole radiates the power equal to

$$\bar{P} = \frac{1}{4\pi\epsilon_0\epsilon} \frac{n^3 \omega^4}{3c^3} |\boldsymbol{\mu}|^2. \quad (2.9)$$

In general, a dipole is situated in an inhomogeneous environment, in which for example a nearby acceptor molecule or nanoparticle is placed. Following Poynting's theorem the radiating dipole experiences some means of energy dissipation. In a linear medium the rate of dissipation for a harmonically oscillating dipole yields

$$\frac{dW}{dt} = -\frac{1}{2} \int_V \text{Re} \{ \mathbf{j}^* \cdot \mathbf{E} \} \, dV = \frac{\omega}{2} \text{Im} \{ \boldsymbol{\mu}^* \cdot \mathbf{E}(\mathbf{r}_0) \}, \quad (2.10)$$

where  $\mathbf{E}(\mathbf{r}_0)$  corresponds to the electric field at the dipole's origin. In inhomogeneous environments  $\mathbf{E}(\mathbf{r}_0)$  does not simply correspond to the dipole field  $\mathbf{E}_0(\mathbf{r}_0)$  alone but is rather composed of additional contributions  $\mathbf{E}_s(\mathbf{r}_0)$  accounting for environmental influences. Thus, the dipole experiences the overall field

$$\mathbf{E}(\mathbf{r}_0) = \mathbf{E}_0(\mathbf{r}_0) + \mathbf{E}_s(\mathbf{r}_0). \quad (2.11)$$

In classical terms  $\mathbf{E}_s(\mathbf{r}_0)$  corresponds to the field back-scattered by the environment but can be identified to be the local field inside a protein cavity or the plasmon induced field of a nearby nanoparticle. Using  $k = \omega/c$  and Equation (2.9) the normalised rate of energy dissipation

reads

$$\frac{P}{P_0} = 1 + \frac{6\pi\epsilon_0\epsilon}{|\boldsymbol{\mu}|^2} \frac{1}{k^3} \text{Im} \{ \boldsymbol{\mu}^* \cdot \mathbf{E}_s(\mathbf{r}_0) \}. \quad (2.12)$$

In other words, the change of energy dissipation depends on the secondary field defined by the environment the dipole is embedded in.

### 2.1.3 Lifetimes and Decay Rates

An excited state of a molecule decays after a characteristic average time  $\tau_0$ , the so called lifetime. In the classical picture this situation corresponds to an undriven harmonical oscillator damped with a damping constant  $\gamma_0$ . The lifetime is defined as the time after which the energy of the oscillator has decayed to  $1/e$  of its initial value at time  $t = 0$  and thus

$$\tau_0 = \frac{1}{\gamma_0}. \quad (2.13)$$

In a homogeneous environment, conservation of energy demands that the decrease in oscillator energy equals the energy losses, i.e.

$$\overline{W}(t=0) - \overline{W}(t) = q_i \int_0^t P_0(t') dt'. \quad (2.14)$$

The parameter  $q_i$  is a measure for the energy loss due to radiation and is called intrinsic quantum yield. It holds values from 0 to 1, the latter corresponding to the situation where all oscillator energy is dissipated by radiation. From a quantum mechanical point of view  $\gamma_0$  corresponds to the spontaneous decay rate and is defined by the density of states of the quantum system  $\rho$  [22], i.e.

$$\gamma = \frac{2\omega_0}{3\hbar\epsilon_0} |\boldsymbol{\mu}|^2 \rho(\mathbf{r}_0, \omega_0). \quad (2.15)$$

In an inhomogeneous environment the oscillating dipole experiences the field  $\mathbf{E}_s$  scattered from the environment which acts as a driving force. In a similar fashion to Equation (2.12) the change in decay rate is expressed as

$$\frac{\gamma}{\gamma_0} = 1 + q_i \frac{6\pi\epsilon_0\epsilon}{|\boldsymbol{\mu}|^2} \frac{1}{k^3} \text{Im} \{ \boldsymbol{\mu}^* \cdot \mathbf{E}_s(\mathbf{r}_0) \} \quad (2.16)$$

which is identical to Equation (2.12) except for the quantum yield  $q_i$ . If  $q_i = 1$  it follows

$$\frac{\gamma}{\gamma_0} = \frac{P}{P_0}. \quad (2.17)$$

This relation is a starting point in deriving energy transfer rates and modelling metal enhanced fluorescence presented in Chapter 7.

### 2.1.4 Frequency Shifts and Spectral Dynamics

Interactions of the molecule with its local environment cause frequency shifts of  $\Delta\omega = \omega - \omega_0$ . In the framework of the preceding discussion an expression for the normalised frequency shift reads

$$\frac{\Delta\omega}{\gamma_0} = q_i \frac{3\pi\epsilon_0}{|\boldsymbol{\mu}|^2} \frac{1}{k^3} \text{Re} \{ \boldsymbol{\mu}_0^* \cdot \mathbf{E}_s \}. \quad (2.18)$$

Such fluctuations manifest themselves in distance changes of a chromophore to neighbouring molecules and give rise to spectral dynamics represented by gradual spectral drifts or abrupt jumps of absorption and emission resonances. As a consequence spectral profiles are inhomogeneously broadened [18]. Such effects are frequently observed in proteins. For a detailed discussion see [24, 25].

## 2.2 Dipole-Dipole Interactions and Energy Transfer

The optical properties of protein-pigment complexes found in photosynthesis are strongly influenced by interactions between the pigments. Energy transfer is central to the function of light-harvesting complexes and a consequence of dipole-dipole interaction. Two limits are distinguished: strong interaction which leads to formation of excitons and weak interaction leading to Förster-type energy transfer.

### 2.2.1 A Dimer Model

The simplest system for which effects of energy transfer can be considered is a dimer of two interacting molecules A and B [22]. Both molecules are represented by two-level systems of fixed orientations separated by a distance  $\mathbf{R} = \mathbf{r}_B - \mathbf{r}_A$ . In absence of any interactions between the molecules, ground state and energy eigenvalue of A are  $|A\rangle$  and  $E_A$ , in the corresponding excited state  $|A^*\rangle$  and  $E_A^*$ , respectively. A similar notation holds for B as well. The system can be in any of the four states  $|AB\rangle$ ,  $|A^*B\rangle$ ,  $|AB^*\rangle$  or  $|A^*B^*\rangle$ .

Energy transfer exists by virtue of intermolecular interactions, among which electrostatic are by far the most dominant ones. The two molecules A and B feature charge densities  $\rho(\mathbf{r}_A)$  and  $\rho(\mathbf{r}_B)$ , respectively. These undergo Coulomb interactions

$$V_{AB}(\mathbf{r}) = \frac{1}{4\pi\epsilon_0} \iint \frac{\rho_A(\mathbf{r}')\rho_B(\mathbf{r}'')}{|\mathbf{r}' - \mathbf{r}''|} dV' dV''. \quad (2.19)$$

Within the dipole approximation the dipole-dipole term from a multipolar expansion series reads

$$V_{AB}(\mathbf{R}) = \frac{1}{4\pi\epsilon_0} \left[ \frac{R^2 \boldsymbol{\mu}_A \cdot \boldsymbol{\mu}_B - 3(\boldsymbol{\mu}_A \cdot \mathbf{R})(\boldsymbol{\mu}_B \cdot \mathbf{R})}{R^5} \right] \quad (2.20)$$

and determines to a large extent the properties of the interacting molecules and their respective energy transfer. Thus, interaction crucially depends on distance and relative orientation between the dipoles.

## 2.2.2 Strong Interaction and Excitons

In the dimer, the two individual molecules couple via dipole-dipole interaction. The Schrödinger equation of the dimer includes, in addition to the molecular Hamiltonian operators  $\hat{H}_A$  and  $\hat{H}_B$ , an interaction term  $\hat{V}_{AB}$  and reads

$$[\hat{H}_A + \hat{H}_B + \hat{V}_{AB}] |\Phi_n\rangle = E_n |\Phi_n\rangle, \quad (2.21)$$

where  $|\Phi_n\rangle$  denotes the wavefunction of the  $n$ th state. The corresponding energy eigenvalues are defined by

$$E_n = \langle \Phi_n | \hat{H}_A + \hat{H}_B + \hat{V}_{AB} | \Phi_n \rangle \quad (2.22)$$

and are derived in the following. However,  $|A\rangle$  and  $|B\rangle$  are no longer valid eigenstates in the dimer and consequently eigenenergies are different as well. The intermolecular interactions  $V_{AB}$  give rise to perturbations of the energy spectrum. Following first order non-degenerate perturbation theory [26, 27] ground and doubly excited state can be written as products of the molecular eigenfunctions [28]

$$|0\rangle = |AB\rangle = |A\rangle|B\rangle, \quad (2.23)$$

$$|2\rangle = |A^*B^*\rangle = |A^*\rangle|B^*\rangle, \quad (2.24)$$

leading to corrected energy eigenstates

$$E_0 = E_A + E_B + \langle 0 | V_{AB} | 0 \rangle, \quad (2.25)$$

$$E_2 = E_{A^*} + E_{B^*} + \langle 2 | V_{AB} | 2 \rangle. \quad (2.26)$$

Thus, coupling between A and B gives rise to displacement of ground state energy and energy of the doubly excited state as well. Treatment of the singly excited states, i.e.  $|1^+\rangle$  and  $|1^-\rangle$ , cannot proceed the same way and demands application of degenerate perturbation theory [22]. In the coupled dimer singly excited states are linear combinations of the unperturbed

states and read

$$|1^+\rangle = \cos \alpha |A^*B\rangle + \sin \alpha |AB^*\rangle = \cos \alpha |A^*\rangle|B\rangle + \sin \alpha |A\rangle|B^*\rangle, \quad (2.27)$$

$$|1^-\rangle = \sin \alpha |A^*B\rangle - \cos \alpha |AB^*\rangle = \sin \alpha |A^*\rangle|B\rangle - \cos \alpha |A\rangle|B^*\rangle, \quad (2.28)$$

where  $\alpha$  is an arbitrary parameter. Thus, the excited states of the coupled system are either on one of the two molecules only or on both of them. The relative contributions of the initial states are given by the coupling parameter  $\alpha$  which reads

$$\tan 2\alpha = \frac{2\text{Re} \{ \langle A^*B | V_{AB} | AB^* \rangle \}}{[E_{A^*} + E_B + W_{A^*B}] - [E_A + E_{B^*} + W_{AB^*}]} = \frac{2V}{\Delta E - \delta E}, \quad (2.29)$$

using the abbreviations  $W_{A^*B} \equiv \langle A^*B | V_{AB} | A^*B \rangle$  and  $W_{AB^*} \equiv \langle AB^* | V_{AB} | AB^* \rangle$ . The term  $V$  describes the interaction between the coupled molecules and reads  $V = \text{Re} \{ \langle A^*B | V_{AB} | AB^* \rangle \}$  and  $\delta E \equiv W_{A^*B} - W_{AB^*}$ , and  $\Delta E \equiv |(E_{A^*} + E_B) - (E_A + E_{B^*})|$ .

Both states  $|1^+\rangle$  and  $|1^-\rangle$  need to satisfy the Schrödinger Equation (2.22). The energy eigenvalues are a function of the coupling parameter  $\alpha$ . If  $\alpha=0$ , the singly excited states are reduced to  $|1^+\rangle = |A^*B\rangle$  and  $|1^-\rangle = |AB^*\rangle$  and thus excitation is localised completely on either A or B. This is also apparent from the energy eigenvalues yielding

$$E_1^+ = [E_{A^*} + E_B + W_{A^*B}], \quad (2.30)$$

$$E_2^- = [E_A + E_{B^*} + W_{AB^*}]. \quad (2.31)$$

A similar case is realised for  $\alpha = \pi/2$  for which roles of A and B simply switch. These limiting cases are referred to as the *weak coupling regime* and energy transfer is described in terms of Förster theory. A weakly coupled dimer is often called an incoherent exciton [29].

However, if  $\alpha = \pi/4$  (resonant case), excitation is distributed equally over both particles. The energy eigenvalues reflect this situation as well and read

$$E_1^\pm = \frac{1}{2} [E_A + E_{A^*} + E_B + E_{B^*} + W_{AB^*} + W_{A^*B}] \pm V. \quad (2.32)$$

Delocalised excitation occurs in the *strong coupling regime* and the dimer is called a coherent or Frenkel exciton.

Generally, the coupling parameter  $\alpha$  characterises the interaction regimes. However, it is more intuitive to use the coupling energy  $V$  itself as a measure. If  $V \gg \delta V \geq \Delta E$  the molecules A and B are strongly coupled,  $V$  is on the order of  $> 100 \text{ cm}^{-1}$ . If  $V \gg \delta V \geq \Delta E$  they are weakly coupled and  $V < 100 \text{ cm}^{-1}$ . Förster energy transfer and the exciton concept are the two limiting cases of energy transfer [30].

### 2.2.3 Weak Interaction and Förster Energy Transfer

In a weakly coupled dimer energy transfer occurs between two particles D (donor) and A (acceptor), each represented as a two level system. The donor is initially in its excited state at energy  $E_D = \hbar\omega_0$ . Donor and acceptor feature the transition dipole moments  $\boldsymbol{\mu}_D$  and  $\boldsymbol{\mu}_A$ , as well as unit vectors in the direction of these dipoles  $\mathbf{n}_D$  and  $\mathbf{n}_A$ , respectively.  $\mathbf{R} = \mathbf{r}_B - \mathbf{r}_A$  is the vector from donor to acceptor. Within the classical dipole approximation model Equation (2.17) provides the starting point to derive the rate of energy transfer between donor and acceptor  $\gamma_{D \rightarrow A}$ , i.e. the following relation holds:

$$\frac{\gamma_{D \rightarrow A}}{\gamma_0} = \frac{P_{D \rightarrow A}}{P_0}, \quad (2.33)$$

where  $\gamma_0$  denotes the decay rate in absence of the acceptor. From a classical point of view the donor constitutes an oscillating dipole at frequency  $\omega_0$  thereby radiating the overall power  $P_0$  which was derived already in Equation (2.9). The acceptor absorbs that radiation at  $\omega_0$  and the fraction of donor energy absorbed by the acceptor per unit time is denoted as  $P_{D \rightarrow A}$ . Thus, since expressions for  $\gamma_0$  and  $P_0$  are already known, in order to derive the rate of energy transfer the problem is reduced to find an expression for  $P_{D \rightarrow A}$ .

The above-mentioned Poynting theorem provides a way to describe the power transferred from donor to acceptor. In general terms, the electric field of the donor  $\mathbf{E}_D$  interacts with the acceptor's dipole moment and, similar to Equation (2.10), dissipates the energy

$$P_{D \rightarrow A} = \frac{\omega_0}{2} \text{Im} \{ \boldsymbol{\mu}_A^* \cdot \mathbf{E}_D(\mathbf{r}_A) \}. \quad (2.34)$$

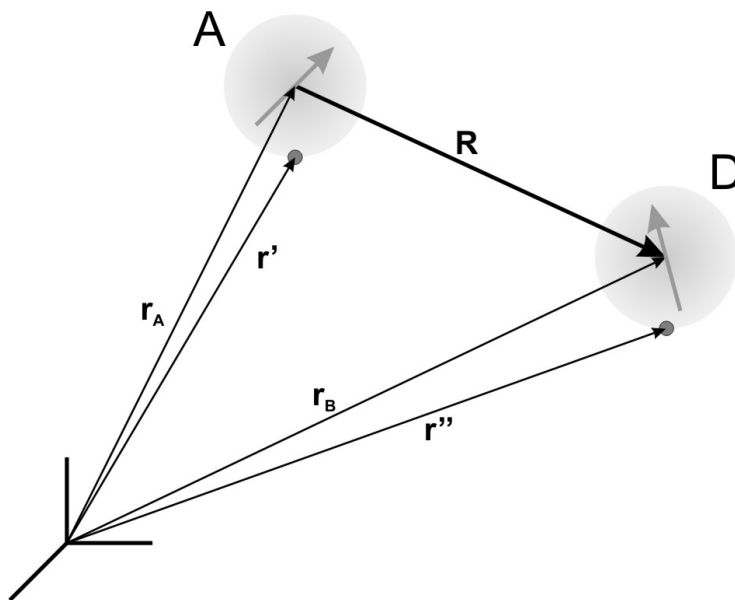


Figure 2.1: Interaction between two particles A (acceptor) and D (donor).

The transition dipole moment  $\boldsymbol{\mu}_A$  is not a permanent dipole but rather a transient dipolar polarisation induced by the electric field of the donor  $\mathbf{E}_D$  according to the polarisability  $\boldsymbol{\alpha}_A$  of the acceptor which, to first order, describes the collective behaviour of all charges of the acceptor. In the linear regime, the power transferred from the donor to the acceptor is approximated as

$$P_{D \rightarrow A} = \frac{\omega_0}{2} \text{Im} \{ \boldsymbol{\alpha}_A \} | \mathbf{n}_A \cdot \mathbf{E}_D(\mathbf{r}_A) |^2, \quad (2.35)$$

using  $\boldsymbol{\mu}_A = \boldsymbol{\alpha}_A \mathbf{E}_D(\mathbf{r}_A)$ . The polarisability can be expressed using known parameters by introducing the absorption cross-section  $\sigma$ . By definition,  $\sigma$  corresponds to the fraction of the power absorbed by the acceptor averaged over all possible absorption dipole orientations  $\langle P \rangle$  and the incident intensity  $I_0$ . Thus, it follows [22]:

$$\sigma(\omega_0) = \frac{\langle P(\omega_0) \rangle}{I(\omega_0)} = \frac{\omega_0}{3} \sqrt{\frac{\mu_0}{\epsilon_0}} \frac{\text{Im} \{ \boldsymbol{\alpha}_A \}}{n(\omega_0)}. \quad (2.36)$$

The remaining term in Equation (2.35) is the electric field of the donor evaluated at the position of the acceptor. This is determined by the free-space Green's function as introduced above

$$\mathbf{E}_D(\mathbf{r}_A) = \omega_0^2 \mu_0 \mathbf{G}(\mathbf{r}_D, \mathbf{r}_A) \boldsymbol{\mu}_D \quad (2.37)$$

and is derived in detail in [22]. Using the normalised donor emission spectrum  $f_D(\omega)$  the rate of energy transfer between donor and acceptor is

$$\frac{\gamma_{D \rightarrow A}}{\gamma_0} = \left[ \frac{R_0}{R} \right]^6, \quad R_0^6 = \frac{9c^4 \kappa^2}{8\pi} \int_0^\infty \frac{f_D(\omega) \sigma_A(\omega)}{n^4(\omega) \omega^4} d\omega. \quad (2.38)$$

The transfer rate from donor to acceptor depends on the spectral overlap determined by the frequency integral over emission spectrum  $f_D$  of the donor (in units of  $\text{cm}^{-1}$ ) and absorption cross-section  $\sigma$  of the acceptor (in units of  $\text{m}^2$ ). The so called orientational factor  $\kappa^2$  is given as

$$\kappa^2 = [ \mathbf{n}_A \cdot \mathbf{n}_D - 3 (\mathbf{n}_R \cdot \mathbf{n}_D) (\mathbf{n}_R \cdot \mathbf{n}_A) ]^2 \quad (2.39)$$

and holds values in the range of  $[0 \dots 4]$ . If the exact orientation between the donor and acceptor dipoles is not known, it is common practise to use the orientational average

$$\langle \kappa \rangle^2 = \frac{2}{3} \quad (2.40)$$

instead.

## 2.3 Principles of Fluorescence

As the size of molecules is usually much smaller compared to the wavelength, laws of quantum mechanics become apparent. Classical absorption and scattering processes considered so far are supplemented or replaced by resonant interactions if the energy of a photon interacting with a molecule gets comparable to the energy separations between discrete internal electronic energy levels. This is often the case at optical frequencies. To a good approximation molecules are described as effective two level systems, i.e. only those two levels whose difference in energy is close to the interacting photon energy need to be considered.

The optical and spectroscopic properties of the pigment or dye molecules studied in this thesis are, to a large extent, determined by their electronic structure. These molecules feature an extended system of conjugated  $\pi$ -electrons and their corresponding molecular orbitals. The lowest energy transition occurs between the highest occupied molecular orbital (HOMO) and lowest unoccupied molecular orbital (LUMO). Besides electronic states the vibrational and rotational degrees of freedom of a molecule give rise to additional states and corresponding transitions allowed by selection rules. They are apparent as a superimposed manifold of vibrational and rotational states. The corresponding energy eigenvalues are derived from the Schrödinger equation  $H\Psi = E\Psi$ . Within the adiabatic limit and Born-Oppenheimer approximation [31] the electronic and vibrational wavefunctions are separable and the overall wavefunction  $\Psi$  can be written as a product of electronic, vibrational and rotational wavefunctions [31].

### 2.3.1 Excitation

At ambient temperatures,  $k_B T$  is much smaller than the separation between vibrational states. Therefore, only few vibrational levels are excited and excitation occurs mainly from the electronic ground state. Excitation proceeds either resonantly into vibrational ground state of the LUMO ( $S_1$ ) or non-resonantly into higher vibrational modes which is followed by rapid internal (vibrational) relaxation ( $10^{-12}$  s or less) due to collisions with solvent molecules. The rule of Kasha [27] states that the decay cascade ends in the vibrational ground state of the LUMO.

The probability of photon absorption is given by the absorption cross-section, as defined in Equation (2.36). An excitation beam of intensity  $I$  penetrating into a dilute sample along the direction  $z$  is partially absorbed by randomly-oriented molecules. After travelling an infinitesimal distance  $dz$  the intensity has dropped to

$$I(z)I(z + dz) = -\frac{N}{V} \langle P(z) \rangle dz, \quad (2.41)$$

where  $N/V$  corresponds to the volume concentration of the absorbers. In the limit  $dz \rightarrow 0$  follows

$$I(z) = I_0 e^{-N/V \sigma z}, \quad (2.42)$$

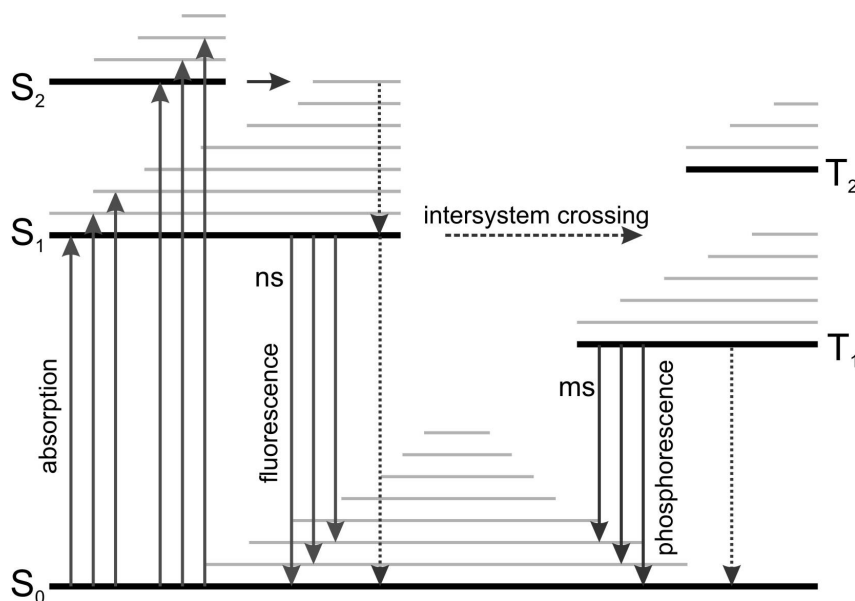


**Figure 2.2:** Energy level diagram of an organic dye molecule. After absorption of a photon the molecule is excited into one of the singly excited state  $S_0$  (HOMO),  $S_1$  (LUMO) or  $S_2$  and their complemented manifold of vibrational states. It relaxes by fast internal relaxation into the vibrational ground state of the first excited electronic state according to Kasha's rule. From here the molecule either decays radiatively by fluorescence or non-radiatively (dissipation to heat, dashed arrows). Intersystem crossing leads to excitation of long-lived triplet states which may decay via phosphorescence. Reproduced from [22].

which is commonly known as the Lambert-Beer law. In practice the absorption is measured in terms of the molar extinction coefficient  $\epsilon(\lambda)$  (in units of  $\text{mol l}^{-1}\text{cm}^{-1}$ )

$$I(z, \lambda) = I_0 10^{-\epsilon(\lambda)[M]z}, \quad (2.43)$$

where  $[M]$  denotes the concentration of absorbers in  $\text{mol l}^{-1}$ .

The strength of  $S_1 \leftarrow S_0$  transition is determined by transition matrix elements. Within the dipole approximation this corresponds to the matrix element of the dipole operator, supplemented by corresponding vibronic states. Absorption and emission dipole moments are determined by the molecular wavefunction and stay constant on the time scale of a transition. In proteins, however, structure is often flexible and change the transition dipole moment. Structural variations of the immediate environment are thus mirrored in the optical properties of a molecule.

### 2.3.2 Fluorescence Emission

The molecule remains in an excited electronic state during the fluorescence lifetime, which frequently ranges from 1-10 ns. From there it returns to the ground state via fluorescence or non-radiative decay channels, e.g. via vibrations and collisions, finally converting excitation

energy into heat. The ratio of radiative decay rate  $\gamma_r$  and total decay rate  $\gamma = \gamma_r + \gamma_{nr}$  is called the quantum yield

$$q = \frac{\gamma_r}{\gamma_r + \gamma_{nr}}, \quad (2.44)$$

which is identical to the intrinsic quantum yield. However, in inhomogeneous environments both  $\gamma_r$  and  $\gamma_{nr}$  are functions of local inhomogeneities. This aspect is discussed in detail in Chapter 7. The interplay of radiative and non-radiative decay rate determines the radiative (fluorescence emission) lifetime which is defined as

$$\tau = (\gamma_r + \gamma_{nr})^{-1}. \quad (2.45)$$

The non-radiative decay can take place through several channels. Already mentioned above is internal conversion with rate  $\gamma_{IC}$ . This channel is due to fast vibrational relaxation caused by collisions with solvent molecules. A similar process, intersystem crossing  $\gamma_{ISC}$ , leads to dissipation of excitation energy to heat. Because of a non-negligible spin-orbit coupling there is also a finite torque acting on the spin of excited electrons. This leads to a small but significant probability of spin flip  $S=1 \leftarrow 0$ . In such a triplet state the spin multiplicity equals  $2S+1=3$  allowing the electrons three possible orientations. Electron energy is reduced. Exchange interaction between parallel spins increases the average distance between the electrons according to Hund's rule [27]. This increased distance between electrons leads to lowering of Coulomb repulsion. Triplet radiative decay into singlet ground state is a highly forbidden transition and features exceptionally long lifetimes of typically  $\sim 1-10$  ms. Yet another non-radiative decay channel opens through electron transfer  $\gamma_e$ . For a detailed discussion see [32–34]. Including possible resonant energy transfer (see Section 2.2) the overall non-radiative decay rate equals

$$\gamma_{nr} = \gamma_{IC} + \gamma_{ISC} + \gamma_e + \gamma_{D \rightarrow A}. \quad (2.46)$$

The fluorescence emission spectrum is composed of sums of Lorentzians that constitute the vibrational progressions corresponding to the different decay pathways to the ground state vibronic levels. At ambient temperatures vibrational progressions are broadened and not resolvable by standard spectroscopic techniques. Instead of strict selection rules it is only possible to derive probabilities for certain decay channels. The so called Frank-Condon factors are determined by overlap integrals of LUMO and HOMO vibrational state wavefunctions. Their relative magnitude determines the shape of the fluorescence spectrum [11, 12]. In dye molecules radiative decay is efficient. As these molecules exhibit low density of vibronic states of the HOMO and LUMO non-radiative decay is less likely to occur.

In contrast to emission spectra, excitation spectra are plots of intensity of fluorescence emission at a fixed wavelength versus the wavelength of excitation. This concept is particularly well suited to study energy transfer processes discussed above. The light harvesting complexes studied in this thesis absorb light by one set of pigments which may subsequently be transferred to another set of pigments. Excitation of one set of pigments and emission of the other requires

energy transfer. In combination with absorption spectra energy transfer efficiencies can be determined [1].

## 2.4 Principles of Single Molecule Microscopy

The general idea of microscopy is to obtain information from small regions in space which may contain only a single molecule. Since its invention microscopy has grown a valuable tool in many fields of science and is at the heart of the recent development of single molecule microscopy and spectroscopy. There are basically two means to detect signals of individual molecules: by spatial or spectral selection. The former is possible because of the high optical resolution of modern microscopes that allows to spatially select just a single molecule in the probe volume of highly diluted samples. The latter employs narrow band lasers that provide coherent illumination in many different spectral regions. Individual molecules feature slightly different optical properties which allows to address them by spectral selection [35]. However, even at low-temperatures the absorption cross-section is at least two orders of magnitude smaller than the area illuminated by a laser. It is a difficult task to separate this weak absorption from the shot noise background of the system [20]. Instead, single molecule microscopy utilises the fluorescence of dye molecules to achieve high contrasts. This is a direct consequence of the Stokes shift, i.e. molecules are detected at wavelengths red-shifted compared to illumination. Highly sensitive detectors such as avalanche photodiodes (APD) and charge coupled devices (CCD) are able to detect the weak signal originating from single molecules against the background.

Spectroscopy of single molecules is characterised by a number of unique effects, among them fluorescence blinking and photo-bleaching. The phenomenon of fluorescence blinking is encountered frequently in single molecule experiments. If fluorescence emission intensity of a single molecule is followed over time it repeatedly is excited into a triplet state. In the observed time trace the frequently high count rates of singlet-singlet transitions are interrupted by dark periods extending up to several milliseconds. As long as this process is reversible the molecule returns to fluoresce. However, another characteristic of SMS is that dark periods are observed over much longer times. The molecule may even not recover. The latter effect is called photo-bleaching and may be due to transient interaction with other chemical species such as oxygen. The exact processes are still a matter of debate [36–38] but one possibility could be the formation of singlet oxygen by triplet-triplet annihilation. Singlet oxygen attacks and interrupts the conjugated or aromatic system of the molecule and irreversibly damages it [39].

SMS relies on infinity corrected objectives of high numerical aperture that are key components of modern high resolution microscopy. They set magnification, field of view and resolution, as well as its quality determines light transmission, contrast and aberrations of the microscope image. However, because of the limited size any given objective cannot collect all light coming from a point source into the focus. The image appears to have a finite size. This is a consequence of spatial filtering of high-frequency components through the optical elements

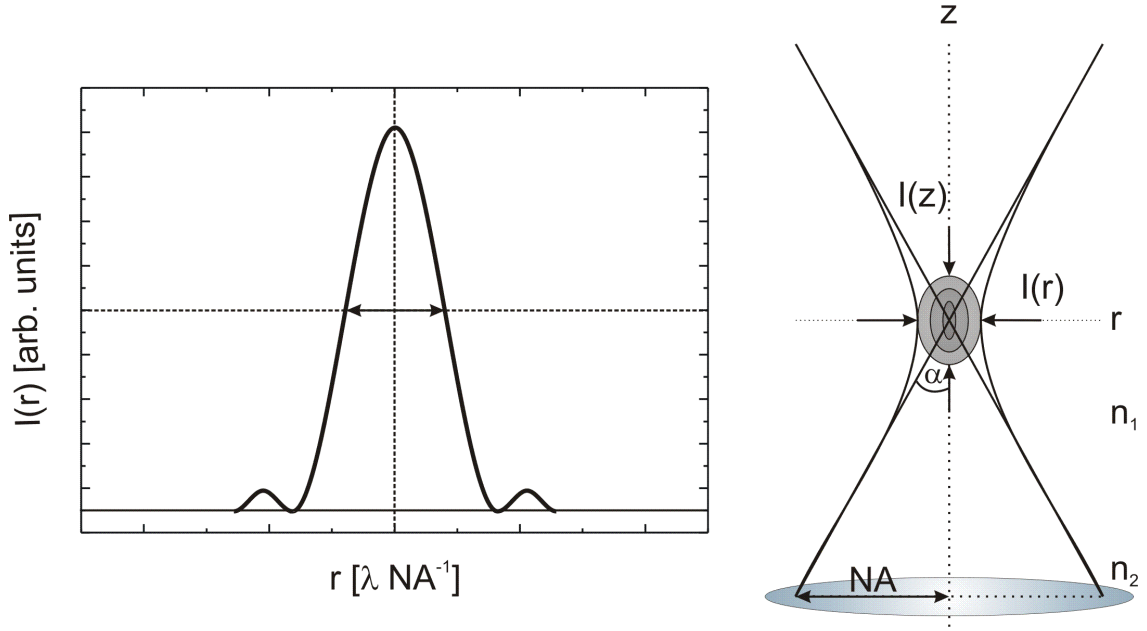


**Figure 2.3:** Left: Point-Spread-Function at the focal plane. Right: Numerical aperture and focusation into PSF.

accompanied with a reduction in bandwidth. The resulting spectrum is not able to accurately reconstruct the original point source. It is fundamentally limited by its finite size characterised by a focusation cone. The effective size of this cone is described in terms of the numerical aperture NA, which is defined as

$$NA = n_1 \sin \theta_{max}, \quad (2.47)$$

where  $\theta_{max}$  denotes the angle of total reflection. As a main consequence, the image does not contain the entire phase information which causes images to look less sharp.

After being focused by the optical system the point-like object is spread into a diffraction pattern of finite width. The intensity map of that pattern is characterised by the point-spread-function (PSF) which defines the spread of a point source (see Figure 2.3). The PSF characterises the spatial resolution: the narrower the PSF the better the resolution of an optical system, and can be calculated using complex mathematical models, including scalar theory, par-axial approximation and angular spectrum framework as described in [22]. The PSF depends on wavelength  $\lambda$ , NA, magnification, as well as illumination and detection geometries. The resulting PSF of an optical system  $I_{\text{PSF}}(x, y, z)$  is given as a convolution of illumination and detection  $I_{\text{ill}}(x, y, z)$  and  $I_{\text{det}}(x, y, z)$ , respectively, and reads

$$I_{\text{PSF}}(x, y, z) = I_{\text{ill}}(x, y, z) \cdot I_{\text{det}}(x, y, z). \quad (2.48)$$

As most microscopy arrangements feature cylindrical symmetry the PSF is commonly denoted as  $I(r, z)$  where  $r$  defines an arbitrary direction parallel to the focal plane  $x, y$  and  $z$  corresponds

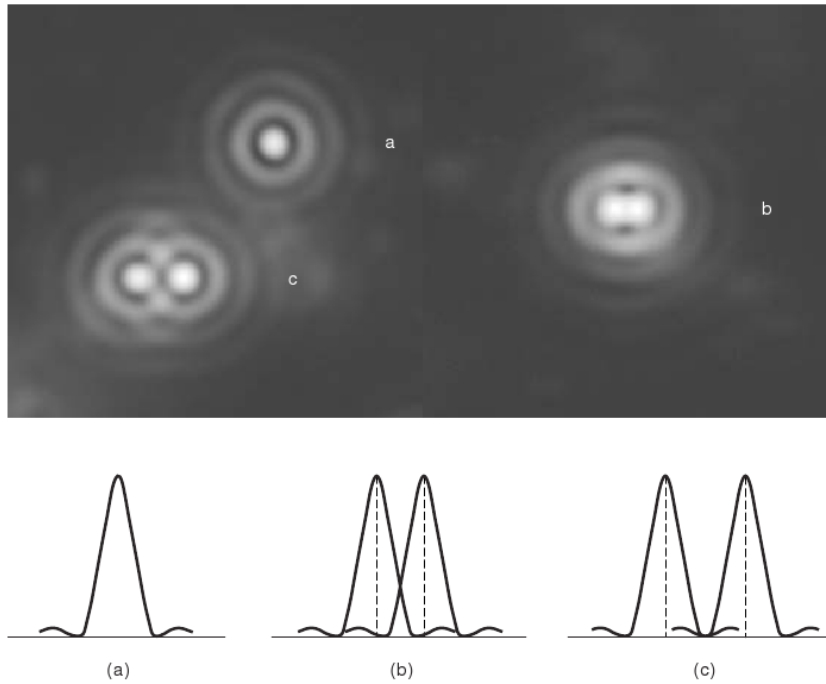


**Figure 2.4:** Criterion for spatial resolution. (a) Profile of a single diffraction pattern (upper panel) and its intensity distributions as a function of separation distance (lower panel). The bright Airy disc and 1st- and 2nd-order diffraction rings are visible. (b) The same two point-like sources separated by exactly one Airy disc, i.e.  $\Delta r$ . The maximum of one disc overlaps with the minimum of the other. The two points are barely resolved showing that the resolution limits derived in the text are merely upper limits. (c) At a separation of two Airy discs, i.e.  $2\Delta r$  the points are clearly resolved. Taken from [40].

to the optical axis.

The PSF is used to define measures of resolution. Figure 2.4 shows several sets of two self-luminous points viewed by a microscope. They appear separate only if their PSFs are far enough apart to be distinct. According to Abbé this is given by the distance between two PSFs for which the maximum of one PSF coincides with the first minimum of the second one. Using par-axial approximation, Abbé [41] estimated this separation to be

$$\Delta r = 0.6098 \frac{\lambda}{\text{NA}}, \quad (2.49)$$

which applies strictly only to two parallel dipoles oriented perpendicular to the optical axis and therefore constitutes an upper limit. This distance  $\Delta r$  corresponds to one Airy disc, which is the radial distance for which the value of the par-axial PSF becomes zero. A similar criterion was found by Rayleigh, who used the overlap of two PSFs in two-dimensional space [42].

The PSFs of excitation and detection paths are characteristic for different types of microscopes. In the next section the experimental features of confocal and wide-field microscopes used

in this thesis are discussed. Other types of microscopes are covered in various sources in literature. Recent developments in high-resolution microscopy are covered in a number of reviews [43–45]. Near-field optical microscopy is discussed in [22]. Extension of wide-field microscopy utilising evanescent fields (TIRFM) is covered in [46, 47]. Applications in single molecule microscopy are reviewed in [20] and [48].

## 2.5 Experimental Techniques

Two different types of microscope configurations are commonly found in SMS and have also been used in this thesis: confocal and wide-field microscopy. Confocal microscopy is able to detect fluorescence from a small diffraction-limited focal volume excited in the sample. Images are obtained either by scanning the sample or the focal volume, i.e. the laser excitation source. This technique provides the spatial resolution to study single molecules and record their spectra. In contrast, wide-field microscopy allows for area detection and imaging of many molecules at the same time. However, spectral information is not accessible this way.

### 2.5.1 Confocal Microscopy

Confocal microscopy relies on a simple principle. The sample is irradiated with focused light originating from a point source or single-mode laser beam and the response from the sample, i.e. the red-shifted fluorescence, is directed onto a pinhole. Light not originating from the focal area cannot pass through the detection pinhole and hence is not detected. Laterally displaced beams are blocked by the detector aperture and beams displaced along the optical axis are not focused on the detection plane and are strongly attenuated. The confocal principle is depicted in the right panel of Figure 2.5. The basic idea was already put forward in a patent application by Minsky in 1955 [49] and has led to the development of many variations of confocal microscopes over the years. A thorough overview about confocal microscopy is given in [50, 51].

The imaging properties of a confocal microscope are determined by the total PSF as already discussed. The PSF represents the volume out of which the probability for exciting and detecting a photon is larger than a chosen threshold value. In confocal microscopy this volume is constructed as a spatial superposition of illumination and detection foci. In a typical confocal arrangement, as depicted in Figure 2.5, excitation and detection are accomplished by the same objective using an inverted path. A beam-splitter, or in fluorescence microscopy a dichroic mirror, is used to split excitation and detection into two separate arms. As a consequence of this geometry the intensity distributions characterising illumination and detection path can be approximated by  $I_{\text{ill}} \approx I_{\text{det}}$ . Thus the intensity distribution of the PSF reads

$$I_{\text{PSF}}(r,z) = I_{\text{ill}}(r,z)^2. \quad (2.50)$$

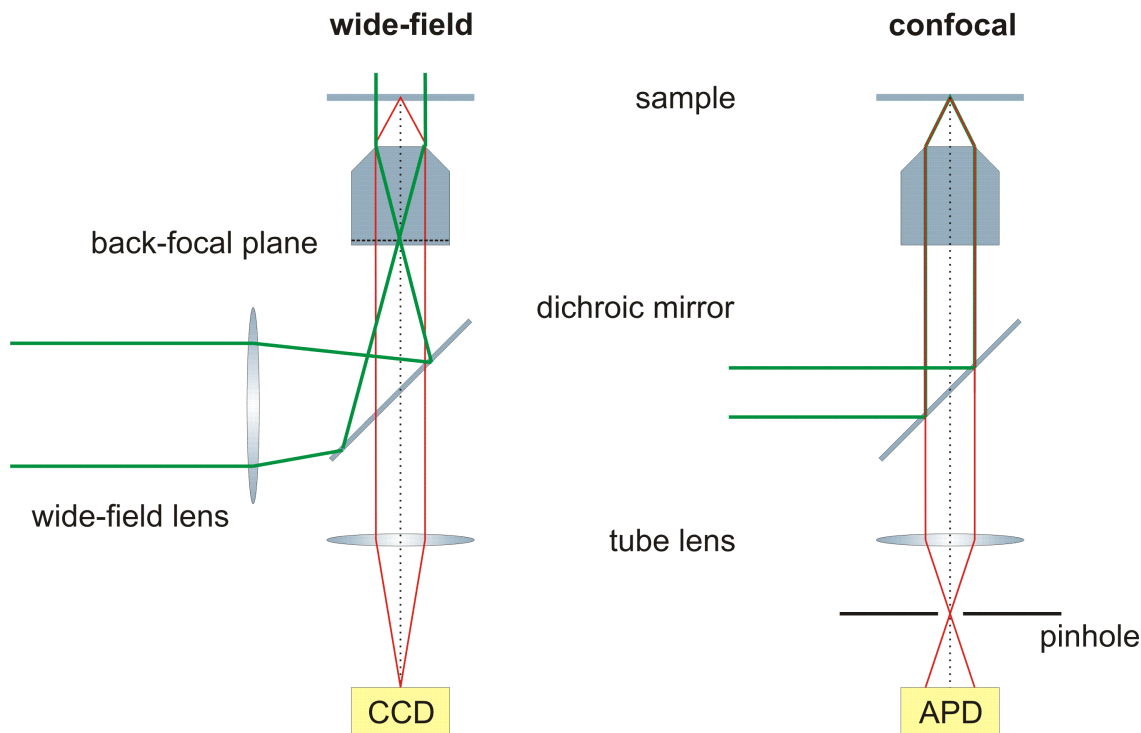


**Figure 2.5:** Single molecule fluorescence microscopy methods. In green: laser excitation; in red: fluorescence from the sample. (a) Wide-field: molecules spread over an area of up to 50 μm x 50 μm are simultaneously excited by a widened laser beam. Fluorescence from this area is imaged onto a CCD area detector. (b) Confocal: The laser excitation beam is focused into the diffraction limited focal volume. The pinhole assures that only light from the focal volume is detected.

This important result states that the PSF of a confocal microscope is essentially the square of the PSF of an ordinary microscope. The confocal PSF displays a three-dimensional ellipsoid that is elongated along the optical axis and whose centre coincides with the geometrical focus of the objective lens. The dimensions of the confocal volume constitute the microscope’s resolution and are typically in the range of 220 x 750 nm for an objective of NA=1.4. In order to determine the exact shape of the PSF mathematically complex methods need to be applied [22, 51, 52]. However, for most purposes it is sufficient to separate the PSF into lateral  $I_{\text{ill}}(r)$  and axial  $I_{\text{ill}}(z)$  components, each approximated by a Gaussian. Their widths depend on wavelength  $\lambda$ , numerical aperture NA and refractive index  $n_1$ . Applying Abbé’s criterion, the resolution limit is found as [51]

$$\Delta r = 0.44 \frac{\lambda}{\text{NA}} \tag{2.51}$$

which is slightly better than estimated in Equation (2.50) for a conventional microscope. This result reflects the sharper peak due to the squared confocal PSF. Applying Abbé’s criterion to

the optical axis yields also an axial resolution which reads

$$\Delta z = 1.5 \frac{\lambda n_1}{\text{NA}^2}. \quad (2.52)$$

Lateral resolution is slightly better than in conventional microscopies like wide-field methods. The confocal diffraction pattern has slightly less energy outside the central peak than is obtainable by a single lens. Therefore, the resolution is less degraded by variations in contrast. The use of a detection pinhole lends confocal microscopes a rather high contrast as off-focus objects are readily discriminated [51]. Thus, unlike most other conventional microscopies the axial resolution is really available.

Experimentally, a confocal microscope is divided into two parts. The excitation path is either fixed and the sample is scanned with respect to it. Or, more commonly the laser excitation source is moved (laser scanning confocal microscope). The laser light source is usually spatially filtered by a pinhole or a single mode fibre in order to arrive at a beam with a perfect Gaussian beam profile. The light is then collimated by a lens whose focal distance is chosen such that after reflection at an appropriate beam splitter or dichroic mirror the beam diameter is large enough to overfill the back aperture of an infinity-corrected microscope objective of high NA which is used to focus the light on the sample. The use of high numerical aperture assures the resulting spot-size is only limited by diffraction at the entrance aperture of the objective.

The second part of a confocal microscope is the detection path. After the laser light interacts with the sample, the fluorescence together with reflected and scattered excitation light is collected by the same microscope objective. This time the high NA assures a wide angle for effective light collection. The infinity corrected objective allows for use of filters and other optical elements without introducing offsets in the light path. The collected light has to be separated from incoming light which is achieved by exploiting the difference in wavelength. The dichroic mirror that reflected the incoming laser light before is chosen such that it blocks the returning excitation light and passes the red shifted fluorescence signal. After some additional filtering the beam is focused by a second lens onto a pinhole in front of a detector which is usually a highly sensitive single-photon counting avalanche photo-diode (APD). The small active areas of such detectors sometimes diminish the need of a pinhole. The size of the pinhole is a means of fine-tuning the performance of a confocal microscope. On one side the pinhole must match the diameter of the focal spot, i.e. the Airy disc produced by the second lens in order to efficiently reject out-of-focus signals. On the other side however, the bigger the size of the pinhole, the more photons can pass which helps to optimise the effective transmission of light. A larger pinhole does not influence the PSF which rather depends on NA as the image of the pinhole in the object plane describes the area of that plane from which photons are collected or which they go to. A good balance between resolution (small pinhole) and transmission (large pinhole) is found for a spot-size two times smaller than pinhole diameter.

### 2.5.2 Wide-field Microscopy

The wide-field microscope is conceptually in contrast to confocal microscopy. The differences are mainly a consequence of illumination geometry which make wide-field methods more similar to conventional microscopy. The laser excitation beam is expanded and focused at the back-focal plane of the objective using a lens (see left panel in Figure 2.5). The objective collimates the beam and uniformly illuminates the sample. The excited fluorescence is collected by the same objective and residual excitation light is filtered away by appropriate filters. This configuration is called epi-fluorescence mode and minimises the amount of background signal. The image is originating from the whole illuminated area simultaneously and recorded by an area detector, in general a CCD camera. In this way, many molecules are studied at the same time.

A result of the uniform illumination of the sample is a PSF that is merely a constant and is approximated as

$$I_{\text{PSF}}(r,z) = I_{\text{det}}(r,z). \quad (2.53)$$

The exact function is calculated in [22, 51, 52]. Similarly to the discussion of confocal microscopy above, the PSF can be separated into lateral and axial components,  $I_{\text{det}}(r)$  and  $I_{\text{det}}(z)$ , respectively and are approximated by Gaussians. Applying the criterion of Abbé the lateral and axial resolution limits read

$$\Delta r = 0.51 \frac{\lambda}{NA} \quad \Delta z = 1.7 \frac{n_1 \lambda}{NA^2}, \quad (2.54)$$

respectively. At  $\lambda = 633$  nm,  $n_1 = 1.51$  (immersion oil) and  $NA = 1.4$  the resulting PSF features 230 nm x 829 nm. However, in contrast to confocal microscopy the axial resolution is usually not available. In the set-up used in this thesis at the same conditions the PSF features only 300 nm x 3  $\mu\text{m}$  [53] which is due to reduced contrast as compared to confocal methods. As the widened beam passes through the entire sample it also excites molecules not situated in the focal plane. This leads to additional background that deteriorates the contrast and thereby the available axial resolution. This problem is addressed by alternative wide-field methods deploying evanescent fields, e.g. TIRF microscopy [46, 47]. However, the reduced axial resolution is not an issue in the context of this thesis as the samples used here are prepared in thin polymer films of about 200 nm thickness.

### 2.5.3 Comparison

Confocal and wide-field microscopy methods both feature a number of advantages and disadvantages which enable them to address different tasks. The most important features are summarised in Table 2.1. Most experiments presented in this thesis have been conducted using a modified Zeiss LSM-410 confocal microscope (see Chapter 4 for experimental details). The main feature of this set-up is the ability to record spectra of single molecules at a time. The wide-field microscope based on a Nikon Eclipse TE 200 was used to record polarisation

resolved data using a Wallaston prism. The CCD detection allowed for simultaneous data collection of many molecules.

	<i>wide-field</i>	<i>confocal</i>
<b>Focal volume</b>		
x-y plane	300 nm	300 nm
optical axis z	1-2 $\mu\text{m}$ (TIRFM: 100-200 nm)	900 nm
<b>Temporal resolution</b>		
in 1-dim.	-	1 $\mu\text{s}$
in 2-dim.	512 x 512 px at 30 fps	200 x 200 px at $\sim$ 1 fps
<b>Advantages</b>		
	imaging with high temporal and spatial resolution	spot scan with high temporal resolution
	array detection	spectral information
	low z-resolution	high z-resolution
<b>Limitations</b>		
	no spectral information	slow acquisition times
	out of focus contributions	limited to one molecule at a time

**Table 2.1:** Comparison of single molecule fluorescence methods. fps: frames per seconds

# CHAPTER 3

---

## Photosynthesis and the Peridinin Chlorophyll Protein

---

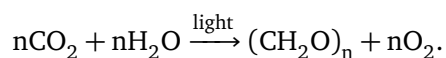
In a general definition 'photosynthesis is a biological process whereby the Sun's energy is captured and stored by a series of events that convert the pure energy of light into the biochemical energy needed to power life' [1]. Section 3.1 shows how green plants as well as certain bacteria and algae developed diverse strategies to exploit the energy of sunlight. These involve the absorption of solar photons and conversion of their energy to synthesise organic compounds like carbohydrates. Photosynthesis involves several building blocks. Section 3.2 introduces light-harvesting complexes that are associated with the very first step in photosynthesis and function to absorb and transfer the energy to reaction centres where conversion of excited state energy into chemical compounds is initiated. Light-harvesting complexes are built of pigments like chlorophylls and carotenoids presented in Section 3.3 that are bound into a protein structure. A light-harvesting complex is at the focus of this work: the peridinin chlorophyll protein or PCP Sections 3.4 and 3.5 summarise structural and spectral features of this complex as well as the current understanding of the energy transfer pathways between its pigments.

### 3.1 Oxygenic Photosynthesis

Most living organisms directly or indirectly make use of energy that is originating in photosynthesis to drive their metabolism. Organisms are commonly divided into autotrophic and heterotrophic groups. The group of heterotrophic organisms gains its energy from decomposition of organic compounds and is unable to use inorganics as sole sources for organic synthesis [1, 54]. Autotrophic organisms are further categorised into the chemoautotrophic group, i.e. organisms that obtain their energy to drive life processes from oxidation of inorganic elements. And organisms making direct use of radiant energy are specified as photoautotrophic.

Photosynthesis is the process by which autotrophic organisms, i.e. green plants, as well as many bacteria and algae, produce organic substances from pure inorganic compounds, and, in rare cases, low-energy organic compounds, using the sun's electromagnetic radiation as a driving

force. In oxygenic photosynthesis carbon dioxide is reduced by water under the illumination with light that ultimately leads to synthesis of carbohydrates  $(\text{CH}_2\text{O})_n$  thereby storing the sun's energy in starch. The overall reaction for this process reads



The water molecule acts as an electron donor and carbon dioxide functions as an acceptor of electrons. In nature other donors and acceptors occur as well, like  $\text{H}_2\text{S}$  and  $\text{NO}_3^-$ ,  $\text{N}_2$ ,  $\text{H}^+$ , respectively. It is widely thought that oxygenic photosynthesis evolved out of its inorganic counterparts in the course of evolution only because of a shortage of other electron donors.

However, the rather simple overall chemical reaction doesn't reflect the complexity and huge variety of protein complexes and small molecules that are involved in photosynthesis. For all autotrophic organisms the photosynthetic process is rather divided into two distinct phases called the light and dark reactions. The light reactions involve the initial absorption of sunlight and lead to synthesis of cell fuel components such as adenosine-tri-phosphate (ATP) or reduced nicotinamide-adenine-dinucleotide-(phosphate) (NAD(P)H). During the dark reactions no further absorption is involved and carbon dioxide is fixed and reduced with use of ATP and NAD(P)H to create carbohydrates. Both ATP and carbohydrates are used in the organisms metabolism to sustain its life processes. The course of these reactions is summarised, in most photosynthetic organisms, in the so called Calvin cycle [55]. In green plants and algae the apparatus involved in the light reaction is contained in specialised organelles, called chloroplasts. The pigment proteins used during the course of reactions are usually embedded into a highly folded inner structure, called thylakoid membrane. The inside of this membrane is denoted the lumen side, the outside the stroma. Figure 3.1 shows a schematic cross-section of a thylakoid membrane.

The first steps of photosynthesis involve the absorption of sunlight by light-harvesting complexes, sometimes also called antennae. These pigment-protein complexes are generally comprised of pigments belonging to three groups, chlorophylls (Chl), phycobilins and carotenoids and are adapted to the environment a given organism lives in. After absorption by one of the pigments, excited state energy is transferred to a neighbouring pigment within the same pigment-protein complex or, after several jumps, to another complex nearby.

After generally dozens of such energy transfer steps across the photosynthetic membrane, energy is finally taken up by the photosystem I (PS I) and II (PS II). PS I creates a reductive potential by production of NADPH, while PS II transfers electrons from water to quinon molecules under the release of oxygen. These central protein complexes include reaction centres (RC I and RC II) where conversion of optical excitation into a usable charge potential with reductive properties is initiated by special pairs, two strongly coupled Chl *a* molecules which trigger charge separation. After light absorption the special pair can act as an electron donor. These primary donors are bound into the lumen side and feature slightly different binding sites in RC I and RC II leading to an absorption maximum around 700 nm in RC I and 680 nm in RC II. Therefore the donors are denoted P700 and P680, respectively. The primary

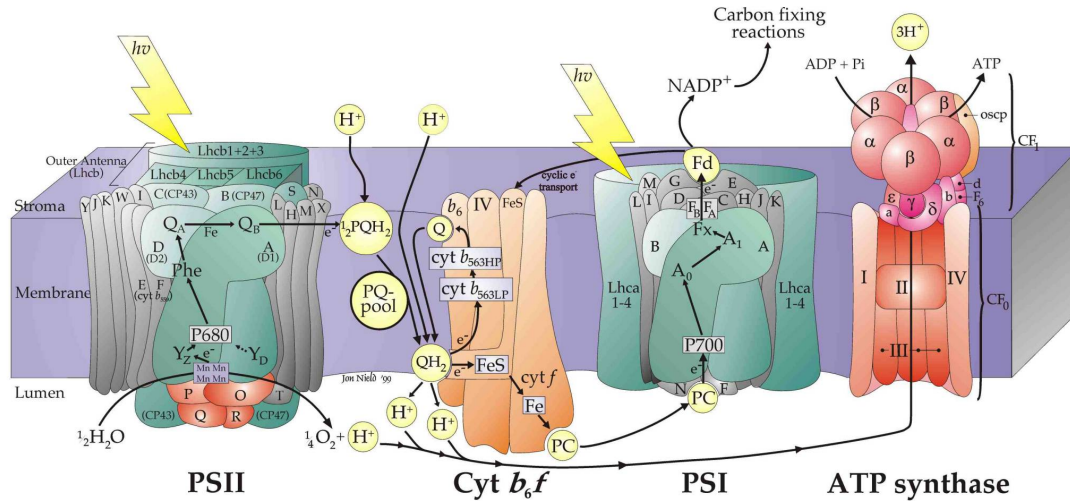


**Figure 3.1:** A schematic cross-section of a photosynthetic thylakoid membrane as found in green plants and many algae. It shows three main complexes, photosystem I and II (PS I and II), as well as cytochrome  $B_6f$ , found to drive electron and proton flow across the membrane. The resulting proton gradient drives the ATPase. Taken from [56]

electron transfer initiated by the RCs is followed by secondary processes leading to energy stabilisation and net proton gradient formation. This gradient, reaching from lumen to stroma, is the driving force for the ATP synthase which attaches a third phosphate group to adenosine-di-phosphate (ADP) to yield ATP. ATP, together with NADPH, are key components used to finally synthesise stable products. Details can be found in [1, 54].

### 3.2 Light-Harvesting Antennae

RCs are remarkably efficient and initiate an electron transfer cascade nearly every time they absorb a photon [1]. However, even under bright sunlight the reactive pair in an isolated RC absorbs a photon only a few times a second. This rate will drop even further in more unfavourable environments. The overall absorption cross-section of the photosystem is improved by light-harvesting complexes surrounding the PS I and PS II. Some of these antennae, like the core antennae, are close to the RC or directly bound to them, and are therefore an inherent part of the photosystems. Examples for the former are the Chl proteins CP43 and CP47, for the latter - core antenna pigments of PS I. In contrast, peripheral light-harvesting complexes are often only loosely bound to the photosystems and can be expressed in huge quantities. Such antennae feature a large variety of different structures and are optimised to the environment the specific organism is embedded in. Nevertheless, in all oxygenic organisms Chl *a* pigments play an important role. Via radiationless energy transfer excitation energy is funnelled down between individual antennae towards the RCs. Charge separation at P680 and P700 takes place within 20-40 ps which prevents that excitation energy

is transferred away from the RCs. Overall, both RCs feature an additional pool of about 500 Chl and other pigments to assure efficient capture of light.

Unlike RCs light-harvesting complexes feature a vast variety of structures enabling them to optimise light capture in many different environments. The structural arrangement of the pigments is crucial for establishing highly efficient energy transfer pathways and is provided by binding to protein capsules, which belong to seven basic families [57]. However, there are a few general themes all light-harvesting complexes share:

- strong absorption in visible and near IR
- long-lived excited states generated by absorption
- closely-packed and stable molecules in order to provide pathways for excitation migration to the RCs
- deactivation mechanisms to remove destructive side-products, e.g. triplet states, singlet oxygen
- photo-protection under strong light conditions, avoidance of concentration quenching

### 3.3 Building Blocks of PCP Antennae

The following discussion is focused on a special light-harvesting complex studied in this thesis: the peridinin chlorophyll protein (PCP). The main pigments in PCP are Chl *a* and the carotenoid peridinin or Per. This section introduces their structural and spectral properties.

#### 3.3.1 Chlorophylls

Chls are the most abundant pigments in photosynthesis and Chl *a* can be found in all oxygenic photosystems. The name chlorophyll was first used by Pelletier and Caventou in 1818 and is derived from greek chlōrós, green and phýllon, leaf to describe the pigment mixture that lends plants their characteristic greenish-blue colour [58, 59]. A variety of about 50 different types of Chl molecules are known and are integral parts of RCs and various antenna complexes [60]. Chls mediate most efficient energy transfer between antennae and RCs.

Despite the large number of different Chls some structural characteristics are shared by all of them. Chls belong to the group of cyclic tetrapyrroles whose structures are based on the macrocyclic porphine system. Figure 3.2 shows the structure of Chl *a* as an example. The central Mg atom is coordinated to four nitrogen atoms each being part of a substructure derived from pyrrole rings denoted from A-D in a clockwise fashion<sup>1</sup>. Added to this modified porphine structure is a fifth ring E at the lower right corner at ring C. At the lower left side a

---

<sup>1</sup> Coordination to a fifth ligand is possible which usually is a polar aminoacid of the apoprotein. [59]

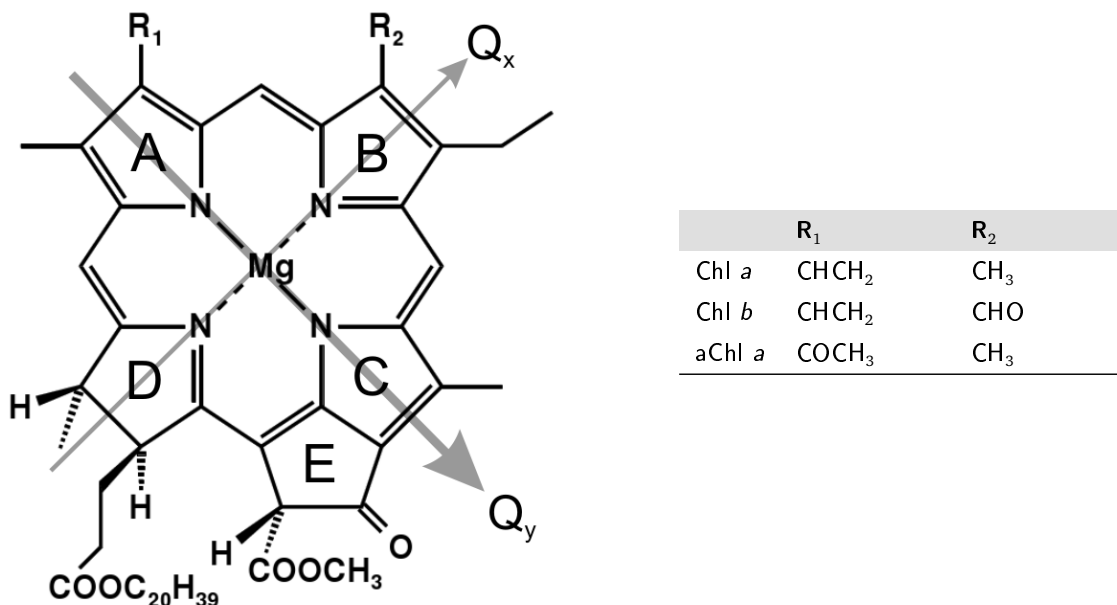


**Figure 3.2:** Chl structure according to IUPAC convention. Grey arrows denote  $Q_x$  and  $Q_y$  dipole moments, respectively. The Chls used in this thesis vary in positions  $R_1$  and  $R_2$ . The corresponding functional groups are listed in the table.

long hydrocarbon chain, generally phytol, is attached that often serves as an anchor to bind into proteins. The system of delocalised  $\pi$  electrons extends over most of the molecule but is distorted at this position. The different Chls vary in the side-groups attached e.g. to  $R_1$  and  $R_2$  (see Figure 3.2) but can also lack the phytol chain. Three Chls are of special interest in this thesis: Chl *a*, [3-acetyl]-Chl *a* (acChl *a*) and Chl *b*. Chl *a* is found in large quantities in photosystems of both eukaryotes and prokaryotes. It features a  $\text{CHCH}_2$  functional group at  $R_1$  and a methyl group  $\text{CH}_3$  at  $R_2$ . The structure of the non-natural acChl *a* shows only minor structural changes ( $\text{COCH}_3$  at  $R_1$ ) but its absorption is moved by  $\sim 20$  nm to the red with respect to Chl *a*. Chl *b* has a formyl group  $\text{CHO}$  at position  $R_2$  and its absorption is shifted by  $\sim 20$  nm to the blue. Chl *b* is the major accessory pigment in green plants and algae, and certain cyanobacteria. Absorption spectra of these three Chls in acetone are depicted in Figure 3.3 and spectral properties are summarised in Table 3.1.

All Chls feature two main absorption bands that span in the blue or near UV and red or

Pigment	$\lambda_{\text{abs}}$ [nm]	$\lambda_{\text{em}}$ [nm]	$\epsilon_{\text{max}}$ [ $\text{mM}^{-1}\text{cm}^{-1}$ ]	$\tau$ [ns]	$q$
Chl <i>a</i>	662, 430	668	78.8	6.1	0.35
Chl <i>b</i>	644, 455	652	46.6	3.6	0.15
acChl <i>a</i>	678, 434	692	65.2	-	-

**Table 3.1:** Spectral properties of different Chls in acetone. Absorption  $\lambda_{\text{abs}}$  from  $Q_y$ - and Soret-band, respectively; emission  $\lambda_{\text{em}}$  from  $Q_y$ . Taken from [62, 63]

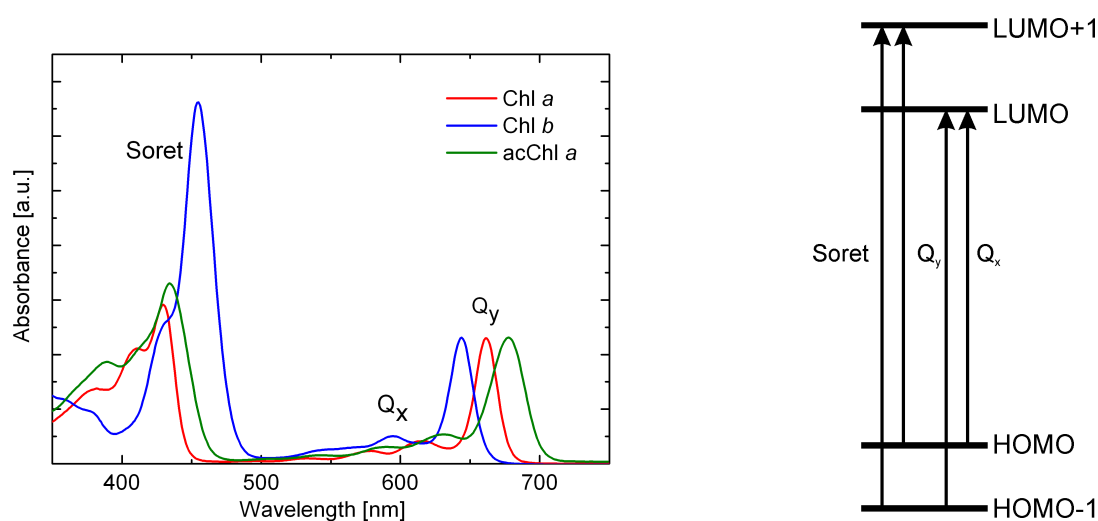
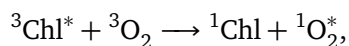


**Figure 3.3:** Left: Absorption spectra of the Chls in acetone used in this thesis. Spectra are normalised to the  $Q_y$  maximum for better representation. Right: Four-orbital model to explain Chl optical properties. The adjunct  $\pm 1$  denotes the molecular orbital next highest/lowest in energy, respectively [61].

near IR, respectively. The lowest energy bands are called the Q bands and the highest B or commonly the Soret bands. The lack of significant absorption in the green lends many Chls their characteristic green colour. Many aspects of Chl optical properties can be explained using the four-orbitals model first proposed by Gouterman *et al.* [64, 65]. Neglecting more complex configuration interactions the model describes electronic transitions between  $\pi$ -orbitals defined by the highest occupied molecular orbital (HOMO) and lowest unoccupied molecular orbital (LUMO) involving electrons from the chlorine macrocycle. As shown in Figure 3.3 several singlet  $\pi \rightarrow \pi^*$  transitions are optically allowed. The corresponding transition dipole moments are of different oscillator strength and orientation. By convention, the molecular  $y$ -axis is defined to run through nitrogen atoms in rings A and C and the  $x$ -axis through Nitrogen atoms in B and D, respectively. The red-most or  $Q_y$  transition corresponds to the transition dipole approximately running along the molecular  $y$ -axis [66]. The orthogonal  $Q_x$  transition dipole along the  $x$ -axis leads to  $Q_x$  transitions. As symmetry is broken at ring E the  $Q_x$  has a higher energy and weaker oscillator strength as compared to  $Q_y$  transition which causes weak absorption and emission through this transition. The strongest transitions in the visible occur at yet higher energies and are denoted as Soret bands. The  $Q_x$  and Soret states feature very short lifetimes and decay within  $\sim 100$  fs via internal conversion to  $Q_y$  which in many Chls lives for several nanoseconds depending on solvent (see Table 3.1). Thus, almost all excitation transfer between Chls would take place via interaction between  $Q_y$  transition dipoles. Apart from pure electronic transitions additional vibrational overtones are visible as well and are most prominent for  $Q_y$  transitions.

So far only singlet excited states in Chls have been discussed. However, Chls can also be

excited into a system of triplet states, the lowest of which energetically lies well below  $Q_y$ . Such a triplet can be excited by intersystem crossing from  $Q_y$ . The lifetime of the triplet state is very long and decays within milliseconds. This has an immediate impact on photon absorption which is reduced due to loss of ground state population. Related to the functionality of light-harvesting complexes a more severe problem arises. Chl in its triplet state reacts with oxygen molecules via



which results in generation of excited singlet state oxygen. In turn, singlet oxygen can convert into an oxygen radical which is highly reactive and toxic. As a consequence the photosynthetic apparatus is damaged. Light-harvesting complexes as will be discussed in Section 3.3.2 feature strategies of photo-protection which are mainly based on carotenoids.

### 3.3.2 Peridinin - the Major Pigment in PCP

Among all photosynthetic pigments carotenoids constitute the most diverse group, both structurally and functionally. Although carotenoids are found in various light-harvesting antennae they only rarely take over a central role in light-collection in terrestrial plants. They are however indispensable to photosynthesis because of their photo-protection abilities. Remarkably, several algae use carotenoids as key pigments, among them the dinoflagellates that use PCP. About 1/3 of all globally available carotenoids are peridins, and 50 % fucoxanthins, both pigments feature excellent light-harvesting capabilities [67]. Furthermore, carotenoids fill the green gap between  $\lambda_{max} = 450\text{-}500\text{ nm}$ , not covered by other pigments. This property renders them attractive to aid light-harvesting in PCP complexes found in marine photosynthetic algae like dinoflagellates.

Carotenoids are almost one-dimensional molecules that consist of a polyene chain of conjugated double bonds with small end groups at both sides. Many of more than 800 known carotenoids [60] feature only a branched carbon  $C_{40}$  chain, like for example lycopene. In oxygenic organisms the ends of such a chain are functionalised by cyclic groups as in the renowned  $\beta,\beta$ -carotene, which lends its name to the whole group of carotenes. Derivatives to carotenes constitute the group of xanthophylls, and among its most wide-spread members is Per. Per lacks 3 carbon atoms, is highly substituted and asymmetric due to a carbonyl group attached to one of its ends, as can be seen from Figure 3.4. The structure of Per was first elucidated by NMR spectroscopy [68] and later confirmed by complete biochemical synthesis [69].

The spectral properties of carotenoids are determined by the symmetry of the carbon chain which belongs to the  $C_{2h}$  point group. The rod-shaped carotenoids show for example typical absorption spectra similar to linear polyenes which feature the same symmetry (see Figure 3.5). However, in carotenoids symmetry is always broken by head- and eventually side-groups, as well as twisting if the molecule is embedded into a protein. To a first approximation, symmetry can be idealised as  $C_{2h}$  but structural deviations determine the unique spectral

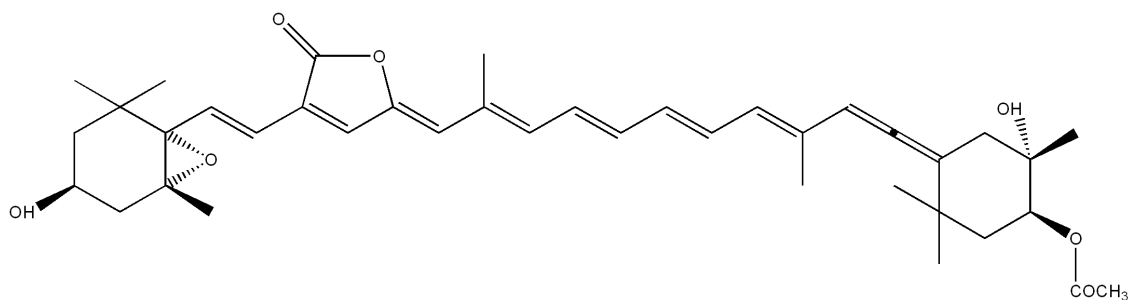


**Figure 3.4:** Chemical structure of Per. Per is a highly asymmetric  $C_{37}$ -carotenoid composed of a polyene chain with a lactone ring. The ends are substituted with an epoxy-cyclo-hexane and cyclo-hexane rings.

properties observed in many carotenoids. For example Per markedly owes its special properties to symmetry breaking caused by its carbonyl endgroup. Figure 3.5 shows a general level scheme of the lowest electronic states and the allowed optical transitions. Ground and first excited state  $S_0$  and  $S_1$  share the same symmetry  $1A_g^-$  and  $2A_g^-$ , respectively. Consequently, an optical  $S_0 \rightarrow S_1$  transition would be strongly forbidden [70]. However, this argument holds strictly only for  $C_{2h}$  symmetry as realised to a high degree for example in  $\beta, \beta$ -carotene. In most asymmetric carotenoids it is partially released. The exceedingly weak transition dipole moment has made it difficult in the past to determine the  $S_0 \rightarrow S_1$  transition energy. Fluorescence and two-photon absorption studies have shown however that  $S_1$  lies slightly above  $Q_y$  of Chls around 600-630 nm. Carotenoids like Per with a carbonyl group in their conjugated chain feature unusually strong  $S_1$  emission [71] with lifetimes up to 150 ps which is probably due to larger deviations from  $C_{2h}$  symmetry. On the other hand,  $S_1$  absorption is negligible. Fluorescence spectroscopy yields a quantum yield of  $\sim 10^{-3}$  in nonpolar solvents and  $\sim 10^{-5}$  in polar solvents [72]. The second electronic excited state  $S_2$  is of  $1B_u^+$  symmetry and  $S_0 \rightarrow S_2$  transition is strongly allowed as it involves two states of different symmetry, i.e.  $1A_g^-$  to  $1B_u^+$ . Strong absorption of carotenoids in the spectral region between 400 and 550 nm is related to this transition but is generally split into a series of three closely spaced vibronic bands that eventually show broadening in different solvents.

The exact nature of the  $S_1$  state in Per has raised some controversy in recent literature. Time-resolved studies revealed that the change in quantum yield between non-polar and polar solvents alters  $S_1$  lifetime from  $\sim 160$  ps to  $\sim 10$  ps, respectively [72–75]. A striking difference between both steady-state and transient absorption spectra in polar and non-polar solvents observed for Per and other carbonyl carotenoids has been reported in [73, 75]. These results were extended by many additional spectroscopic investigations [76–83] and it is now established that the changes in spectral properties as a function of solvent polarity are due to the presence of an additional excited state having charge-transfer character, the  $S_{ICT}$  state [72–74]. In Per this state is stabilised in polar solvents and the stability gets further enhanced in protic solvents through hydrogen bonding via the Per carbonyl group. The exact nature, namely its possible coupling to  $S_1$ , remains a matter of debate [84].

Per excited states and especially polarity-dependence of  $S_{1/ICT}$  are of key importance to

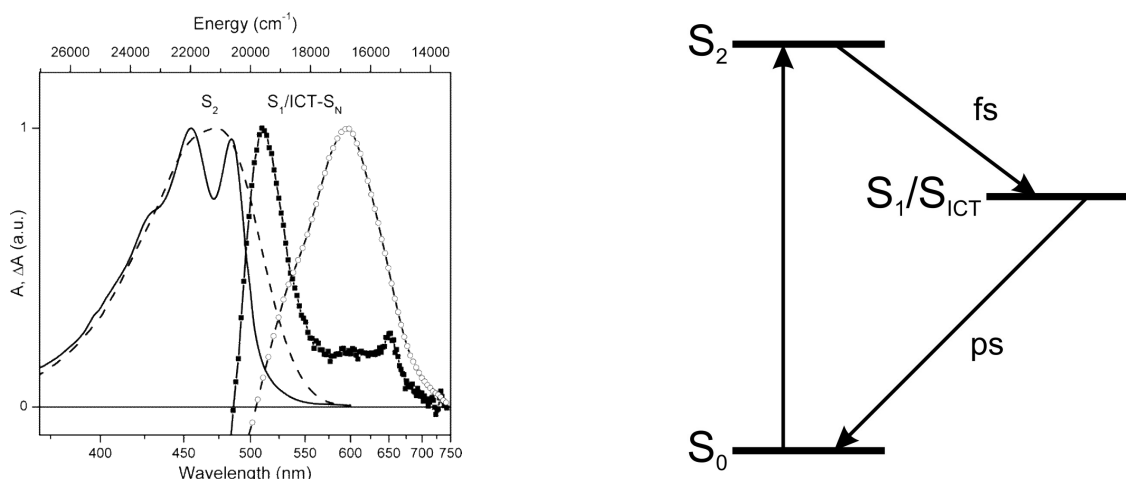
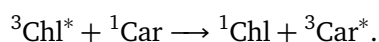


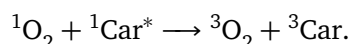
**Figure 3.5:** Left: Room temperature absorption spectra of Per in n-hexane (solid line) and methanol (dashed line). Transient absorption spectra corresponding to the  $S_{1/ICT} \rightarrow S_N$  transition of Per in n-hexane (filled squares) and methanol (open circles) recorded 1 ps after the excitation at 490 nm are also shown. All spectra are normalised to their absorption maximum. Taken from [70]. Right: Energy levels of Per.

energy transfer to other pigments and thereby light-harvesting function of complexes like PCP. As will be discussed in 3.4 the binding sites for Per in PCP provide a moderately polar environment and are postulated to allow for high energy transfer efficiency between Pers and Chls [75, 77, 79, 85–87]. As a consequence of polarity, Per  $S_1$  lifetime in PCP is still rather short and, as most other carotenoids, features extremely rapid internal conversion in the range of a few ps. Similarly, excited state lifetime of  $S_2$  is very short as well and frequently non-radiative relaxation to  $S_1$  is in the fs regime. Excitation transfer runs through the  $S_1$  and  $S_2$  channels (Figure 3.5) and competes with the rapid internal conversion from these states. In order to be efficient it has to take place on an even faster time scale and demands close proximity to energy acceptors, e.g. Chls. As discussed in 3.4 this condition is nicely met in PCP light-harvesting complexes.

Carotenoids play an important role in the photo-protection strategies of light-harvesting complexes [88, 89]. Apart from simply filtering incident light, protection against singlet oxygen is among the most important properties carotenoids lend to light-harvesting antennae [60]. As discussed above, excited Chl features a small probability of inter-system crossing to triplet states in which it can react with oxygen to create singlet oxygen radicals. Carotenoids can efficiently quench Chl triplets as their own triplet states are lower in energy than those of oxygen [90, 91]:



Furthermore, carotenoids are effective quenchers of reactive oxygen and other reactive compounds like  $\text{OH}^-$  [60]:



It is interesting to note that these mechanisms work best at near contact distances as they involve electron transfer. These are e.g. provided in the PCP structure.

### 3.4 Peridinin Chlorophyll Protein (PCP)

The water-soluble PCP is the main light-harvesting complex of the dinoflagellate *Amphidinium (A.) carterae*. Dinoflagellates are unicellular algae that live in the ocean as part of the plankton population (for further details on dinoflagellates see [92]). The core-photosynthetic apparatus of these organisms is similar to that of higher plants as discussed in Section 3.1. They contain the same two photosystems PS I and PS II, together with their related LHC (Lhcd) antennae. However, dinoflagellates express large amounts of water-soluble PCP complexes that are not membrane bound. It is widely thought that PCP transfers its absorption energy to LHC and other PS II related antennae from where it proceeds to RC II. Whether PCP is temporarily bound to the PS II supercomplex is still a matter of debate [93].

#### 3.4.1 PCP Structure

PCP represents a unique example in the large family of light-harvesting antennae. While most of the antennas collect light energy predominantly by (bacterio)Chl or bilin molecules, the main pigment of PCP is the carotenoid Per (see Section 3.3). The characteristic reddish colour related to Per absorption dominates the whole organism and enables dinoflagellates to live at depths in the ocean where only blue/green light is present. The native PCP complex from *A. carterae* forms a homotrimer. Its structure has been determined with 2 Å resolution by Hofmann *et al.* [7] and is depicted in the left panel of Figure 3.6. The trimer is constituted of three boat-shaped  $\alpha$ -helical protomers. These subunits each have a mass of 32 kDa and are denoted as large PCP (l-PCP). They contain two clusters of pigments in an approximate  $C_2$ -symmetry. Each half consists of one Chl *a* nested between two pairs of Pers as depicted in the right panel of Figure 3.6. The pigments in each cluster are in Van der Waals contact. There is also contact between Pers from the two clusters. The centre-to-centre distance of the two Chls is 17.4 Å.

#### 3.4.2 Reconstitution of PCP

PCP can be reconstituted from heterologously-expressed apoprotein of the 16 kDa N-terminal domain of PCP from *A. carterae* mixed with native Chl *a* and Per pigments [94]. Topologically this N-PCP represents a ‘halfmer’ of monomeric l-PCP. Two such halves dimerise and form monomers that after purification share absorbance, fluorescence and circular dichroism (CD) spectra identical to l-PCP. In the context of this thesis the terms ‘monomer’ and ‘halfmer’ are used in a topological sense. The 32 kDa l-PCP from *A. carterae* from which the X-ray structure has been solved, originates from a gene duplication and binds two Per–Chl *a* clusters. For historical reasons, this species is generally referred to as the PCP monomer. With respect to

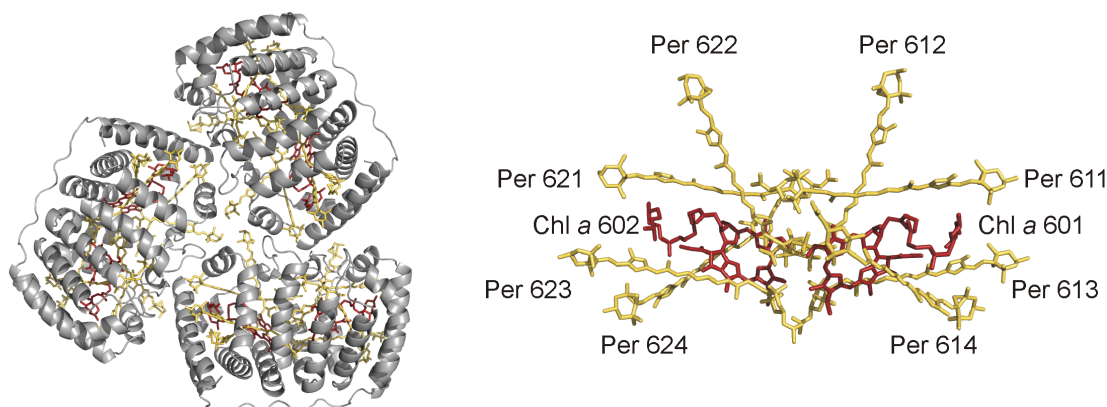


**Figure 3.6:** Left: Structure of the native, trimeric PCP complex. The protein is shown as a grey ribbon. The pigments are represented as red (Chl *a*) and yellow (Per) sticks. Right: Each monomer (protein not shown) contains two Chl *a* molecules and eight Per molecules grouped into two nearly symmetric units. Labelling of individual pigments as used in the literature.

this l-PCP monomer, N-PCP generated from the *A. carterae* protein, is topologically a ‘halfmer’ as it carries only a single Per–Chl *a* cluster, and dimerises to species homologous to the l-PCP monomer. The experimental aspects of the reconstitution procedure are discussed in Chapter 4. Reconstitution can produce both homo- and hetero-chlorophyllous N-PCP complexes, depending on whether initially single Chls or mixtures of Chls are used (see Figure 3.7 and [95]). However, relative binding affinities vary among the Chls, e.g. Chl *b* and acChl *a* feature higher affinities than the native pigment Chl *a* [96]. The ability to systematically alter each Chl site within a N-PCP monomer renders these systems ideal to study both Per–Chl and Chl–Chl energy transfer processes as discussed in 3.5.

### 3.4.3 Steady-State Spectroscopy

Long before the crystal structure was solved, the pairing of Per and Chl into clusters and close spacing of the pigments had been inferred from CD spectra of PCP [97]. Absorption spectra of purified PCP at room temperature show contributions of both pigment types embedded in the protein capsule (see Figure 3.8). The Soret band of Chl *a* is a narrow band at 435 nm,  $Q_y$ -band peaks at 670 nm. The weak-intensity bands between 600 and 650 nm have been resolved in low-temperature absorption spectra [98–100]. Kleima *et al.* combined simulation of absorption spectra with CD and LD (linear dichroism) spectra to assign the band at 625 nm to  $Q_x$  and the ones at 604 and 615 nm to vibronic bands of  $Q_y$ . The simulation and LD spectra indicate that the two Chl *a* are not identical in the two halfmers of the PCP monomer but rather their  $Q_y$  maxima are separated by  $\sim 1$  nm at 77 K. Furthermore, a shift between CD and absorption spectra has been attributed to Chl *a* heterogeneity [99]. The difference between CD and absorption band shapes is consistent with very weak coupling between Chls within a PCP monomer which is estimated to be  $<10$   $\text{cm}^{-1}$  [100].

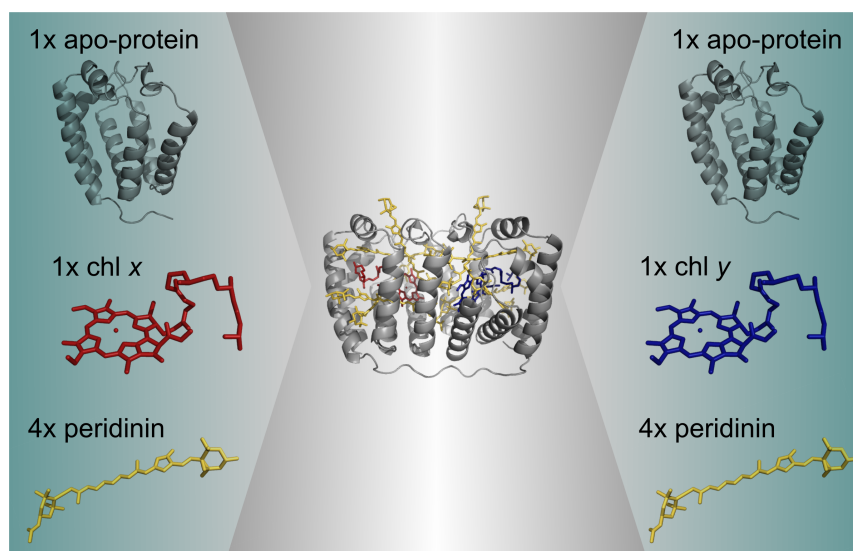


**Figure 3.7:** Schematic of reconstitution process. Heterologously expressed apoproteins of the N-terminal domain of PCP can be mixed with various Chls and Per pigments. According to their binding affinities the pigments are refolded into the apoproteins to form halfmers. During the course of the reconstitution process two halfmers dimerise and form monomeric N-PCP. In a statistical manner such monomers can contain two alike Chls or two different Chls depending on the initial mixture of pigments.

	Per 611	Per 612	Per 613	Per 614	Chl B <sub>x</sub>	Chl B <sub>y</sub>
$\nu$ [cm <sup>-1</sup> ]	18400	20600	19300	18700	23100	23100
$\lambda$ [nm]	543	485	518	535	433	433

**Table 3.2:** Spectral origins of Per S<sub>2</sub> transition as estimated in [101].

Both CD and absorption spectra are dominated by Per S<sub>0</sub> → S<sub>2</sub> transition, responsible for broad absorption between 400 and 500 nm. The lack of any vibrational structure of Per at room temperature points towards polar binding sites [72, 73]. However, a shoulder at 530 nm is apparent in low temperature spectra measured at 77 K [100, 101], 10K [80, 102, 103] and 4 K [100]. These results provide evidence for spectrally distinct Pers as a consequence of slightly different protein environments. Calculations based on the crystal structure suggest moderate (~100-300 cm<sup>-1</sup>) pairwise interaction between the Pers within a single cluster. In order to reproduce the CD spectra all possible interactions between the eight peridinin and two Chls in a double cluster need to be taken into account [101]. Simulations reveal that the inter-cluster interaction energies between most of the Pers in one cluster and the Pers in the second one are significant and need to be considered in order to obtain satisfactory agreement in the Soret band region. The best fit has been obtained with 0-0 S<sub>2</sub> transitions at 543, 518 and 534 nm (Table 3.2). The two Pers 612 and 622 feature blue-shifted spectra and exhibit differences in the two domains of PCP monomer peaking at 485 and 465 nm,

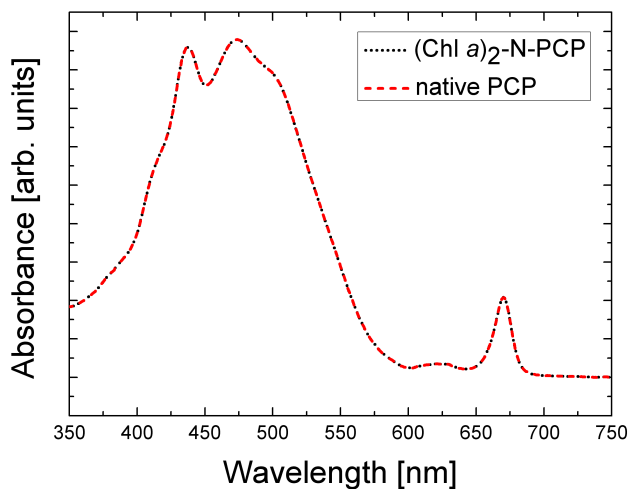


**Figure 3.8:** Absorption of native and N-PCP reconstituted with Chl *a*. The two spectra show nearly perfect overlap.

respectively. It was speculated that the two Pers are not involved in energy transfer to Chls from  $S_1$  and instead redistribute excitation to neighbouring Pers via excitonic coupling (see Section 3.5 and [104]). Quantum chemical calculations suggested that the blue-shifted Pers have reversed ordering of the  $S_1$  and  $S_2$  states [102, 103] and excitation cannot relax into  $S_1$ .

Per in PCP also features a charge transfer state. Zimmermann *et al.* [83] concluded from two-photon excitation spectra that in PCP  $S_{1/ICT}$  of Per is located at 550-560 nm ( $17850$ - $18120$   $\text{cm}^{-1}$ ) but features only weak absorption. These results are consistent with transient absorption measurements [86]. Conventional one-photon spectroscopy found even lower  $S_{1/ICT}$  energy and concluded that the spectral origin of 0-0  $S_{1/ICT}$  transition of Per is isoenergetic with the  $Q_y$ -band of Chl *a* ( $\sim 14900$   $\text{cm}^{-1}$ ). For a detailed review on non-linear steady-state spectroscopy see [84].

### 3.5 Energy Transfer Pathways in PCP

PCP features different energy transfer channels both between Per and Chl as well as among the Chls. Understanding the transfer from Per to Chl has been aided using N-PCP that have been reconstituted with different Chls [94]. The results support theoretical predictions [104] of a major contribution of the relatively long-lived  $S_1$ -state of Per as donor to the Chls [72, 73, 105]. The relatively weak Chl-Chl interactions allow to study energy transfer between two Chls in a structurally well-known situation. In this context, it has been highly advantageous

to study hetero-chlorophyllous N-PCP containing two different, spectrally separated Chls [94].

### 3.5.1 Peridinin to Chlorophyll Energy Transfer

Fluorescence excitation spectra demonstrated Per-Chl energy transfer long before the high-resolution crystal structure allowed detailed insight into the pigment arrangement of PCP [97]. The publication of the structure triggered a number of systematic time-resolved studies that tried to achieve a deeper insight into the energy transfer pathways within PCP. Femtosecond up-conversion methods estimated transfer efficiency to be as high as >85 % [105]. Transient absorption studies of sufficient time-resolution [106] indicated a 3 ps time constant for the rise of bleaching of Chl *a*  $Q_y$ -band. These first studies suggested that energy transfer via  $S_1$  constitutes the primary route with an overall efficiency of 90 % [105, 106]. The charge transfer state of Per was not considered at that time.

The question of whether other energy transfer pathways, involving for example the Per related intramolecular charge transfer state  $S_{ICT}$ , raised some controversy in recent literature. A global and target analysis of transient absorption spectra recorded at various wavelength between 450 and 700 nm suggested a more complete picture [107]. The primary contribution from  $S_1$  was confirmed and the  $S_1$  lifetime estimated to be ~2 ps. However, assuming the 90 % overall energy transfer efficiency from [106] the data could only be fitted by allowing  $S_2$  mediated energy transfer as well. The contribution of this channel was estimated to be as high as 25-50 %. Minor contributions were assigned to originate from  $S_{ICT}$  (~3 %) and from a sub-population of 'disconnected' Pers (10-18 %). Similar conclusions were drawn by Zigmantas *et al.* [86] and later supported by fluorescence up-conversion experiments [85]. The  $S_2$  lifetime was estimated to be 66 fs in PCP which anticipates energy transfer efficiency via  $S_2$  channel to be close to 50 %.

In contrast, theoretical calculations by Damjanović *et al.* [104] predict negligible contribution of Per-Chl transfer via  $S_2$ . Based on a semi-empirical approach they found transfer time via  $S_2$  to be too slow to compete with fast internal conversion to the Per  $S_1$  state. Additionally, they calculated full Coulomb couplings between Pers and Chls together with the corresponding spectral overlaps. The results showed couplings between the Per  $S_2$  states to range from 130 - 520  $\text{cm}^{-1}$  suggesting the possibility of excitons. Surprisingly however, calculated transfer rates were considerably larger than those derived from experiments.

Peridinin 612 and 622 (see right panel in Figure 3.6) have unique properties as compared to the other Pers. They are too unfavourably oriented with respect to Chl *a*  $Q_y$  transition dipole moment to play any significant role in Per-Chl energy transfer. Calculated exciton densities suggest that Per 612 and 622 transfer energy very rapidly to other Per  $S_2$  states [104] predominantly via Per612 and Per621, respectively. Energy transfer between the Per  $S_2$  states is excluded [107] but it was also suggested that Per612 and Per621 feature reversed  $S_1$  and  $S_2$  states [80].

Reconstituted with	$\tau_{S_1/ICT}$ [ps]	$\tau_{ET,S_1/ICT}$ [ps]	$\Phi_{ET,S_1/ICT}$	$\Phi_{S_2}$
Chl <i>a</i>	2.9	3.6	0.82	0.35
Chl <i>b</i>	5.9	9.4	0.63	0.45
acChl <i>a</i>	2.2	2.6	0.86	0.35
native PCP	2.7	3.2	0.84	0.25-0.50

**Figure 3.9:** Parameters of the  $S_{1/ICT}$  and  $S_2$  energy transfer in reconstituted PCP complexes. Calculated  $S_{1/ICT}$ -mediated energy transfer from experimental lifetimes. Efficiencies  $\Phi_i$  calculated in [87].

The influence of the combined  $S_{1/ICT}$  state on energy transfer is still a matter of debate. For a recent review see [84]. The inherent difficulty lies in the fact that  $S_{1/ICT}$  lifetime depends on the solvent, as discussed in Section 3.3.2. Additionally, its intrinsic lifetime in PCP is not known because of immediate energy transfer and could only be estimated to be about 16 ps [86, 107]. The Per binding sites in the PCP protein seem to provide a polar environment. However,  $S_{1/ICT}$  lifetime could also be altered by possible hydrogen bonding via carbonyl group [78] or amino acid residues and water molecules as indicated in the PCP structure [7, 108]. Whether energy transfer from  $S_1$  also involves the contribution from the charge transfer state is suggested in [86] and [80] but still controversial. The gain of charge transfer character could increase the transition dipole moment associated with the  $S_{1/ICT}$  state. This would have an immediate impact on the Förster-type transfer rates that are sensitive to the transition dipole via donor and acceptor coupling. However, its function may just as well be regulatory, converting excess energy to heat [72].

Reconstitution of PCP with various Chl mixtures provides a valuable set of model systems to study Per-Chl energy transfer. The application of different Chls allows for tuning of spectral overlap between Per emission and Chl absorption. Transient absorption experiments demonstrated that reconstituted N-PCP complexes maintain energy transfer pathways of the native form but efficiency of transfer depends on the particular Chl embedded in the complex [87]. Based on the experimentally determined Per lifetimes in N-PCP, Table 3.9 summarises calculated transfer times and efficiencies of Per-Chl transfer. Efficiencies of  $S_{1/ICT}$ -mediated energy transfer are comparable to native PCP for all complexes except reconstitution with Chl *b*. No trend is obvious for  $S_2$ -mediated energy transfer and ranges between 28-45 %. These findings are in agreement with fluorescence excitation spectra. Interestingly, differences in transfer rates could be explained in terms of Förster type energy transfer as a result of changed spectral overlap. Thus, Per-Chl energy transfer seems to proceed via the Förster mechanism and features no excitonic character as in many other light-harvesting systems.

### 3.5.2 Chlorophyll to Chlorophyll Energy Transfer

After excitation is funnelled down to the Chls, energy transfer occurs also between these pigments. First fluorescence anisotropy studies on Chl-Chl energy transfer were aided by

the high-resolution crystal structure [66]. Rapid fluorescence depolarisation of 6.8 ps decay has been assigned to intra-monomer energy transfer between the Chls, a much slower component of 350 ps lifetime to Förster type inter-monomer transfer between Chls. These results were used to model energy transfer rates between the Chls that were assumed to be isoenergetic. For Chls in one monomer time constant is 14.6 ps, for Chls in neighbouring monomers constants range from 0.66-12.1 ns. These high values result from both high inter-Chl distances as well as unfavourable orientation of dipole moments already apparent from the crystal structure. Similar results have been obtained by low-temperature spectroscopy [102].

N-PCP reconstituted with mixtures of different Chls constitute an ideal system to test predictions based on Förster theory. Different  $Q_y$ -band energies alter spectral overlap and thereby energy transfer rates. Recently, Miller *et al.* studied two such systems: (Chl *b/d*)-N-PCP and (Chl *a*/BChl *a*)-N-PCP [94]. Time-resolved spectroscopy allows for direct monitoring of energy transfer in these complexes by excitation of higher energetic component. The rise of bleaching of  $Q_y$  of lower energetic component shows decay that matches the originally excited Chl. Such observations are in close agreement to Förster theory [109].

The relatively slow inter-monomer transfer rates have important implications for the operation of PCP *in vivo*. Similar to bacterial LHC [110] it was speculated by Hofmann *et al.* that energy would equilibrate in the PCP homotrimer. Onward energy transfer towards to RCs is expected to occur on a much faster time scale so that it is unlikely the system is able to return to equilibrium. To assure efficient energy transfer each monomeric unit should be placed in close vicinity to an acceptor protein, like LHC. This could be realised if the *in vivo* form would indeed be the trimer [66].

### 3.6 Conclusion

The peridinin chlorophyll protein (PCP) is a unique light-harvesting complex comprised of tightly clustered Chl *a* and Per pigments with an exceptionally high carotenoid-Chl ratio of 4:1. The highly modified Per features an unusually long-lived  $S_1$ -state. These properties render PCP a challenge to understand pigment interactions and excitation energy transfer between Per and Chl as well as among the Chls. In recent years these issues have been addressed by many experimental and theoretical studies. Figure 3.10 summarises the current understanding of energy transfer pathways in PCP that have been gained from these observations. Excitation transfer from Per to Chl proceeds predominantly via the relatively long-lived  $S_1$  state as donor and reaches high efficiency of ~90-100 %. Research on PCP has been aided using N-PCPs that have been reconstituted with different Chls. Per-Chl and Chl-Chl energy transfer could be studied in a structurally well-known situation that is relatively simple as compared to other photosynthetic systems. In this context, it has been highly advantageous to study PCP containing two different, spectrally separated Chls.

Experimental studies, though extensive, have only been carried out at the ensemble level. In this thesis, the first investigations on PCP using single molecule spectroscopy are presented.

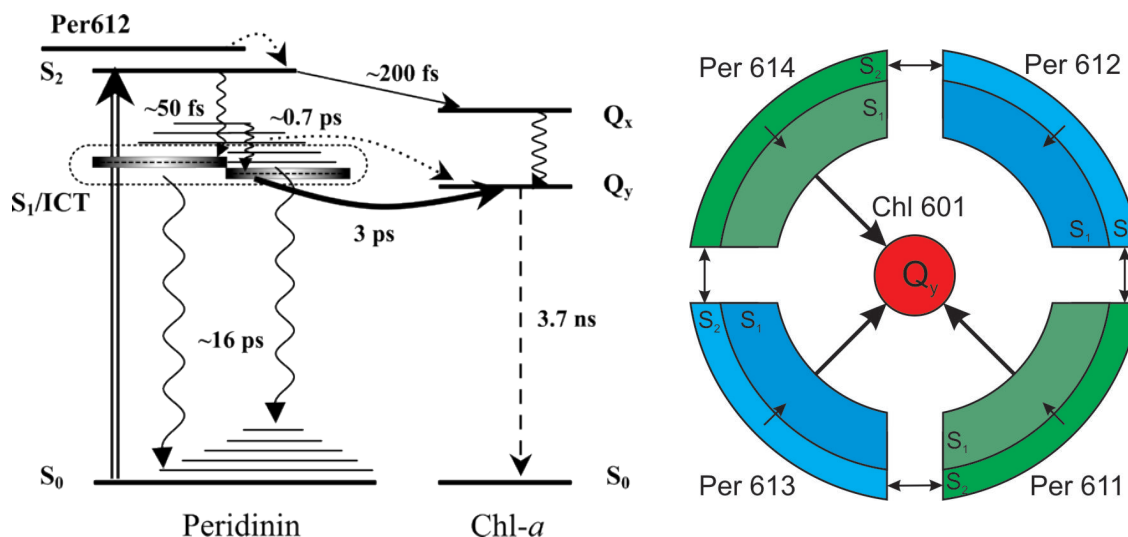


**Figure 3.10:** Left: Scheme of energy levels and energy transfer pathways between Per and Chl *a* in a PCP monomer. Intramolecular relaxation processes are denoted by wavy arrows, while the dashed arrow represents the long-lived Chl *a* fluorescence. Solid arrows represent main energy transfer channels. The dotted arrows represent possible minor energy transfer channel involving higher vibrational levels of the  $S_{1/ICT}$  state and the  $S_2-S_2$  energy transfer involving the Per with blue-shifted absorption spectrum. Excitation is shown as a double arrow. All processes are labelled by the corresponding time constant. From [84]. Right: Energy transfer in a single N-PCP cluster. Shown are the pigments Per 611-614 and Chl 601 colour-coded with their respective excitation wavelength (Table 3.2).

SMS removes ensemble averaging and, as will be discussed, allows for monitoring interactions of single weakly coupled fluorescing Chls with neighbouring pigments and their local protein environment. The efficient Per-Chl energy transfer is utilised as an excitation channel for the spectroscopic investigations. The availability of reconstituted homo- and hetero-chlorophyllous N-PCP allows to follow pigment interactions as a function of structure.



# CHAPTER 4

---

## Materials and Methods

---

This chapter describes the sample preparation and experimental procedures that have been applied in the course of spectroscopic investigations of the light-harvesting complex PCP. Section 4.1 presents the protocol used for biochemical reconstitution of PCP with various Chls, which results in complexes containing either two identical Chls (homo-chlorophyllous PCP) or two different Chls (hetero-chlorophyllous PCP). The sample preparation method for the optical experiments is given in Section 4.2 which is followed by a description of the experimental setups for ensemble and single-molecule-spectroscopies in Sections 4.3 and 4.4, respectively. The experimental approach presented in Section 4.5 adopts the efficient energy transfer between Pers and Chls in PCP as an excitation channel.

### 4.1 Reconstitution of PCP

PCP can be reconstituted from N-domain coding region apoproteins mixed with pigments extracted from native PCP [94, 95]. The possibility of reconstituting PCP complexes with Chls or mixtures of Chls provided a valuable tool to systematically study energy transfer between its pigments as a distinct function of structure. This work was conducted in close collaboration with the group of Prof. H. Scheer (Dept. of Biology, LMU).

#### 4.1.1 Extraction and Purification of N-domain Apoprotein

In a first step N-domain apoprotein was prepared from a 1l culture of *E. coli* JM109 on a pND707 plasmid. The culture was grown in a fermenter at 37 °C to an optical density of 0.8 at 600 nm, at which time protein expression was induced by rapidly increasing the temperature to 43 °C. After 3 h at 43 °C, cells were harvested (5000 g, 30 min) by centrifugation, resuspended in 10 ml of lysis buffer (50 mM Tris 1 mM EDTA pH 8.0 + 25 % Sucrose) and lysed by four passages through a French Press (15000 psi). The centrifugation (31000 g, 15 min) of the lysates resulted in pelleting of recombinant inclusion bodies. In order to remove the

contaminants from the inclusion body preparation, initial pellets were resuspended in lysis buffer and centrifugated at 12000 g for 15 min. Three cycles and centrifugation (10000 g, 15 min) were then performed in Tris buffer (50 mM, pH 8) containing EDTA (1 mM). Following the addition of 4 ml of 50 mM Tris, 1 mM EDTA at pH 8.0, the inclusion bodies were extracted on boiling water for 20 min. N-domain apoprotein was harvested by centrifugation at 33000 g for 30 min and collected as supernatant. Purity and the size of the apoprotein were tested by SDS-PAGE with SDS-7 (Sigma) as the marker. The apoprotein was characterised by circular dichroism between 190 - 300 nm (see Chapter 5 and 6). From the initial 1 l culture a concentration of about 1.986 mg ml<sup>-1</sup> of N-domain apoprotein (~16 kDa) could be collected.

#### 4.1.2 Materials for Reconstitution

Trimeric PCP was isolated from *A. carterae* [7]. Per was extracted from thylakoid membranes of *A. carterae* as previously published in [72]. Chl *a* was extracted from spraydried *Spirulina geitleri*, and Chl *b* was extracted from frozen spinach and purified over DEAE cellulose [111], acChl *a* was synthesized from bacterio-chlorophyll (BChl) *a* (from *Rhodobacter sphaeroides* (R26)) and purified by Sepharose CL-6B chromatography [112].

#### 4.1.3 Homo- and Hetero-Chlorophyllous Reconstitution

Reconstitution followed the protocol described in [94]. 200 - 400 µg of N-domain apoprotein of PCP (0.32 mg ml<sup>-1</sup> or 1.99 mg ml<sup>-1</sup>) in 50 mM Tris 1 mM EDTA pH 8.0 was combined with tricine buffer (25 mM, pH 7.6) containing KCl (10 mM) and adjusted to achieve a total volume of reconstitution equal to 1000 µl. Following the addition of peridinin (12 nmol) and chlorophyll mixtures in 150 µl ethanol, 1 ml of the mixture was incubated at 4 °C for 24 hours. The homo-chlorophyllous mixtures contained a total of 3 nmol of either Chl *a*, Chl *b* or acChl *a*. The hetero-chlorophyllous mixtures contained binary mixtures of these Chls that were added up to yield 3 nmol. The different combination ratios of the Chl pigments were 4:1, 2:1, 1:1, 1:2 and 1:4. The crude reconstitution product was loaded on a small Sephadex G-25 column (5x25 mm) and equilibrated with tricine buffer (25 mM, pH 7.6) containing KCl (10 mM) and eluted with the same buffer. Then it was bounded to a column of DEAE Trisacryl equilibrated with tricine buffer (25 mM, pH 7.6) containing KCl (10 mM) and removed with tricine buffer (25 mM, pH 7.6) containing KCl (10 mM), NaCl step gradient (100, 200, and 500 mM). Fractions containing the reconstituted complex (100 mM NaCl) were dialysed against the starting buffer.

The nomenclature used in the text is as follows: homo-chlorophyllous N-PCP is denoted for example as (Chl *a*)<sub>2</sub>-N-PCP for N-PCP reconstituted with Chl *a*, and hetero-chlorophyllous N-PCP is denoted for example as (Chl *a/b*)-N-PCP for N-PCP reconstituted with both Chl *a* and Chl *b*.

#### 4.1.4 Atomic Coordinates

The crystal structures of native PCP and (Chl *a*)<sub>2</sub>-N-PCP have been solved and the atomic coordinates of native PCP from *A. carterae* are published at the Protein Data Bank (PDB) at <http://www.pdb.org> (identifier 1PPR and [7]). Structure of N-domain (Chl *a*)<sub>2</sub>-N-PCP has also been reported in [113]. All images of various PCP complexes used in this thesis have been produced from the atomic coordinates of native PCP using PyMol from DeLano Scientific LLC at <http://pymol.sourceforge.net/>. Images of reconstituted PCP complexes were obtained by replacing Chl *a* with the respective Chls, assuming that binding geometry is identical to that of the native pigment.

## 4.2 Sample Preparation

### 4.2.1 List of Chemicals

Chemical	description
Tris-EDTA	pH = 7.4, Fluka 93302
PVA	Mowiol 40-88, molecular weight ~127000, Sigma-Aldrich 324590
Water	for luminescence, Fluka 95287
Silver Nitrate	Rectapur, VWR 21570.182
D-(+) Glucose,	99,5% anhydrous, Sigma Aldrich G-7528

**Table 4.1:** Chemicals used in experiments described in the text.

### 4.2.2 Preparation

In order to achieve the concentrations appropriate for single molecule detection, the PCP solutions of about ~0.2 OD at the peridinin-related absorption (~450 nm) were further diluted to pM concentrations in a Tris-EDTA buffer solution or PVA polymer matrix. The appropriate concentration for each sample was found by conducting a dilution series.

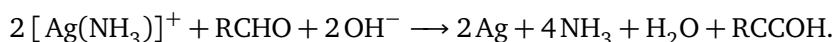
### 4.2.3 Cover Slips and Silver Island Films

Single-molecule spectroscopy demands removal of any fluorescing dust particles that usually contaminate the glass. Thus, all coverslips (Menzel-Gläser No. 1.5, 24x24 mm) were treated with a rigorous cleaning procedure. First, they were placed onto a silicon holder and put into a glass beaker filled with 1 % Helmanex (Hellma GmbH & Co. KG) solution. The solution was sealed with parafilm and kept in a water bath at 60 °C for approximately 30 minutes. Subsequently, the coverslips were ultrasonicated for 5 minutes before being swilled with

distilled water and dried with gaseous nitrogen. Just before applying the sample the surface of the coverslip was flamed with a gas burner.

Samples were immobilised on glass coverslips. The sample was then carefully applied on the coverslip surface by either spincoating or simply pipetting a small drop ( $\sim 20 \mu\text{l}$ ) onto it. In a final step, the coverslip was glued to another glass plate in order to prevent the solution from drying and too rapid oxidation.

Preparation of silver island films (SIF) followed a modified procedure initially published by Ray *et al.* [114]. The overall reaction of this adapted silver mirror reaction reads



0.75 g of silver nitrate were dissolved in HPLC clean water. 3.0 ml of NaOH (5 %) was added while the solution was kept stirring. The resulting grey-brown precipitate was complexated to yield silverdiamin cations (transparent) by addition of concentrated ammonia. Subsequently, the transparent solution was cooled down to  $5^\circ\text{C}$  and 1.08 g of D-(+)-glucose was added. A silicon holder with 12 Helmanex-cleaned coverslips was placed in the stirring solution and kept cooled for two more minutes. Within 5 minutes the mixture was allowed to warm up to  $30^\circ\text{C}$  on a heater. Under constant stirring the solution changed colour from yellow, over green to dark grey and a silver mirror precipitated at the walls of the beaker. The coverslips were then removed, thoroughly cleaned with luminescence-free water and put into an ultrasonic cleaner for 5 minutes. The coverslips were then dried and treated with UV light for 1 h under an Argon atmosphere. This procedure was necessary to bleach away remaining fluorescing

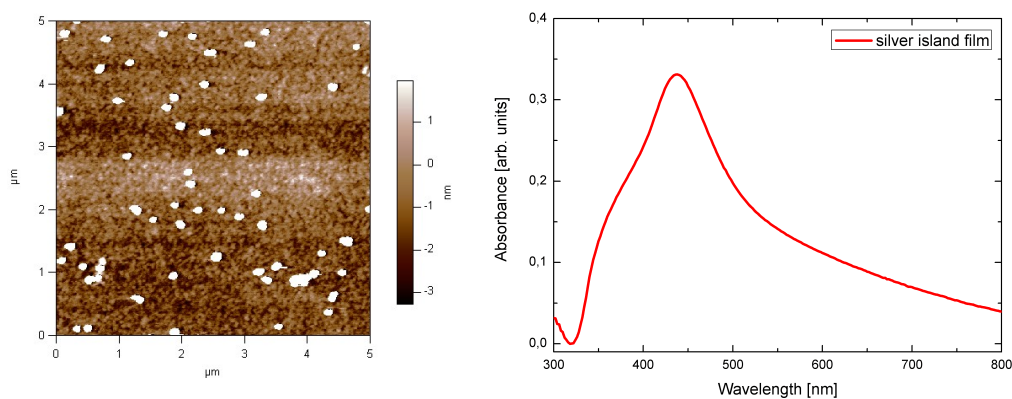


**Figure 4.1:** Left: Atomic force microscopy image of the silver island film (SIF) surface. The diameters of silver islands range from 70 to 140 nm, and their heights are between 30 and 40 nm. Right: Room-temperature absorption spectrum of a microscope coverslip with the SIF layer. The dominant plasmon frequency is observed at  $\sim 440$  nm. The absorption values at 532 nm and 633 nm that correspond to the excitation wavelengths used in the experiments are 0.16 and 0.11, respectively. Absorption is background-corrected with the absorption spectrum of a bare glass coverslip.

dust particles. Coverslips were used in the experiments right after they were fabricated to reduce effects of possible silver oxidation.

As a result of the procedure, the surface of the coverslips is covered with distinct silver islands that feature circular to elliptical shape with typical widths between 70-140 nm and heights in the order of 30-40 nm. Figure 4.1 shows an atomic force microscopy (AFM) image of the SIF coverslip. Plasmon resonance of such prepared SIF coverslips appears at  $\sim 440$  nm (see Figure 4.1).

## 4.3 Ensemble Spectroscopy

PCP samples were characterised at ensemble concentrations at room-temperature using standard spectroscopy methods. Fluorescence emission, excitation and lifetime as well as absorption spectra provided an irreplaceable basis for investigations at single molecule level.

### 4.3.1 Absorption

Absorption measurements on the ensembles were performed using a Cary 50 Cone UV-Vis spectrophotometer (Varian). This instrument incorporates a Xenon flash lamp and allows to scan from 190 to 1100 nm using its built-in software-controlled monochromator. The Xenon lamp flashes only when acquiring a data point and allows for simultaneous reference beam correction. In each case the samples were placed in a quartz cuvette (Helma; centre height: 15 mm). Depending on the initial concentration cuvettes of 3 and 10 mm light-path have been used, holding a volume of 60 and 120  $\mu\text{l}$ , respectively.

### 4.3.2 Fluorescence Spectra and Lifetimes

Fluorescence was measured using a FS-900 fluorimeter from Edinburgh Analytical Instruments, UK. This spectrofluorimeter offers combined steady-state and fluorescence lifetime capabilities. Fluorescence lifetimes were also measured using a home built set-up based on a Nikon Eclipse TE2000-S microscope (collaboration with the lab of Prof. A. Hartschuh, Dept. Chemistry and Biochemistry, LMU). If not stated otherwise fluorescence lifetime was measured using the FS-900.

For steady state fluorimetry the FS-900 fluorimeter is equipped with a 450 W Xenon Arc Lamp (Xe900) allowing for continuous excitation. Two software-controlled monochromators provided the capability to record both emission and excitation spectra. Spectral resolution depends on the slit widths and could be better than 1 nm. Detection photomultiplier was based on the Hamamatsu R928P and featured a spectral response between 200 nm - 870 nm at low dark count rates (typically 50 cps at  $-20^\circ\text{C}$ ). A nanosecond flashlamp excitation source (nF900) under hydrogen pressure (0.42 bar excess pressure) was used for fluorescence

lifetime measurements. Spectral range is from 200 to 850 nm. Pulse width was typically 1 ns (FWHM) at an operating frequency of 40kHz. Time Correlated Single Photon Counting (TCSPC) data acquisition and analysis was achieved using a PCS900 data acquisition card and the F900 software, respectively.

The samples were investigated using the same cuvettes for absorption measurements. However, such an approach was not possible when the samples were prepared on SIF coverslips. For time-resolved measurements in that configuration, a set-up based on a Nikon Eclipse TE2000-S microscope was used. The excitation source was the fundamental frequency beam from a Ti:Sapphire laser system (Coherent Mira, 150 fs pulse width, 75.3 MHz repetition rate) which was coupled into a photonic crystal fibre resulting in generation of a light supercontinuum. A narrow spectral width was cut by a 530/10 nm bandpass filter (Chroma) and the collimated beam with a typical power of 20  $\mu$ W was focused onto the sample by means of a high NA 1.3 immersion oil objective in the inverted microscope Nikon TE 2000 E. The sample fluorescence was collected in epi-illumination configuration, spectrally filtered with 670/10 BP filter (Chroma) corresponding to the sample emission wavelength, and guided to a fast APD (APD - MPD-5CTC Pico Quant). Instrument response function (IRF) had a temporal width of  $\sim$ 27 ps (FWHM). TCSPC technique was achieved using a Becker & Hickl, TCSPC-Board (SPC-140).

## 4.4 Single Molecule Spectroscopy

Single molecule spectroscopy experiments were performed using a modified scanning confocal microscope based on a Zeiss LSM 410. Additional implementations enabled the microscope to be used for both single molecule microscopy and spectroscopy. The set-up has been characterised in detail in [115, 116]. A wide-field microscope was used at a second set-up. It was equipped with a Wollaston prism to record polarisation resolved fluorescence traces. A detailed description of the experimental details can be found in [53].

### 4.4.1 Confocal Setup

The set-up based on the Zeiss LSM 410 is depicted in Figure 4.2. The laser scanning microscope featured a built-in HeNe laser operating at 633 nm (see Table 4.2). Via the backport of the microscope it was possible to align an additional laser excitation source. Nd:YAG was used to provide green excitation at 532 nm (see Table 4.2). The laser beams have been expanded using a telescope and directed via a dichroic mirror to the objective barrel. Maximum intensities were measured at the objective barrel entrance (not attenuated). For single-molecule experiments these values were typically between 1-50  $\mu$ W and were attenuated when needed. High spatial resolution and detection efficiency were achieved using oil-immersion objectives of high numerical aperture (Zeiss 40x 1.3 NA and Zeiss 63x 1.4 NA, immersion oil).

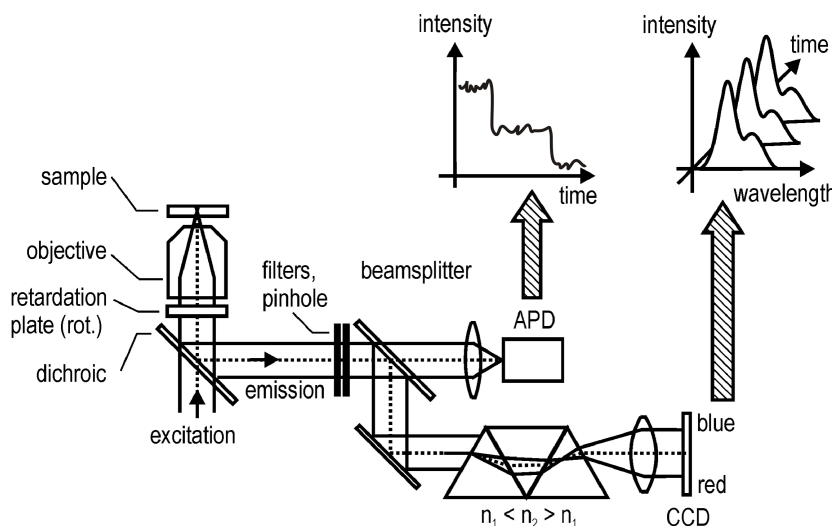


**Figure 4.2:** The confocal set-up based on the laser-scanning microscope Zeiss LSM-410. Excitation and detection of fluorescence was achieved by using the same objective of high numerical aperture. The detection path was modified in order to allow for both imaging with an APD and acquiring spectra with an amici prism and CCD detector.

Red-shifted fluorescence was collected by the same objective and directed back to the dichroic mirror (for red excitation Q640LP, green excitation LP455, AHF Analysentechnik). The beam was then focused through an adjustable pinhole and the fluorescence signal is separated from unspecific reflected and scattered excitation light by band- and longpass filters. After the pinhole, the detection path was split into two beams of equal intensity or alternatively redirected by a mirror. One beam was guided to an avalanche photodiode (EG&G SPCM-AQ 141). The APDs TTL signal was processed by a pulse expander [115] and re-routed to the microscope hardware to record images or intensity transients by scanning the laser over the sample. The configuration of the experimental setup allowed to scan an area up to  $30\ \mu\text{m} \times 30\ \mu\text{m}$  depending on the objective. The second beam was dispersed by an Amici prism and detected with a Peltier-cooled, back-illuminated CCD camera (Princeton Instruments, EEV 1300/100-EMB-chip). Instead of scanning the laser over the sample, the excitation beam can be fixed at a given position. Such a spot scan was used to collect spectra of single molecules. Temporal resolutions of usually 0.3 - 1 s have been used in the experiments on PCP. Spectral resolution of the set-up depends on the dispersion strength of the Amici prism. Non-linear dispersion in the small wavelength region used in the experiments was linearly approximated by: 1 pixel  $\approx$  1.5 nm.

#### 4.4.2 Wide-field Setup

At the wide-field set-up a Cobolt Samba solid state laser operating at 532 nm was used as an excitation source (see Table 4.2). The laser power was attenuated using an OD filter wheel (continous change of OD 0-2, Thorlabs) to yield  $1.6\ \mu\text{W}$  at the objective barrel entrance.

Laser	$\lambda_{exc}$	$I_{exc}$
Nd-YAG, Soliton	532 nm	200 $\mu W$
HeNe, internal, Zeiss GmbH	633 nm	34 $\mu W$
Cobolt Samba, Cobolt AB, Sweden (diode-pumped solid state laser, cw)	532 nm	1.6 mW 100 mW output

**Table 4.2:** Laser sources. Maximum intensities measured at objective barrel entrance (not attenuated).

The beam diameter was focussed using an achromatic lens onto an optical multimode fibre ( $\varnothing$  0.6 mm, Optronics GmbH) which acts as a spatial mode filter and provided elliptical polarisation of the excitation beam. Homogeneous illumination was achieved by vibrating the fiber. An identical achromatic lens was used to achieve parallel light beam and guide it onto a rectangular diaphragm. The diaphragm was imaged using 200 mm wide-field lens (achromat, Thorlabs) onto the back-focal plane of an objective. The parallel beam leaves the objective and illuminates an area of up to 30 x 30  $\mu m$  (ROI: image of the diaphragm). An oil-immersion objective with high numerical aperture (Nikon, CFI Plan Apochromat 100x Oil, N.A. 1.4) assured high excitation and detection efficiency.

Fluorescence was collected by the same objective and guided to a dichroic mirror which was identical to the one used at the confocal set-up for green excitation. Passing a tube lens ( $f=160$  mm) the beam leaving the microscope via a switchable mirror. The parallel beam was filtered by a bandpass filter (670/10 BP, Chroma). A telescope magnified the beam by a factor of 1.33. At the end of its tube a Wollaston prism (Kryptonik Technologies) was placed to split the beam into two orthogonal polarisations. The exiting beams had an angle of  $10^\circ$ . Polarisation-sensitive detection was achieved using a back-illuminated electron multiplying CCD camera (iXon DV887, 512 x 512 pixels, 1 pixel  $\approx$  16  $\mu m$ ) which featured high detection sensitivity. The two different beams of orthogonal polarisation were imaged onto two separated areas on the CCD chip. These two channels were calibrated to match in size and orientation using an analysis software. Thus, it was possible to compare the fluorescence intensities in both polarisation channels at two corresponding positions. This way polarisation traces of individual molecules could be constructed.

## 4.5 Excitation Schemes

In all experiments presented in this thesis, the Chl fluorescence in PCP was detected by their fluorescence emission. Depending on the wavelength, emission of Chls can either be excited by directly tuning the laser into their vibronic bands or indirectly into the broad absorption of PCP and taking advantage of the efficient energy transfer from Pers to Chls (see Figure 3.10).

Direct excitation is achieved with red excitation at 633 nm. Absorption of Per, although rather broad, is in the green/blue part of the spectrum only and thus Pers are not involved in this

excitation scheme. Exciting directly into the chromophore absorption is a common approach found in SMS experiments [11, 17]. However, the observation of spectral changes is often limited by the inhomogeneously broadened fluorescence band of the chromophore [117]. This limitation can be overcome by using the continuous-wave Nd:YAG laser at 532 nm which corresponds to the absorption of Per. In this way Chls are excited indirectly, since in this spectral region the direct absorption of Chls is less than 10%. Chl emission is excited via very efficient energy transfer from Pers. This experimental approach features several advantages. In PCP the absorption at 532 nm is more pronounced than at 633 nm. Chls are efficiently excited through energy transfer from the Pers and excitation laser light can easily be filtered away from the red shifted fluorescence signal. Furthermore, the fluorescence emission of the two Chls in PCP can be simultaneously excited with a single wavelength. This is especially important when studying hetero-chlorophyllous complexes in which the fluorescence of the two different Chl molecules can be separated by about  $400\text{ cm}^{-1}$ . Another advantage is due to the broad absorption of the Pers: spectral changes that occur on a scale much smaller than the inhomogeneous linewidth could be monitored (see Chapter 5).



# CHAPTER 5

---

## Spectroscopy of Homo-Chlorophyllous PCP

---

This chapter presents results obtained for the homo-chlorophyllous PCP complexes (Chl *a*)<sub>2</sub>-N-PCP, (Chl *b*)<sub>2</sub>-N-PCP and (acChl *a*)<sub>2</sub>-N-PCP using ensemble spectroscopy and SMS. The experiments utilise excitation of Chl emission via the efficient energy transfer from Per to Chl. The results of ensemble spectroscopy described in Section 5.1 highlight how reconstitution with different Chls tunes the optical properties of N-PCP. Absorption and circular dichroism spectra show spectral features clearly attributable to the Chl pigments used during reconstitution. Besides a detailed characterisation of the samples, absorption and fluorescence spectra provide the parameters needed to model energy transfer in PCP. Fluorescence excitation spectra show that high efficiency of the energy transfer between Per and Chl in native PCP is preserved for all N-PCPs. Section 5.2 introduces results obtained at the single molecule level on the same set of complexes. SMS allows for direct insight into spectral properties of individual PCP complexes. Spectra of both single native and reconstituted PCP presented in Section 5.3 exhibit stepwise photobleaching of fluorescence emission, which suggests very weak dipole-dipole coupling between the Chls in a monomer. This conclusion is further supported by polarisation-resolved fluorescence emission traces described in Section 5.4. The influence of solvents and effects of spectral dynamics are considered in Sections 5.5 and 5.6, respectively.

### 5.1 Ensemble Spectroscopy

Ensemble spectroscopy is used to characterise N-PCP reconstituted with Chl *a*, Chl *b* and acChl *a* and determine the photo-physical properties required to describe and understand the energy transfer pathways in the hetero-chlorophyllous complexes.

#### 5.1.1 Absorption and Circular Dichroism

Figure 5.1 shows absorption and circular dichroism (CD) spectra of homo-chlorophyllous PCP complexes. The homo-chlorophyllous N-PCP complex containing Chl *a*, i.e. (Chl *a*)<sub>2</sub>-N-PCP, has absorption and CD spectra similar to those of native PCP [100]. However, the

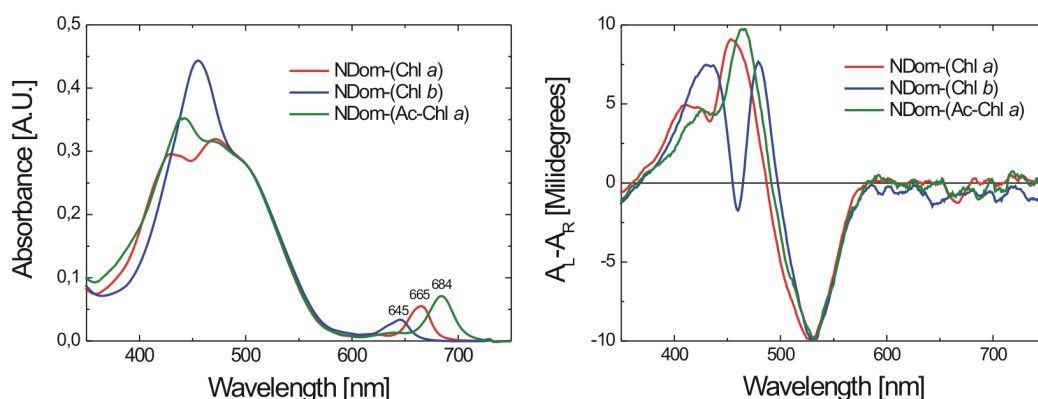


**Figure 5.1:** Left: Absorption spectra of N-PCP reconstituted with Chl *a*, Chl *b* and acChl *a*, respectively. For comparison the spectra are normalised into Per absorption maximum at 505 nm. Right: Circular dichroism spectra of the same set of complexes normalised into the negative extremum of Per at 532 nm.

negative CD-band of Per peaking around 530 nm is slightly red-shifted and broadened in (Chl *a*)<sub>2</sub>-N-PCP as compared to native PCP. The CD-spectrum of both complexes is dominated by an intense, s-shaped band peaking at 530 nm (-) and ~445 nm (+), with the zero-crossing near the absorption maximum of Per. Superimposed on the positive lobe of this signal is a much smaller and narrower, s-shaped band centred near the absorption maximum of Chl *a*. Its negative lobe shows as a dip in the intense positive Per band located ~7 nm to the red of the Chl *a* absorption maximum (437 nm). The positive lobe is discernible as a distinct peak in the largely unstructured Per band, located 10 nm to the blue of the Chl *a* absorption maximum. There is no such splitting for the Q<sub>y</sub>-band of Chl *a* at ~672 nm. The major band of Chl *a* in the Soret-region is the B<sub>x</sub>-band [118, 119]. Since the orientation factors  $\kappa$  are similar for the *x*- and *y*-polarised transitions, the lack of a split Q<sub>y</sub> CD-signal indicates that the split Soret CD-signal is not due to excitonic interactions among the Chls of adjacent pigment clusters, but results mainly from coupling with Per within a single cluster [100, 101]. The presence of acChl *a* instead of Chl *a* results in similar absorption and CD spectra of the (acChl *a*)<sub>2</sub>-N-PCP complex, as seen in Figure 5.1. However, Q<sub>y</sub>-band is red-shifted, as in acetone solution, compared to that of Chl *a*. Soret band is more pronounced as compared to (Chl *a*)<sub>2</sub>-N-PCP. These spectral features are reflected in very similar CD spectra as well.

Reconstitution with Chl *b* yields a complex with a blue-shifted Q<sub>y</sub>-band of the Chl and a red-shifted Soret band (see Figure 5.1), these shifts are similar to those of Chl *b* in acetone (see Figure 3.3). The red-shifted (460 nm) and more pronounced Soret band reflects the larger extinction coefficient of Chl *b* as compared to Chl *a* [120]. Accordingly, the absorption of the Chl *b* complex is dominated by the latter (460 nm). The s-shaped CD signal in the Soret region is also much more prominent than in the Chl *a*-containing complex. This was shown already by Miller *et al.* [94]. The zero-crossing of the intense, s-shaped feature is close to the Chl *b* absorption maximum. The Q<sub>y</sub>-band shows, like in the Chl *a* complex, no

splitting. This further supports that excitonic interactions of the Chls occur mainly with Per [100, 101].

### 5.1.2 Fluorescence Emission Spectra

The fluorescence emission spectra measured for ensembles of homo-chlorophyllous N-PCP reconstitutions excited at 532 nm are shown in Figure 5.2. For comparison the spectra are normalised to the respective fluorescence maxima. In all three cases, the emission consists of a single narrow line positioned at 652 nm ((Chl *b*)<sub>2</sub>-N-PCP), 672 nm ((Chl *a*)<sub>2</sub>-N-PCP), and 692 nm ((acChl *a*)<sub>2</sub>-N-PCP). All three homo-chlorophyllous complexes feature vibronic side wings to the red. At the excitation wavelength of 532 nm emission of the Chls is mainly excited via the efficient energy transfer from Per to Chls, as discussed in Chapter 3.5. However, as apparent from Figure 3.3, Chl *b* features a notably higher absorbance at 532 nm. This leads to additional direct excitation and explains the higher intensity of vibronic bands in (Chl *b*)<sub>2</sub>-N-PCP) as compared to the other reconstitutions.

### 5.1.3 Fluorescence Excitation Spectra

Fluorescence excitation spectra can be used to quantify energy transfer efficiencies [1]. By scanning the excitation wavelength the spectra reveal the energy transfer pathways present in a complex. The left panel of Figure 5.3 shows the excitation spectra of all three homo-chlorophyllous N-PCP complexes normalised to the mainly Per-related absorption maximum

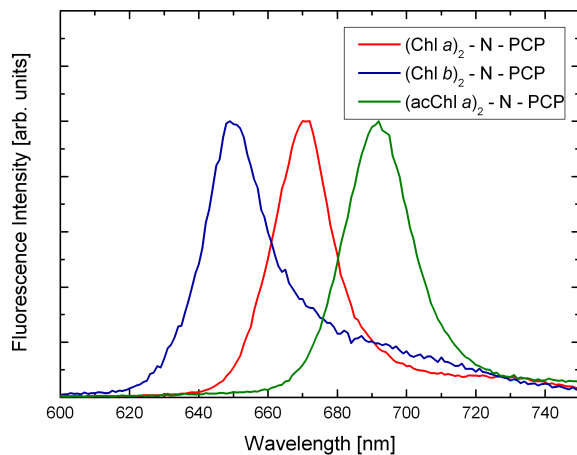


**Figure 5.2:** Normalised room temperature ensemble fluorescence spectra of homo-chlorophyllous N-PCP complexes: (Chl *a*)<sub>2</sub>-N-PCP (red), (Chl *b*)<sub>2</sub>-N-PCP (blue), and (acChl *a*)<sub>2</sub>-N-PCP (green). The excitation wavelength was 532 nm in all cases.

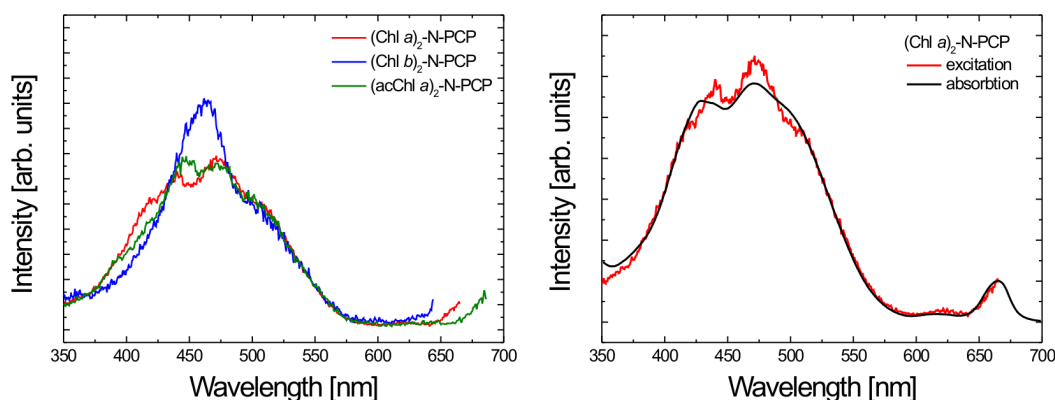


**Figure 5.3:** Left: Fluorescence excitation spectra of homo-chlorophyllous N-PCP complexes: (Chl *a*)<sub>2</sub>-N-PCP (red), (Chl *b*)<sub>2</sub>-N-PCP (blue), and (acChl *a*)<sub>2</sub>-N-PCP (green). Detection is tuned into respective Q<sub>y</sub> fluorescence maxima. Right: Overlap of excitation and absorption spectra of (Chl *a*)<sub>2</sub>-N-PCP. Both spectra are normalised to Q<sub>y</sub> absorption maximum.

at 505 nm. Detection is placed at the respective Q<sub>y</sub> emission maxima. The spectra of all reconstituted homo-chlorophyllous complexes feature similar shape compared to their absorption spectra in Figure 5.1. Soret- and Q<sub>y</sub>-bands are clearly visible. This is a clear indication of the energy transfer between Pers and Chls. The energy transfer efficiency can be quantified from a comparison with the absorption spectrum. The right panel of Figure 5.3 shows an overlap of excitation and absorption spectra of (Chl *a*)<sub>2</sub>-N-PCP normalised to Q<sub>y</sub>-band. The relative amplitudes of excitation and absorption spectra indicate the energy transfer efficiency at a given wavelength. (Chl *a*)<sub>2</sub>-N-PCP and similarly all other homo-chlorophyllous reconstitutions (data not shown) feature large spectral overlap of absorption and excitation spectra. Thus, the high energy transfer efficiency from PCP is preserved in reconstituted N-PCP [103]. This is an important result as most of the experiments presented in this thesis, in particular SMS, rely on the very efficient energy transfer from Per to Chl as an excitation channel.

The spectral variations lead to changes in overlap with the Per emission and is partially responsible for the recently observed changes in the excitation transfer from Per to Chl in homo-chlorophyllous samples [87]. The spectral similarity of absorption and excitation allows to qualitatively deduce different energy transfer efficiencies from Per to the respective Chls. The absorption spectra in Figure 5.1 are essentially equivalent to excitation spectra of the same complexes. Thus, the different relative intensities apparent at the Q<sub>y</sub>-bands are an indication of Per to Chl transfer efficiency. The highest peak indicates that Per to acChl *a* energy transfer is more efficient than Per to Chl *a* efficiency as the corresponding Q<sub>y</sub>-band features lower intensity. On the other hand, Per to Chl *b* transfer features the lowest efficiency. These observations are in agreement with time-resolved measurements [87] as discussed already in Chapter 3.5.

## 5.1.4 Fluorescence Lifetime and Quantum Yield

Besides absorption and emission spectra, fluorescence quantum yields and lifetimes are important photo-physical parameters and essential to calculate Förster energy transfer rates. Fluorescence decay of homo-chlorophyllous PCP was measured by TCSPC and is shown in the left panel of Figure 5.2. The points represent experimental data, the solid lines correspond to curves fitted assuming a mono-exponential decay of the fluorescence. Fluorescence decay of all three homo-chlorophyllous complexes could be reasonably well fitted resulting at a reduced  $\chi^2 \approx 1$ . The emission of Chl *a* in N-PCP is characterised by a time constant of  $\tau = 3.7$  ns, which is shorter than the fluorescence decay time of Chl *a* emission in the native PCP complex ( $\tau = 4.2$  ns [66]). This difference is most probably due to the different protein surroundings as the reconstituted PCP does not include the C-terminal domain of the native system [7]. Decay of acChl *a* in N-PCP is comparable to Chl *a* ( $\tau = 3.8$  ns). Lifetime of (Chl *b*)<sub>2</sub>-N-PCP is shortest ( $\tau = 1.4$  ns). The fluorescence lifetimes obtained for all Chl pigments embedded in N-PCP are thus significantly shorter than in acetone (see Table 3.1) which is likely due to the polarity inside the protein capsule [84]. Table 5.1 summarises the photo-physical properties of all three Chl molecules in refolded N-PCP.

The fluorescence quantum yields were determined by comparison with a dye of known quantum yield following a comparative method by Williams *et al.* [121]. Solutions of a given test sample and a well-characterised standard sample of identical absorbance absorb the same number of photons at a given excitation wavelength. Thus, a simple ratio of fluorescence intensities  $F/F_{ref}$  of the two samples is proportional to the ratio of quantum

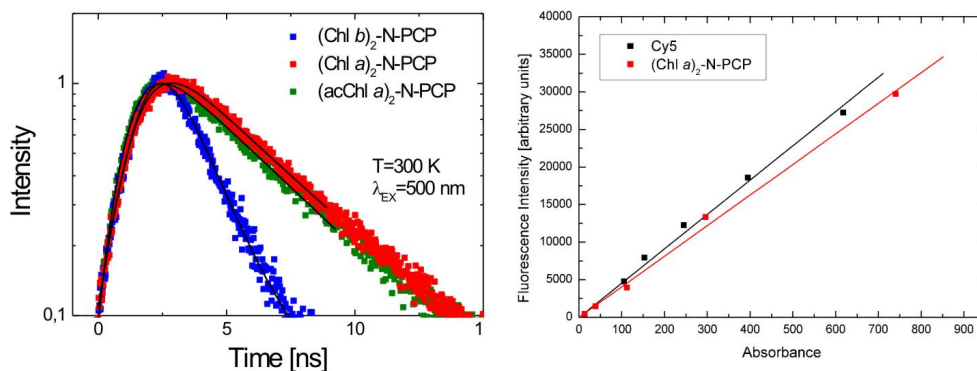


**Figure 5.4:** Left: Fluorescence decay of the three homo-chlorophyllous complexes. Fit to mono-exponential function is shown in black. Right: Fluorescence intensities vs. absorbance of different dilutions of Cy5 (in black) and (Chl *a*)<sub>2</sub>-N-PCP (in red). The ratio of the respective gradients of the plots from a linear fit determine the quantum yield.

Pigment	Chl <i>a</i>	Chl <i>b</i>	acChl <i>a</i>
Fluorescence emission $\lambda_{max}$	672	651	692
Extinction coefficient $\varepsilon [mM^{-1}cm^{-1}]$	78.8 at 662 nm	46.9 at 644 nm	65.2 at 667 nm
Fluorescence lifetime $\tau [ns]$	3.68	1.4	3.84
Fluorescence quantum yield $\Phi_f [\%]$	24	11	21
Per-to-Chl transfer time $t(Per - Chl) [ps]$	3.55	9.4	2.55

**Table 5.1:** Photo-physical parameters of the three Chl pigments in homo-chlorophyllous complexes. The Per-to-Chl energy transfer times in N-PCP were taken from [87]

yields:

$$q = \frac{F}{F_{ref}} \frac{n^2}{n_{ref}^2} q_{ref}, \quad (5.1)$$

where  $n$  and  $n_{ref}$  are the refractive index of the test and reference, respectively.

In practice, a couple of requirements need to be met to achieve reliable quantum yield values. First, both test and reference dye must be excitable at a given excitation wavelength. Concentrations should be low enough to avoid effects like self-quenching. Secondly, because of typical wavelength-dependent transmission characteristics of fluorescence spectrometers, a sufficient spectral overlap of test and reference dye has to be assured. In order to determine the quantum yield of (Chl *a*)<sub>2</sub>-N-PCP Cyanine 5 (Cy5) was used (Amersham). This dye meets all the requirements. Cy5 is a reactive fluorescent dye of the cyanine dye family. Cy5 has excitation peaks at 649 nm (absorption overlap with PCP is sufficient) and emission maximum is at 670 nm, quantum yield is 0.28. Similar to PCP, the dye is water-soluble, thus correction for different refractive index of the solvent can be omitted. Figure 5.4 (right panel) shows a plot of fluorescence intensities vs. absorbance for Cy5 and (Chl *a*)<sub>2</sub>-N-PCP for different dilutions. In a similar fashion, all remaining reconstituted homo-chlorophyllous PCP complexes were measured. (Chl *a*)<sub>2</sub>-N-PCP served as the reference dye. The results are summarised in Table 5.1.

## 5.2 Single Molecule Spectroscopy

More detailed insight into the distribution of optical parameters of N-PCP is possible by SMS. It allows to monitor intrinsic inhomogeneities of photophysical parameters of chromophores, such as fluorescence lifetimes and/or emission frequency [19] of individual complexes and relate them e.g. to protein dynamics. Fluorescence emission of single PCP molecules is excited by Per absorption at 532 nm and subsequent energy transfer to Chls. The results obtained on homo-chlorophyllous complexes provide a reference required for understanding the single molecule experiments carried out on N-PCP reconstituted with Chl mixtures. Furthermore, SMS allows insight into Chl-Chl coupling and solvent effects on stability of the native PCP complex.

### 5.2.1 Native PCP

The results of SMS obtained on native PCP complexes in Tris EDTA buffer is summarised in Figure 5.5. The upper left panel shows a typical 30  $\mu\text{m}$  by 30  $\mu\text{m}$  confocal-micrograph. The bright spots correspond to fluorescence emission of single complexes, each containing six Chl *a* molecules [7]. The images of the molecules are Gaussian shaped and feature almost no blinking during the scan. A clear proof that the spots indeed correspond to single complexes is possible via their step-wise bleaching characteristics. The extraordinarily bright spot visible on the left side of the image is most probably a higher aggregate of native PCP. Such aggregates could easily be distinguished from single complexes based on their photobleaching behaviour. In contrast to single molecules the aggregates feature an exponential decay of fluorescence intensity reminiscent of the ensemble behaviour. The upper right panel of Figure 5.5 shows a representative fluorescence spectrum of a single PCP complex. It consists of a single intense line, whose lineshape is well reproduced by a single Gaussian fit represented with a red solid line.

The advantage of SMS is that with this approach one can record distributions of spectral parameters instead of just average values. The lower left panel of Figure 5.5 shows a histogram of emission energies of over 150 single native PCP complexes. Although the fluorescence emission wavelength exhibits some variation from complex to complex, the maximum of the overall distribution ( $\lambda = 673.5 \text{ nm}$ ) corresponds well to the energy measured at ambient temperature for PCP ensemble. This correlation indicates that the photo-physical properties of single PCP complexes are not affected by the surface and/or preparation procedure in any significant way. Another parameter characteristic to single molecules is the bleaching time. Each individual complex shows fluorescence only until it irreversibly photobleaches. The lower right panel of Figure 5.5 shows a histogram of bleaching times obtained for over 150 single native PCP complexes. Fluorescence of single PCPs is remarkably stable and, apart from some occasional blinking, the signal could frequently be observed for tens of seconds. The solid line represents a single exponential fit, which yields the average survival time of native PCP fluorescence to be around 29 s at excitation power  $\sim 1 \mu\text{W}$  in Tris EDTA buffer.

### 5.2.2 Homo-Chlorophyllous N-PCP

In contrast to the native PCP, which is predominantly a trimer, the reconstituted PCP complexes are expected to form monomers each containing two Chls. Trimerisation of N-PCP is prohibited because of the missing C-terminal domain that is needed to promote binding of the monomers into trimers [7]. Recently, direct proof of that has been reported by solving the crystal structure of  $(\text{Chl } a)_2\text{-N-PCP}$  [113]. The complexes indeed form monomers almost structurally identical to monomeric subunits in native PCP. The left panel of Figure 5.6 shows examples of the fluorescence spectra of the three single PCP complexes reconstituted with Chl *a*, with Chl *b*, and acChl *a*. All homo-chlorophyllous reconstitutions feature single, well-resolved and narrow lines. In these experiments PVA polymer layer was used instead of

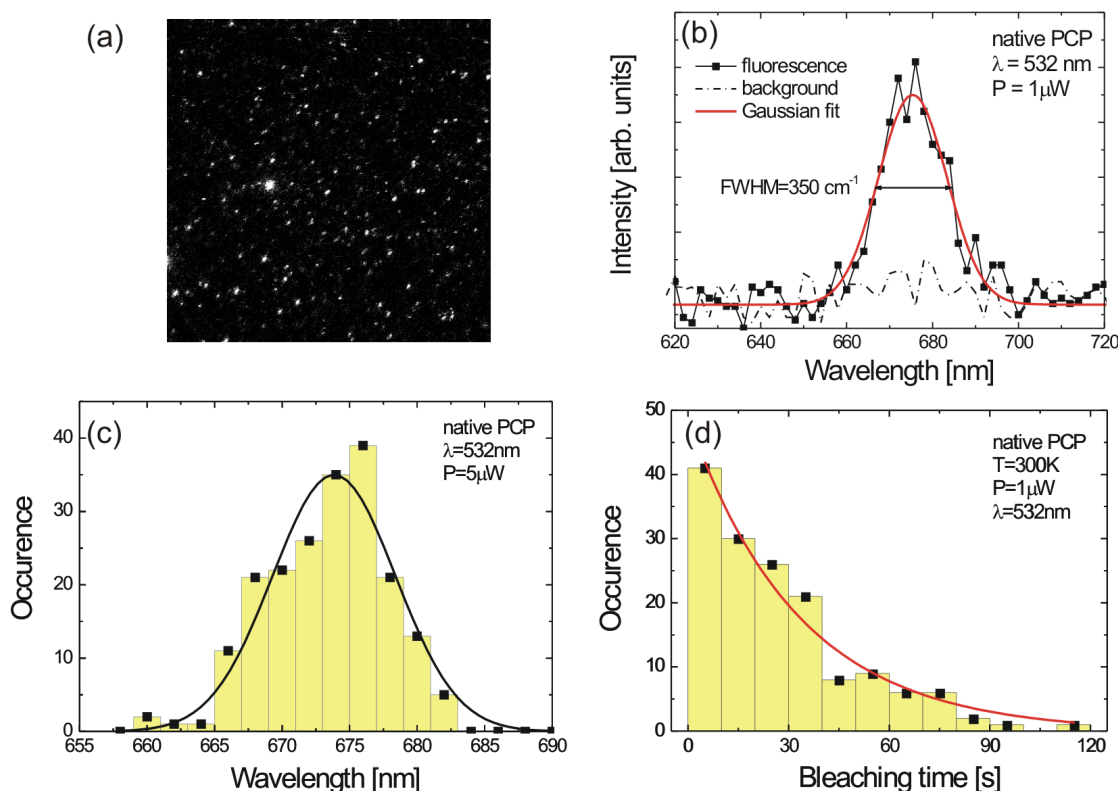


**Figure 5.5:** Summary of SMS results obtained for native PCP: (a) 30  $\mu\text{m}$  by 30  $\mu\text{m}$  image showing the fluorescence of single PCP complexes excited at 532 nm. (b) Fluorescence spectrum of a single native PCP complex (points). Solid line represents the Gaussian fit, for comparison the background is also displayed. (c) Histogram of fluorescence emission wavelengths measured for over 150 single native PCP complexes. The solid line is the ensemble spectrum. (d) Histogram of bleaching times obtained for over 150 single PCP complexes. The solid line is an exponential fit to the data.

Tris EDTA. It turned out that PCP complexes are more photostable in this environment (see Chapter 5.5). The right panel of Figure 5.6 displays the distributions of maximum emission wavelength of the same set of complexes each measured for  $\sim 100$  molecules. As expected from the ensemble fluorescence spectra, all three distributions are spectrally well-separated and on average resemble fluorescence maxima at around 652 nm, 673 nm and 692 nm, respectively.

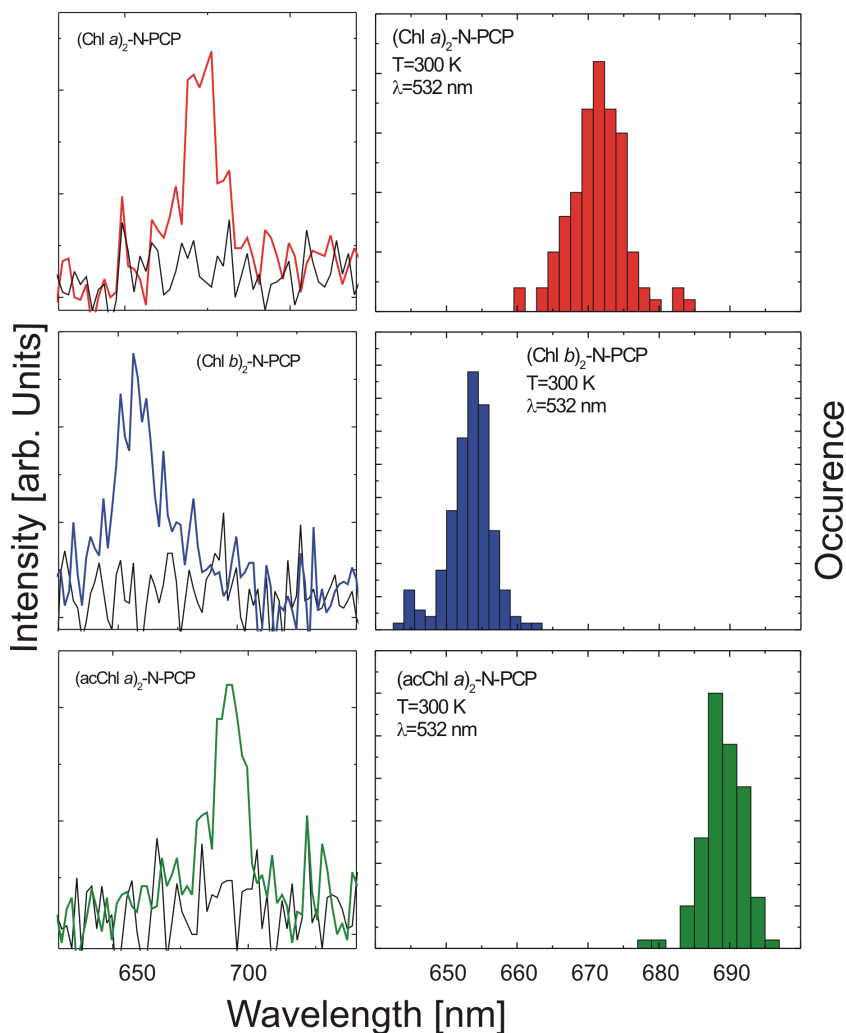


**Figure 5.6:** Left: Representative fluorescence spectra of single PCP complexes:  $(\text{Chl } a)_2\text{-N-PCP}$  in red,  $(\text{Chl } b)_2\text{-N-PCP}$  in blue and  $(\text{acChl } a)_2\text{-N-PCP}$  in green. Right: Distributions of single molecule spectra resemble ensemble emission spectra.

### 5.3 Stepwise Photobleaching

Photobleaching of single N-PCP complexes does not occur in a single distinct step. The left panel of Figure 5.7 shows a sequence of 25 fluorescence spectra measured subsequently for a single PCP complex reconstituted with Chl *a*. The acquisition time of a single spectrum was 0.3 s. An intensity trace obtained for this complex by fitting every spectrum with a single Gaussian line is displayed in the right panel of Figure 5.7. The trajectory features two clear intensity steps, a behaviour observed for approximately 70 % of single PCP complexes of all reconstituted N-PCP complexes. It is to some degree surprising that the fluorescence intensity measured consecutively with the acquisition time of 0.3 s features such a regular bleaching behaviour.

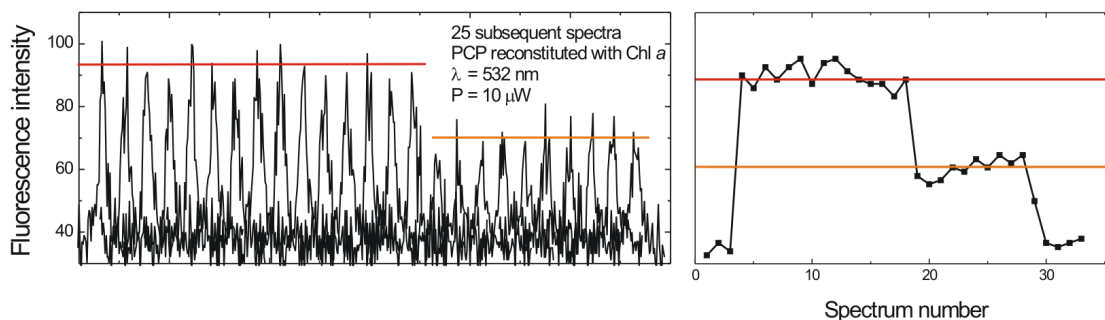


**Figure 5.7:** Representative fluorescence intensity trace measured for a single PCP complex reconstituted with Chl *a*. Left: Sequence of fluorescence spectra measured for a single complex. The averaging time is 0.3 s per spectrum. Right: Corresponding time trace of the fluorescence intensity. Two well-defined levels of the intensity could be identified, as indicated by horizontal lines.

Limited blinking of individual Chl molecules during the measurement could be due to extremely efficient Per quenching of Chl triplet state in PCP [100, 104].

Along with the emission intensity, the fluorescence spectra of the complexes were measured. As an example, Figure 5.8 shows the fluorescence spectra of two single PCP complexes reconstituted with Chl *a* in the upper and lower row. Both complexes exhibit two-step bleaching of the emission intensity, similar to the situation discussed above. The spectra were taken in the sequence indicated by the numbers, and the stepwise drop of the intensity is presented in the central graph of each set. Clearly, in both cases the drop in fluorescence intensity is precisely correlated with pronounced changes in the fluorescence spectrum. It appears as each of the two steps seen in the fluorescence intensity trajectory is due to removal of an individual chromophore that contributes to the emission. Therefore, the combination of intensity and spectral information provide a way to unambiguously attribute the stepwise decrease of the fluorescence intensity to subsequent bleaching of two distinguishable Chl *a* molecules within the PCP monomer. Importantly, as displayed in Figure 5.8, the bleaching of one of the Chl molecules does not affect either energy nor intensity of the fluorescence attributed to the second Chl. The presence of two distinguishable spectral lines in a single complex is a direct consequence of the excitation scheme applied in the experiments. The Förster energy transfer between Chl *a* molecules of about 10 ps [66] is slow compared to the time characteristic for the energy transfer from Per to Chl. Thus, both Chls are independently excited via energy transfer from the Pers.

These results allow to conclude on the coupling between the Chls within a PCP monomer. The observation of subsequent bleaching of the two Chl *a* molecules in reconstituted PCP complexes, together with the insensitivity of the fluorescence emission of the second Chl to the bleaching of the first one, demonstrates weak dipole-dipole coupling between the Chls within a PCP monomer. Weak coupling is supported by the structural parameters obtained from the crystal structure, namely the large Chl-Chl distance of 17.4 Å and the relative orientation of the two Chl dipoles of 116°. On the contrary, strong coupling between Chls should result in a

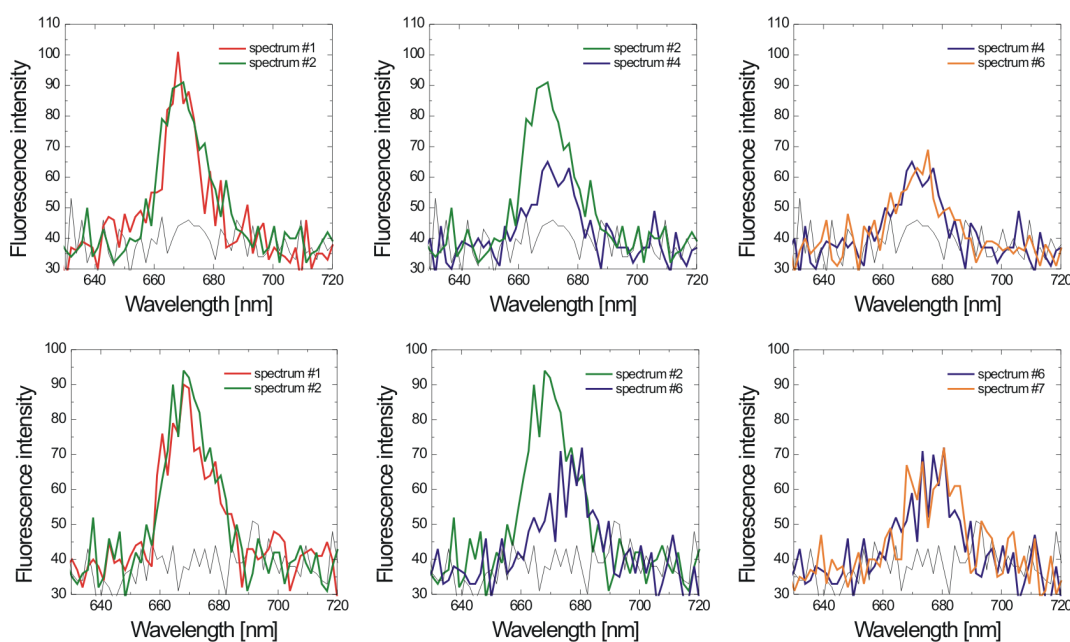


**Figure 5.8:** Relevant parts of fluorescence spectra sequences measured for two different PCP complexes reconstituted with Chl *a*. The upper row shows a complex with small splitting between the chlorophyll emissions, while in the bottom row the splitting is relatively large. The spectra in each case are numbered according to the sequence they were taken. The graphs in the middle display the drop in the fluorescence intensity.

different bleaching behaviour. For example it has been shown that oxidised BChl molecules are very efficient quenchers of the fluorescence in light-harvesting complexes [117, 122]. Thus, upon bleaching of one Chl molecule, the fluorescence intensity of the second Chl should be dramatically reduced [122]. Following the discussion in Chapter 2.2, strongly interacting fluorophores might even form an exciton. In fact, for a pair of strongly interacting Chls the fluorescence intensity would photobleach in just a single step. Such a situation has been observed for another water-soluble photosynthetic complex, APC [123], and the LH2 complex [124, 125].

In conclusion, the results demonstrate that in N-PCP one can independently monitor the fluorescence of the two weakly coupled Chls within the monomer via excitation through energy transfer from Pers. The advantage of monitoring the fluorescence of two independent Chl molecules within a single complex is having a way to estimate the individual contributions to the emission intensity. Figure 5.9 shows an analysis of (Chl *a*)<sub>2</sub>-N-PCP complexes in Tris EDTA buffer showing two-step photo-bleaching. The histograms displayed in the left panel show fluorescence intensities measured from single molecule spectra before and after the first Chl bleached away, i.e. for both and only one emitting Chl *a* molecule(s), respectively. By dividing the two, a distribution of intensity ratios is obtained, as displayed in the right panel of Figure 5.9. Apparently, the ratio is  $1 \pm 0.1$  for the majority of (Chl *a*)<sub>2</sub>-N-PCP complexes,

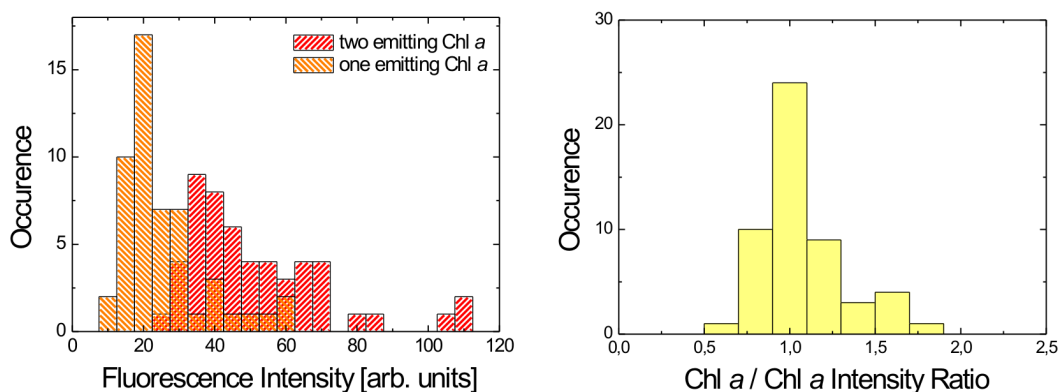


**Figure 5.9:** Distribution of fluorescence intensities measured for single  $(\text{Chl } a)_2\text{-N-PCP}$  Left: Shown in red (right shading) are the intensities of two emitting Chl  $a$ . Similarly, shown in orange (left shading) the intensities of one Chl after the other photo-bleached. Right: Experimentally determined distribution of the intensity ratio between emissions of two Chl  $a$  and of one Chl  $a$  in the complexes at room temperature. The excitation power was  $3 \mu\text{W}$ .

which indicates that the contributions of the two Chl  $a$  molecules to the fluorescence of a single PCP complex are almost identical. Moreover, such a narrow spread of intensity ratios suggests that most of the complexes attach similarly - as far as the orientation of the transition dipole moments is concerned - to the cover-slip. Similar behaviour has also been observed for PCP complexes reconstituted with Chl  $b$  and acChl  $a$ .

The spectra of  $(\text{Chl } a)_2\text{-PCP}$ , displayed in Figure 5.8, demonstrate also that two Chl  $a$  molecules within a reconstituted PCP complex can feature significant energy separation. Figure 5.10 presents a distribution of the energy splitting between the two Chl  $a$  molecules obtained for over 120 complexes. The vast majority of the complexes feature a measurable splitting, that could frequently reach  $280 \text{ cm}^{-1}$  which is comparable to the linewidth of the fluorescence emission. This result shows that, in agreement to the findings based on the ensemble spectroscopy [108], the two Chls in PCP can be energetically distinguishable due to moderate differences in their immediate surroundings, which might, in turn, represent local minima in the folding energy landscape of the holoprotein that do not equilibrate during the measurement. Importantly, this effect can only be observed for a system where due to weak interaction between the chromophores it is possible to independently monitor their fluorescence.

Fluorescence trajectories measured for single native PCP complexes, which contain six Chl  $a$  molecules, also exhibit intensity steps, similarly to the behaviour observed for PCP reconstituted with Chl  $a$ . Figure 5.11 shows a series of subsequent fluorescence spectra and extracted intensities recorded for a single native PCP complex. Clearly, the fluorescence intensity decreases with time and features stepwise behaviour. Tentatively, five intensity steps can be distinguished, marked by horizontal lines in the right panel of Figure 5.11. However, due to three times higher number of emitting Chls, an estimation of the exact number of intensity

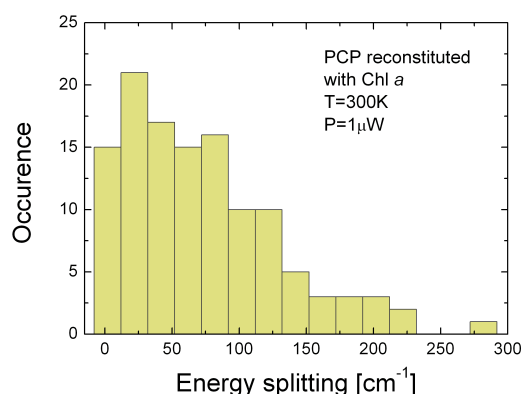


**Figure 5.10:** Statistical distribution of the energy splitting determined for over 120 single PCP complexes reconstituted with Chl *a*.

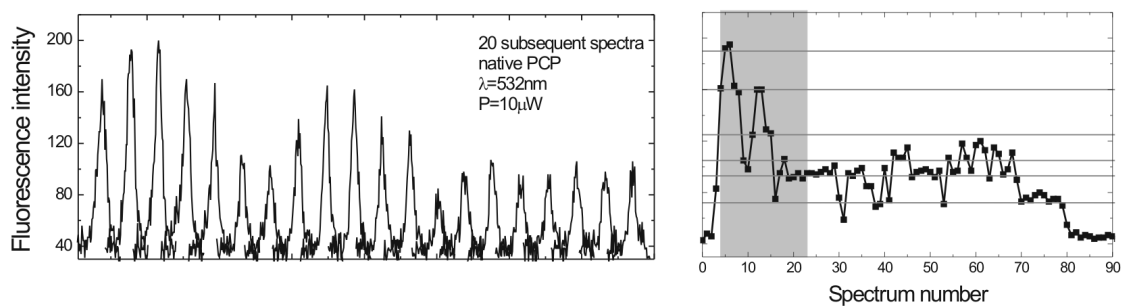


**Figure 5.11:** Fluorescence intensity trace measured for a single native PCP complex. Left: Five spectra measured for this complex at various times of the trace, as described. Right: The whole intensity trace, each spectrum corresponds to 0.3 s.

steps for individual native PCP complexes is more difficult compared to the straightforward case of monomeric PCP. Nevertheless, for most of single native PCP complexes the actual number of observed intensity steps varies between four and six. There were again no significant spectral shifts of the fluorescence emission during the measurement, which indicates that the bleaching event of one of the chromophores does not influence the spectroscopic characteristics of the remaining fluorescing pigments. This implies weak interaction between Chl within monomers as well as between monomers within a PCP trimer. However, there are also some native PCP complexes (less than 10 %), which exhibit only two-step bleaching. This behaviour is attributable to monomeric PCP, some amount of which has been suggested to coexist with the trimeric form of native PCP [7, 100]. The results of fluorescence spectroscopy obtained for single native PCP complexes reinforce further the conclusions drawn from experiments performed on the much simpler reconstituted PCP complexes.

## 5.4 Polarisation-resolved SMS

A more direct way to show that stepwise photobleaching in PCP originates from two independent chromophores is possible via recording polarisation-resolved fluorescence [126, 127]. Each chromophore in PCP is represented by electric dipoles  $\mu_{\text{Chl1}}$  and  $\mu_{\text{Chl2}}$  which feature different spatial orientation. Fluorescence emission of each Chl originates from  $Q_y$  transition dipole moment and thus is polarised along its molecular  $y$ -axis. The degree of polarisation  $p$  of each dipole is defined as

$$p = \frac{I_{\parallel} - I_{\perp}}{I_{\parallel} + I_{\perp}}, \quad (5.2)$$

where  $I_{\parallel}$  and  $I_{\perp}$  correspond to fluorescence intensities of parallel and perpendicular polarisation, respectively. The degree of polarisation stays constant unless reorientations  $\Delta\theta$  occur which, in general, are due to rotational or translational motion [10].

Polarisation-resolved SMS on N-PCP could be realised using the wide-field setup described in Chapter 4. The upper row of Figure 5.12 shows polarisation-resolved fluorescence time traces of single (Chl  $a$ )<sub>2</sub>-N-PCP complexes in a PVA matrix. The trajectories show a similar two-step behaviour, as seen in the fluorescence intensity traces. Depending on their spatial orientation both Chls contribute to  $I_{\parallel}$  and  $I_{\perp}$ . Thus, bleaching of one Chl is apparent as a drop in intensity in both polarisation channels. These changes are not due to any reorientation of one of the chromophores. Proteins of smaller or similar size as PCP are effectively immobilised in a PVA matrix as shown by [128]. Therefore, translational motion of the whole complex during the course of measurements can be ruled out. Furthermore, from fluorescence anisotropy investigations [66, 100] it can be deduced that the chromophores have no rotational degrees of freedom within the protein structure. Hence, the substantial steps visible in the polarisation traces are attributed to the presence of two independent emitters.

Upon bleaching of one of the Chl emission dipoles the degree of polarisation changes by  $\Delta p$  [129]:

$$\Delta p = 2 \cos^2(\Delta\theta) - 1, \quad (5.3)$$

where  $\Delta\theta$  here denotes the relative orientation of  $\mu_{\text{Chl1}}$  and  $\mu_{\text{Chl2}}$  with respect to the laboratory system. Polarisation traces according to Equation (5.3) are also depicted in Figure 5.12. Bleaching of the first Chl is apparent as a drop in polarisation. The traces are recorded until bleaching of the second Chl. Polarisation measurements have been used to determine the absolute three-dimensional orientation of single molecules. Unfortunately, this is not possible via the recorded polarisation traces here without further information of at least one absolute angle. This could be realised by imaging of emission patterns in wide-field imaging [130, 131].

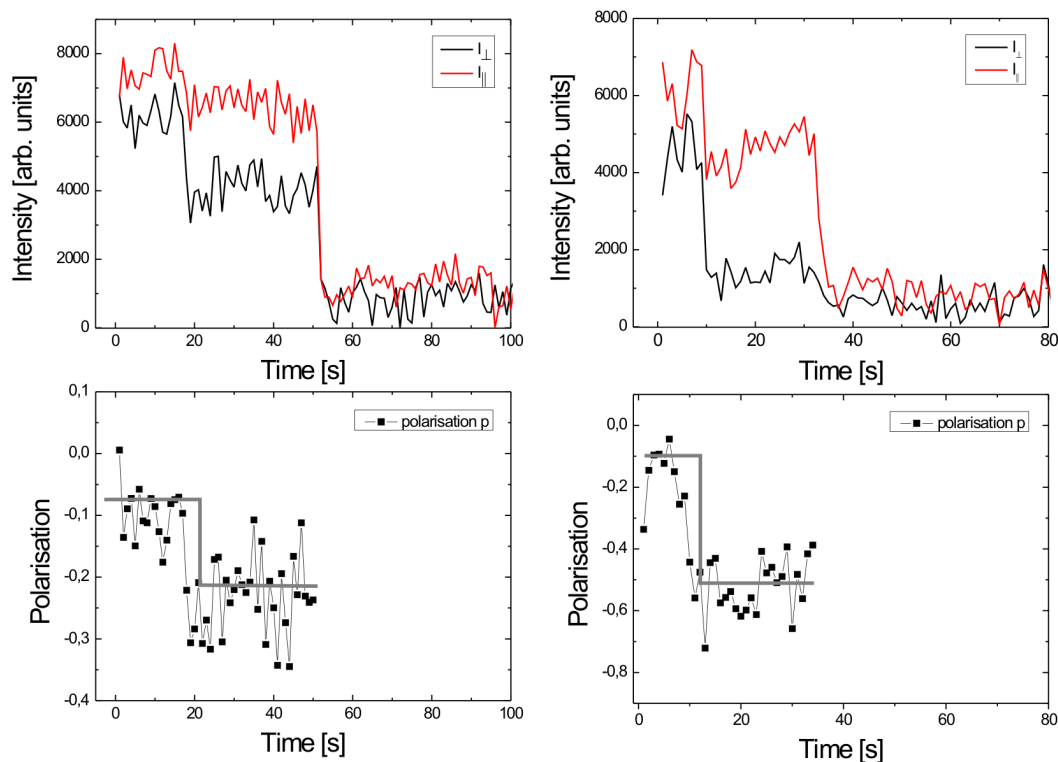


**Figure 5.12:** Changes in polarisation upon stepwise photobleaching in  $(\text{Chl } a)_2\text{-N-PCP}$ . Upper panel: Shown in red and black are emission intensities of fluorescence measured with perpendicular  $I_{\perp}$  and parallel  $I_{\parallel}$  polarisation, respectively. Bleaching of one Chl is visible as a drop in intensity in both channels due spatial orientation of its emission dipole. Intensity drops to background level after bleaching of the second Chl. Lower panel: Degree of polarisation recorded from the polarisation traces of the same two molecules. Bleaching of the first Chl is accompanied with a drop in polarisation in accordance to Equation (5.3).

## 5.5 Solvent Effects on Stability

A variety of environmental factors like solvents affect the photo-stability of fluorophores [10]. In contrast to experiments on native PCP, where Tris EDTA buffer has been used as a solvent, the homo-chlorophyllous complexes were embedded in a polymer (PVA). This approach improved the photo-stability of the complexes which might be due to formation of small cavities of polymer strands in which PCP complexes are enclosed. In this way it is possible to successfully protect the molecules from ambient oxygen that was reported to play a critical role in photobleaching of light-harvesting complexes [122]. Figure 5.13 compares the photobleaching time measured for  $(\text{Chl } a)_2\text{-N-PCP}$  complexes in PVA and Tris EDTA. An excitation wavelength of 532 nm and laser power of 10  $\mu\text{W}$  were used in both measurements. Average survival times for PCP complexes obtained by an exponential fit to the data in Figure 5.13 in Tris EDTA and PVA matrixes resulted in  $22 \pm 3$  and  $26 \pm 3$

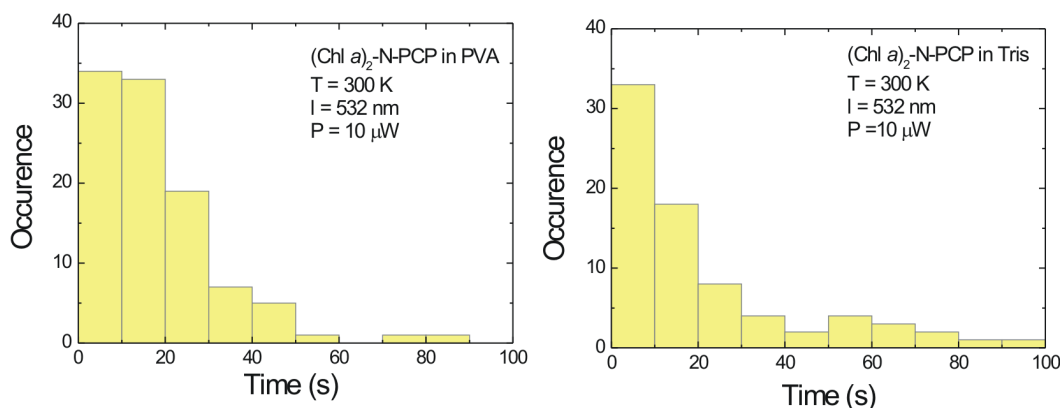


**Figure 5.13:** Comparison of survival times measured for single reconstituted (Chl a)<sub>2</sub>-N-PCP complexes in two different solvents: PVA polymer matrix(left) and Tris EDTA buffer (right).

s, respectively. Because of increased photo-stability PVA was used in most single molecule experiments.

Another solvent effect on PCP concerns the stability of monomers and trimers. Since solving the crystal structure of native PCP by Hofmann *et al.* [7], it has been speculated whether the trimeric structure was in fact the *in vivo* structure. The results of SMS demonstrate that trimeric PCP is stable even in solvents comparably unfavourable as compared to *in vivo* conditions. Such conclusions can be drawn from distributions of fluorescence intensities. The native PCP complex contains three times as many Chls as the reconstituted (Chl a)<sub>2</sub>-N-PCP. Since all these Chls are chemically identical the average fluorescence intensity measured for single native complexes should be larger than for (Chl a)<sub>2</sub>-N-PCP. Figure 5.14 displays histograms of maximum fluorescence intensities collected for over hundred single (a) (Chl a)<sub>2</sub>-N-PCP and (b) native PCP complexes in Tris EDTA buffer (pH = 7.4). All spectra were taken with 0.3 s acquisition time. In the case of (Chl a)<sub>2</sub>-N-PCP the distribution features a relatively broad distribution extending slightly towards higher intensities. In contrast, the distribution obtained for native PCP shows two clear peaks of fluorescence intensity. The lower peak coincides with the one observed for (Chl a)<sub>2</sub>-N-PCP and is due to PCP monomers. The second one appears at about 2.5x higher intensity. This maximum is attributed to the fluorescence of PCP complexes that maintain the trimeric form, i.e. contain six Chl a molecules. This result suggests that in Tris EDTA buffer both monomeric and trimeric PCP complexes seem to be stable and coexist in the mixture as supported by [7, 100]. The peak intensity of the native PCP complexes is not three times higher as compared to the signal measured for the monomers due to fixed geometry of the trimer [7] that results in unequal contributions of each of the Chl a molecules to the total fluorescence intensity measured for the complex. Analogous measurements performed for the reconstituted and native PCP complexes in PVA matrix are displayed in Figure 5.14(c) and (d), respectively. In a clear contrast to the results obtained in Tris EDTA buffer, in both cases the maximum fluorescence intensity features only a

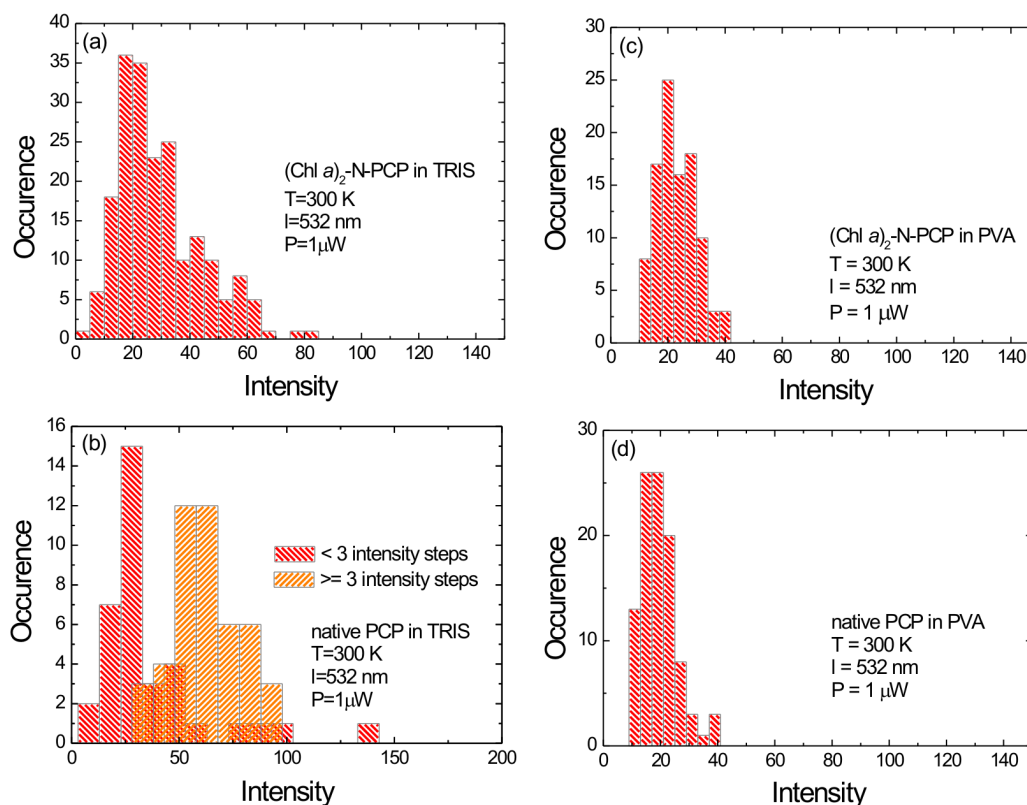


**Figure 5.14:** Histograms of fluorescence emission intensities for (a)  $(\text{Chl } a)_2\text{-N-PCP}$  and (b) native PCP in Tris buffer and (c)  $(\text{Chl } a)_2\text{-N-PCP}$  and (d) native PCP in PVA. In the case of native PCP in Tris buffer the subsets of complexes showing  $<3$  (left shading) and  $\geq 3$  (right shading) intensity steps are distinguished

single peak at the intensity corresponding to monomeric PCP. This suggests that while in Tris EDTA buffer monomers and trimers of PCP are in an equilibrium, in the polymer PVA matrix only monomers are stable.

Supporting evidence for the presence of trimeric PCP complexes in Tris EDTA buffer can be obtained from an analysis of fluorescence intensity steps measured for individual complexes [132]. Two-step photobleaching of  $(\text{Chl } a)_2\text{-N-PCP}$  is, as discussed above, a clear indicator of monomeric PCP. In contrast to reconstituted  $(\text{Chl } a)_2\text{-N-PCP}$ , the fluorescence trajectories collected for native PCP featured frequently more than two steps which can be used as a characteristic indication of stable trimeric structure. The information about the intensity steps measured for native PCP complexes allows for correlating it with the total fluorescence intensity, as displayed in Figure 5.14. The PCP complexes showing less than three intensity steps (attributed to monomers) are marked in left shading, while complexes showing three or more intensity steps (attributed to trimers) are marked with right shading. As can be seen, there is a correlation between the total intensity and the number of bleaching steps observed

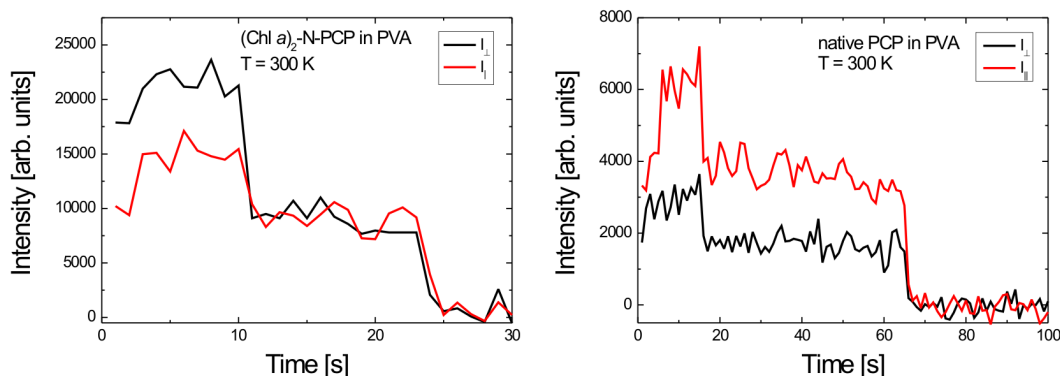


**Figure 5.15:** Polarisation-resolved fluorescence trajectories measured for (left)  $(\text{Chl } a)_2\text{-N-PCP}$  and (right) native PCP in PVA matrix. Solid and dashed lines correspond to two orthogonal polarisations.

for the native PCP complexes. Namely, the complexes featuring three or more intensity steps are grouped around the high intensity maximum seen in Figure 5.14(b), while the majority of complexes that exhibit less than three intensity steps are around the low intensity peak. The distinct separation between the two distributions indicates that both monomeric and trimeric PCP complexes are present in the sample prepared with Tris EDTA buffer. Since no trimeric PCP was present in the PVA matrix, the stability of trimers depends on the environment. Ultracentrifugation experiments carried out by Hofmann *et al.* [7] have shown that the equilibrium between monomers and trimers depends on the protein concentration: at low concentrations monomers are more stable, whereas higher concentrations favour trimers. Moreover, it has been postulated that slightly acidic surroundings are preferable for forming PCP trimers. The results obtained for PCP complexes in PVA matrix are in good agreement with these observations. The combination of a neutral environment and low protein concentration (typically a few  $\mu\text{M}$ ) changes the equilibrium such that only monomers are stable. However, in the case of Tris EDTA buffer, at slightly basic conditions ( $\text{pH} = 7.4$ ), PCP trimers can be stabilised even at low concentrations.

Additional indication of the presence of monomers in PVA can be obtained from polarisation-resolved measurements, as discussed in the previous section. Figure 5.15 shows polarisation dependent time traces of fluorescence intensities obtained for (a)  $(\text{Chl } a)_2\text{-N-PCP}$  in PVA and (b) native PCP in PVA in two orthogonal polarisations. In both cases, a two-step bleaching behaviour is observed [132], demonstrating the presence of two emitting Chl *a* molecules. For all native PCP complexes in PVA matrix the fluorescence, and thus polarisation, decays in two steps which confirms that under these conditions only monomers are stable.

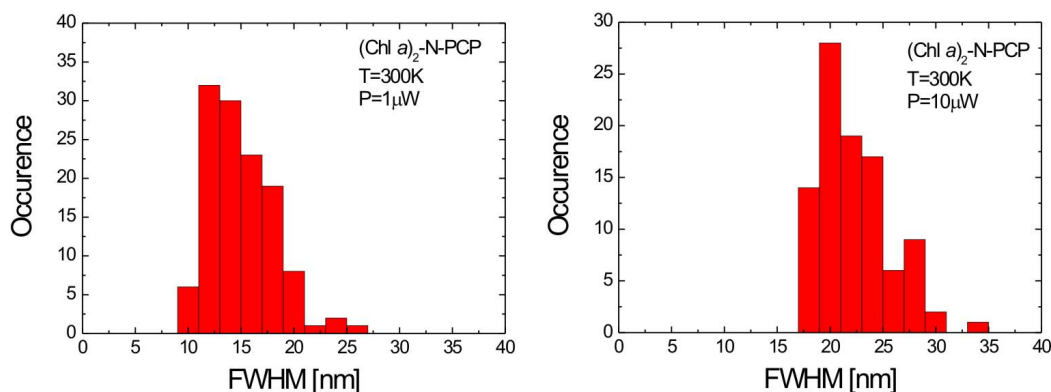


**Figure 5.16:** Distribution of fluorescence linewidths measured for single reconstituted (Chl *a*)<sub>2</sub>-N-PCP complexes with excitation powers of (a) 1 μW and (b) 10 μW.

## 5.6 Protein-Pigment Interaction

As discussed in Chapter 2, the chemical environment of a chromophore alters its optical properties [125, 133–135]. Proteins are complex systems that dynamically change their conformational states characterised by rugged potential energy landscapes with multiple barriers separating potential energy valleys [24, 136]. Transitions between protein substates are usually temperature-driven but can also be photo-induced through the thermal energy released via radiationless deactivation channels after absorption of light. Consequently, the dynamic structural changes constantly alter the optical properties of any chromophore that is embedded in the protein capsule. Thus, the chromophore itself can be considered a “natural” reporter of its local protein surrounding. The relatively simple structure of PCP, in particular the weakly interacting Chl molecules, render this system interesting for studying protein-pigment interactions by monitoring the fluorescence emission of single independent Chls. The spectral changes of fluorescence linewidth and emission energy can be attributed to photo-induced changes in protein conformational dynamics.

Previous experiments carried out on other light-harvesting systems like LH2 have shown that spectral changes should depend on the excitation power [117, 137]. Figure 5.16 shows the distribution of fluorescence linewidths measured for single (Chl *a*)<sub>2</sub>-N-PCP complexes at two different excitation powers of 1 μW and 10 μW, respectively. The experiment was done in Tris EDTA buffer with an acquisition time of 0.3 s. Although for both excitation powers the distribution has a comparable width, the average value of the linewidth is much larger at higher laser power (21 nm at 10 μW compared to 12 nm at 1 μW). Similar behaviour is observed for native PCP complexes, where the average values of the fluorescence linewidth of 23 and 14 nm have been measured at 10 μW and 1 μW (data not shown). The slightly higher linewidth in the case of native PCP complexes can be due to the presence of a larger number of Chl *a* molecules, which would result in stronger inhomogeneous broadening of the

emission.

The increase of the fluorescence linewidth with the excitation power is accompanied by a strong broadening of the distribution of fluorescence maximum energies measured for individual PCP complexes. The result is displayed in Figure 5.17 which compares fluorescence maximum energies, measured for many (Chl *a*)<sub>2</sub>-N-PCP complexes at the excitation powers of (a) 1  $\mu$ W and (b) 10  $\mu$ W. The average wavelength of about 672 nm does not change with the laser intensity. Remarkably, the histogram obtained for the laser power of 1  $\mu$ W is rather narrow (SD = 2 nm) with the width of the distribution increasing up to 4.4 nm for the molecules excited with 10  $\mu$ W. The broadening is more prominent towards lower wavelengths, similar to results obtained for the LH2 complex [137].

The increase of the fluorescence linewidth and broadening of the maximum emission energy distribution upon raising the excitation power is a signature of photo-induced spectral dynamics of the protein. The conformational motions of the protein in PCP that can alter the spectral properties of Chls *a* have recently been considered theoretically [138] using molecular dynamics simulations. Structural changes of the protein may induce significant fluctuations of the absorption of the Chl molecules. In the fluorescence experiment, continuous irradiation by the laser drives the molecules into conformational substates that are not accessible under ambient conditions or at low-intensity laser exposure. Higher excitation powers could induce larger and more frequent structural motions. The broadening of the fluorescence emission points towards dynamics that occurs on a time scale much shorter than the acquisition time used in the experiment (typically 0.3 s).

The increase of energy distribution for high excitation power is an indication for structural changes that take place on a time scale comparable with the acquisition time and hence can be monitored by collecting sequences of fluorescence spectra [139]. Two typical traces are plotted in Figure 5.18 in the form of two-dimensional graphs showing a series of consecutive

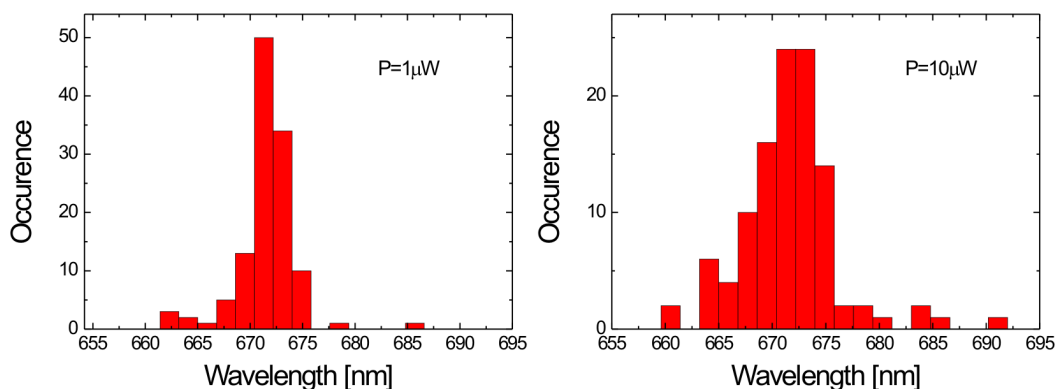


**Figure 5.17:** Fluorescence energy distributions measured for single (Chl *a*)<sub>2</sub>-N-PCP with excitation powers of 1  $\mu$ W (left) and 10  $\mu$ W (right).

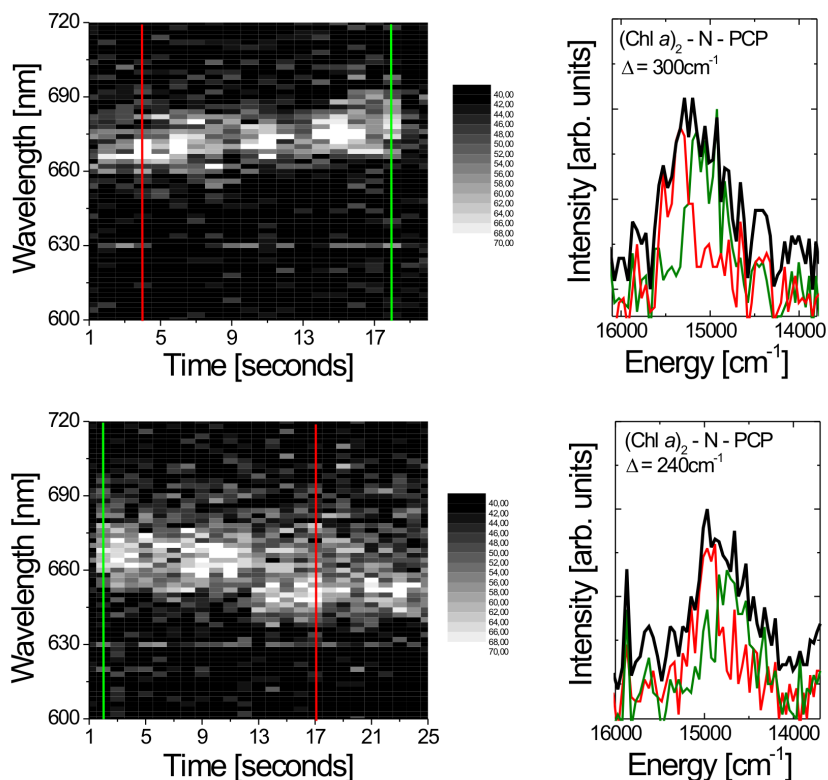


**Figure 5.18:** Sequences of fluorescence spectra observed for two single Chl *a*-N-PCP complexes measured after photobleaching of one of the Chls. The gray-scale two-dimensional images (left column) show a series of consecutive spectra measured as a function of time with the integration time of 0.3 s. Increasing white corresponds to increasing intensities of the fluorescence. The spectra extracted along the vertical lines shown on the images are displayed in corresponding colors on the graphs in the right column. The black lines are the spectra obtained after summing up all spectra in the respective sequence.

spectra. The x axis corresponds to time, while the y axis shows the emission wavelength. In both cases the fluorescence of a single Chl *a* molecule is measured and the time trace starts just after bleaching of the first Chl. The trace shown in the upper row features a clear spectral jump after about 12 s. The molecule displayed in the lower row shows diffusion-like behaviour, which is most probably a combination of jumps that - due to relatively long acquisition time of the experiment - could not be resolved. The two-dimensional maps are accompanied by the fluorescence spectra (right column) extracted at the time points marked with solid lines. In both cases the position of the fluorescence is changed over an energy range of 240 and 300  $\text{cm}^{-1}$ , respectively, which is larger than the linewidth of a single Chl *a* emission ( $\sim 200 \text{ cm}^{-1}$ ). In addition, the calculated sum of the fluorescence spectra measured for these complexes is displayed as black solid lines. The linewidths of the emission are comparable to the spectral changes. Obviously, the broadening of the linewidth of the summed-up spectrum is due to observed spectral dynamics. This result demonstrates that using energy transfer from Per to Chl in PCP for single molecule detection, large spectral changes can be monitored. This

overcomes a difficulty often faced in SMS. Through direct excitation and detection frequently only a very narrow energy range of spectral changes is accessible [117]. Thus, only spectral changes occurring on a scale much smaller than the inhomogeneous broadening could be monitored.

## 5.7 Conclusion

In conclusion, fluorescence spectroscopy, both at the ensemble and single molecule level, was carried out on native and reconstituted PCP. All experiments utilised the efficient energy transfer from Per as an excitation channel of Chl emission. Absorption and circular dichroism spectra recorded for PCP ensembles reveal spectral features characteristic to the reconstitution with Chl *a*, Chl *b* and acChl *a*. A comparison with analogous data collected for pure Chl pigments in acetone indicate spectral shifts due to influence of the protein environment. In the fluorescence emission spectra characteristic spectral features of Chls are apparent as well. Namely, narrow emission lines that are attributed to  $Q_y$  emission of the different Chl pigments used for reconstitution. Both absorption and emission spectra, as well as measured fluorescence quantum yields and lifetimes, provide the basis for a detailed analysis of energy transfer between Chls in the hetero-chlorophyllous complexes discussed in the next chapter. Fluorescence excitation spectra collected on all homo-chlorophyllous N-PCP prove that highly efficient energy transfer from native PCP is preserved in the reconstitutions.

Single molecule spectra excited using energy transfer from Per show step-wise photo-bleaching of fluorescence emission. The steps apparent for native as well as reconstituted PCP leave no measurable influence on the spectral properties of the remaining Chls. These results indicate weak dipole-dipole coupling between the Chls embedded in a PCP complex. This conclusion is further supported by polarisation-resolved SMS. As a consequence, the Chls in PCP can be independently monitored using a single laser excitation source. Due to slightly different environments in the protein capsule the Chls are energetically distinguishable with spectral splitting of up to  $280\text{ cm}^{-1}$ . Comparison of SMS results indicate that PCP features longer bleaching time in a PVA polymer matrix as compared to Tris EDTA buffer. However, in PVA the equilibrium between monomeric and trimeric native PCP is shifted such that only monomers are stable. The fluorescence emission of single PCP complexes exhibits signatures of photoinduced conformational dynamics of the protein. Strong increase of the average linewidth of the emission upon increasing excitation power is attributed to structural changes that occur on a timescale much shorter than the subsecond acquisition time. On the other hand, the broadening of the fluorescence maximum frequency distribution is due to structural changes taking place on a timescale comparable to the acquisition time.

In summary, the results of SMS and ensemble spectroscopy provide detailed information needed to understand energy transfer in hetero-chlorophyllous PCP as a function of structure. This is presented in the following chapter.

# CHAPTER 6

---

## Spectroscopy of Hetero-Chlorophyllous N-PCP

---

In this Chapter the results of spectroscopy on N-PCP complexes reconstituted from mixtures of Chls are presented. Hetero-chlorophyllous complexes are interesting model systems to study pigment-pigment interactions and energy transfer as a function of structure. That such complexes indeed form by reconstitution is apparent from ensemble spectroscopy presented in Section 6.1. The data indicates energy transfer between the Chls at the  $Q_y$  level and is described in terms of Försters theory in Section 6.2. However, due to the structural heterogeneity of the hetero-chlorophyllous samples also homo-chlorophyllous complexes are present. The results of single molecule spectroscopy summarised in Section 6.3 not only provide direct means to distinguish hetero-chlorophyllous N-PCP from homo-chlorophyllous ones, but also allow for detailed analysis of spectroscopic properties associated with the individual complexes. The SMS spectra show fluorescence intensity peaks attributable to two different Chls embedded in a single complex. Step-wise photo-bleaching is observed in these samples as well and, similar to homo-chlorophyllous N-PCP discussed in Chapter 5, the Chls can be independently monitored. The relative fluorescence intensities are due to Chl-Chl and Per-Chl energy transfer and are modeled by Monte-Carlo simulations in Section 6.4.

### 6.1 Ensemble Spectroscopy

Ensemble spectroscopy is used to characterise N-PCP reconstituted with binary mixtures of Chl *a*, Chl *b* and acChl *a*. However, due to the structural heterogeneity absorption and fluorescence emission spectra alone cannot provide evidence that hetero-chlorophyllous complexes indeed formed during the reconstitution process. Fluorescence excitation spectra reveal energy transfer pathways in these samples and show the presence of two different Chl pigments in the complexes.

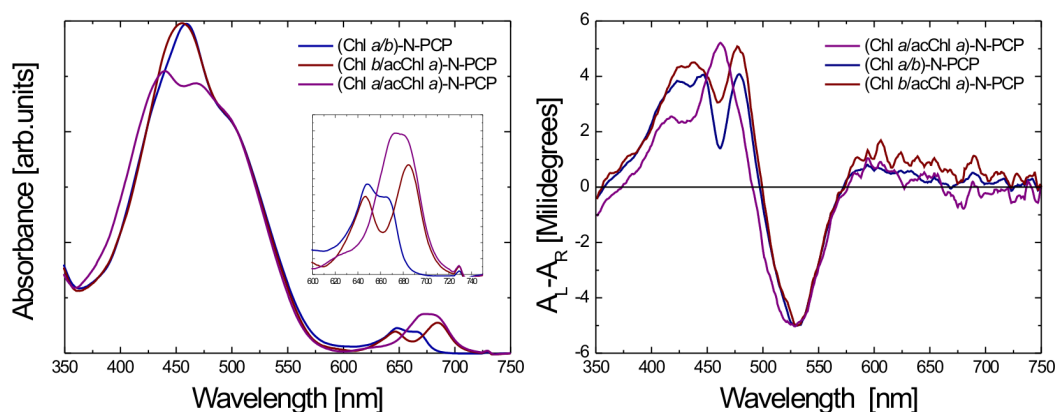


**Figure 6.1:** Left: Absorption spectra of hetero-chlorophyllous N-PCP reconstituted with Chl *a* and acChl *a* (in purple), Chl *a* and Chl *b* (in blue), and Chl *b* and acChl *a* (in red). Spectra were normalised into Per related absorption at 505 nm. Right: CD spectra of the same set of hetero-chlorophyllous N-PCP complexes. Spectra were normalised at the negative extremum of Per at 532 nm.

### 6.1.1 Absorption and Circular Dichroism

Figure 6.1 shows absorption and CD spectra of N-PCP reconstituted from binary mixtures of Chl *a*, Chl *b* and acChl *a*. All spectra clearly show contributions of the respective pigments. Absorption of the (Chl *a/b*)-N-PCP complex features a pronounced Soret band due to the presence of Chl *b* and a split  $Q_y$ -band at 647 and 668 nm (see inset of Figure 6.1). The CD spectrum is dominated by two superimposed S-shaped bands. The major component shows extrema at 480 (+) and 532 (-) nm. The minor S-shaped band is superimposed on the intense positive extremum and has been attributed to Per. It is an indication of excitonic coupling between Chl *a* and Per in the same half of the N-PCP dimer [100]. Soret band is pronounced in all samples containing Chl *b* and red-shifted as compared to the sample without Chl *b*. (Chl *b/acChl a*)-N-PCP shows large spectral overlap with both absorption and CD of (Chl *a/b*)-N-PCP but  $Q_y$ -bands are clearly separated. Absorption and CD spectra of (Chl *a/acChl a*)-N-PCP are similar and show effects of the presence of acChl *a*. The  $Q_y$ -band is red-shifted compared to Chl *a* as in solution of pure pigments (see Figure 3.3). Clearly, Soret band is less pronounced as compared to the other samples.

The spectra of hetero-chlorophyllous complexes are only superficially a mixture of the ones of the homo-chlorophyllous complexes. However, a closer inspection reveals differences, that are likely due to Chl-Chl interactions. Figure 6.2 shows absorption spectra of (Chl *a/b*)-N-PCP and compares it with the respective homo-chlorophyllous spectra. In this example

- the Chl *b*-related  $Q_y$ -CD band at 649 nm is stronger than that of Chl *a* at 669 nm. Based on the spectra of homo-chlorophyllous complexes in Figure 5.1 (and [94]), and the Chl

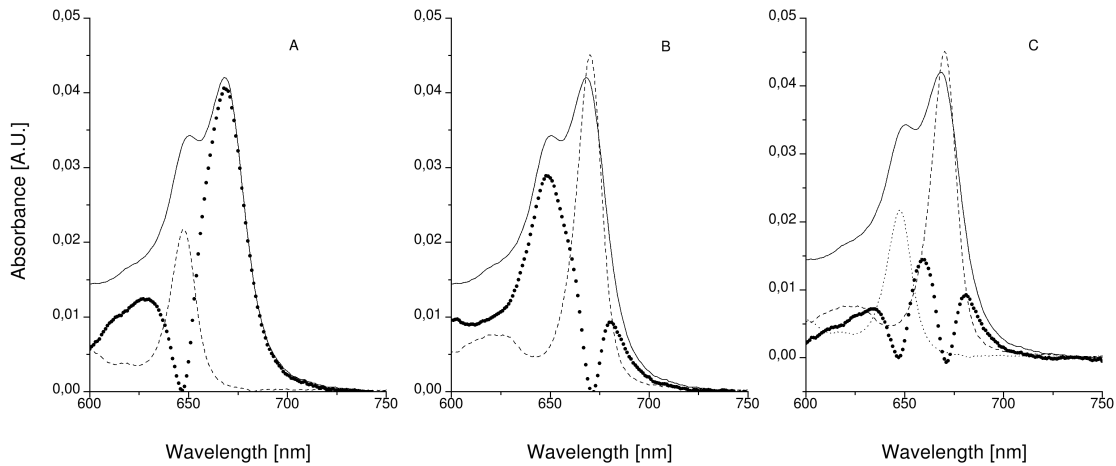


**Figure 6.2:** Comparison of homo- and hetero-chlorophyllous N-PCP complexes. Absorption spectra of Chl *a/b*-N-PCP (bold lines) and absorption differences (primed lines) with (A) the spectra of (Chl *a*)<sub>2</sub>-N-PCP, (B) (Chl *b*)<sub>2</sub>-N-PCP and (C) the sum of Chl *a*-N-PCP and Chl *b*-N-PCP. The subtracted homo-chlorophyllous spectra are shown as dotted lines, they were scaled to give minimum deviation in the region of the respective Chls.

*a/b*-ratio as determined from the reconstitution product [95]), at most equal intensities are expected

- the red absorption and CD-bands of Chl *a* are blue-shifted by 2 nm in the Chl *a/b* complex as compared to the Chl *a* - only sample (see Figure 6.2)
- subtraction of the absorption spectra of the homo-chlorophyllous (Chl *a*)<sub>2</sub>-N-PCP or (Chl *b*)<sub>2</sub>-N-PCP complex from that of the hetero-chlorophyllous complex always gave additional bands (Figure 6.2).

However, the situation could be further complicated by the possibility that there are complexes, in which one binding site is empty, and by the presence of half-mers carrying only a single Chl-Per cluster. However, these are unlikely based on the tight pigment binding and dimerisation of individual N-PCP and were not considered here. Fluorescence spectroscopy of bulk samples gives likewise inconclusive results. Thus, the spectral shifts are a first indication of Chl-Chl interaction and suggest formation of hetero-chlorophyllous complexes.

### 6.1.2 Fluorescence Emission Spectra

Figure 6.3 shows ensemble fluorescence spectra measured for N-PCP samples reconstituted with (a) Chl *a* and acChl *a*, (b) Chl *a* and Chl *b*, and (c) Chl *b* and acChl *a*. The excitation wavelength was 532 nm throughout. All three preparations were reconstituted with binary mixtures of the respective Chls. These ratios are somewhat changed in the reconstituted complexes, due to different affinities [96]. All three samples show two emission lines that are, by their positions, clearly attributable to the emissions of the respective Chl molecules used for reconstitution. The emission of the various Chl pigments is slightly shifted as compared

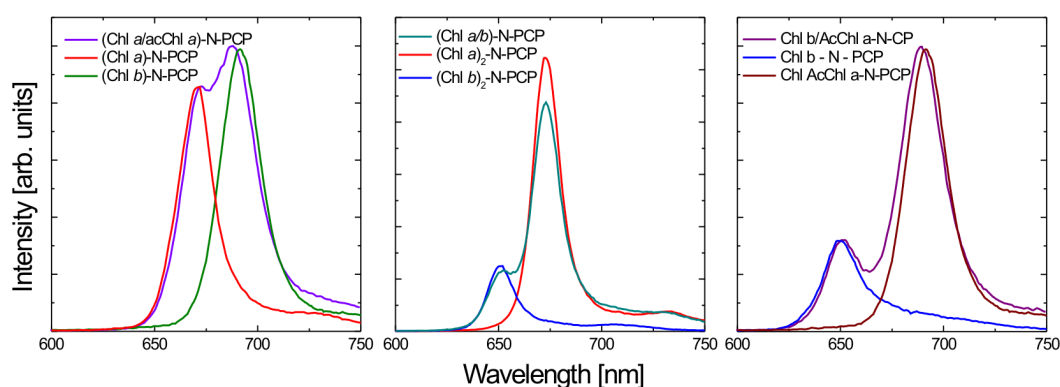


**Figure 6.3:** Normalised room temperature fluorescence spectra of N-PCP reconstituted with Chl mixtures. (a) Chl *a* and Chl *b*, (b) Chl *b* and acChl *a*, and (c) Chl *a* and acChl *a*. The fluorescence emission was excited at 532 nm. The excitation wavelength was 532 nm. For comparison emission of Chl *b*, Chl *a*, and acChl *a* are plotted as well.

with the respective homo-chlorophyllous complexes. For example Chl *a* emission occurs at 671 nm in the Chl *a*/Chl *b* complex which is red-shifted by 2 nm compared to the Chl *a* - only complex. These minor but reproducible shifts are also seen in the Soret-region. All these shifts point to small, but distinct Chl–Chl interactions between the Chls in the two clusters as already apparent in the absorption and CD spectra.

### 6.1.3 Fluorescence Excitation Spectra

Absorption and fluorescence emission spectra alone cannot provide evidence that hetero-chlorophyllous N-PCP indeed is formed by reconstitution. This process, though influenced by the relative binding affinities of the pigments, is random, and it is therefore expected that the preparations are always mixtures of homo- and hetero-chlorophyllous complexes. Figure 6.5 shows fluorescence excitation spectra measured for N-PCP reconstituted with (a) Chl *a* and Chl *b*, (b) Chl *b* and acChl *a*, and (c) Chl *a* and acChl *a*. Detection was centred into the respective Chl emission maxima, i.e. 650, 670 and 690 nm for Chl *b*, Chl *a* and acChl *a*, respectively. By monitoring the fluorescence of the long-wavelength Chl, i.e. Chl *a* in N-PCP reconstituted with Chl *a* and Chl *b*, and acChl *a* for the two other reconstitutions, an emission band is observed at the excitation wavelengths corresponding to the shorter-wavelength Chl, i.e. Chl *a* in N-PCP reconstituted with Chl *a* and acChl *a*, and Chl *b* for the two other reconstitutions. Its presence implies that there are complexes containing two different Chl molecules in a single monomer, and that there is energy transfer between the  $Q_y$ -bands of these Chls [87, 95, 140]. This energy transfer is best visible in the case of N-PCP reconstituted with Chl *b* and acChl *a*, where the energy difference between the Chl absorption bands is the largest ( $\sim 40$  nm). Interestingly energy transfer occurs in both energy directions. The uphill transfer between the Chls can be studied by exciting into the respective long-wavelength Chl, and monitoring the emission

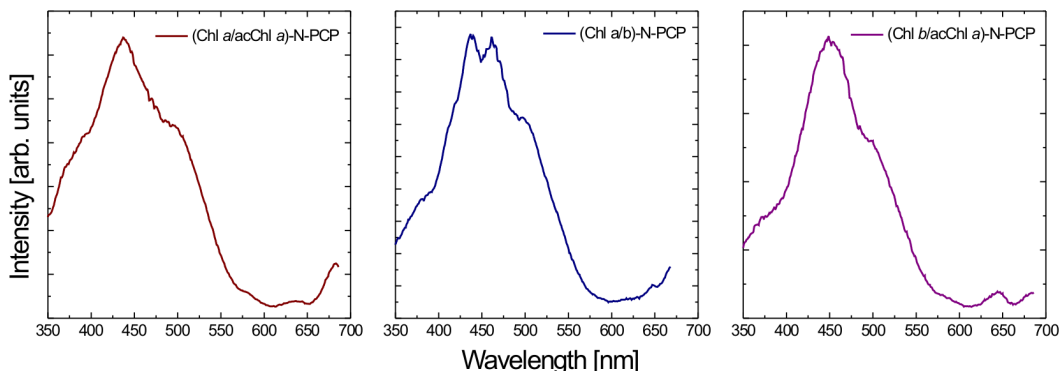


**Figure 6.4:** Ensemble fluorescence excitation spectra of N-PCP reconstituted with Chl mixtures: Chl *a* and acChl *a* (in purple), Chl *a* and Chl *b* (in blue), and Chl *b* and acChl *a* (in red). Detection was centred at 650, 670 and 690 nm, corresponding to emission maximum of Chl *b*, Chl *a*, and acChl *a*, respectively.

of the short-wavelength one. In the N-PCP sample reconstituted with Chl *b* and acChl *a*, the transfer is mostly unidirectional in the energetically favorable direction, viz. from Chl *b* to acChl *a*. By contrast, as seen in Figure 6.5, the fluorescence excitation spectrum of N-PCP reconstituted with Chl *a* and Chl *b* detected at the Chl *b* emission, has a strong peak at the absorption energy of Chl *a* [140]. Considerable energy transfer in this complex takes place also in the less-energetically favourable direction: from Chl *a* to Chl *b*.

Besides direct coupling between the Q<sub>y</sub>-bands of the Chl in reconstituted N-PCP there is also strong interaction between the two half-mers in the energy range corresponding to Pers and

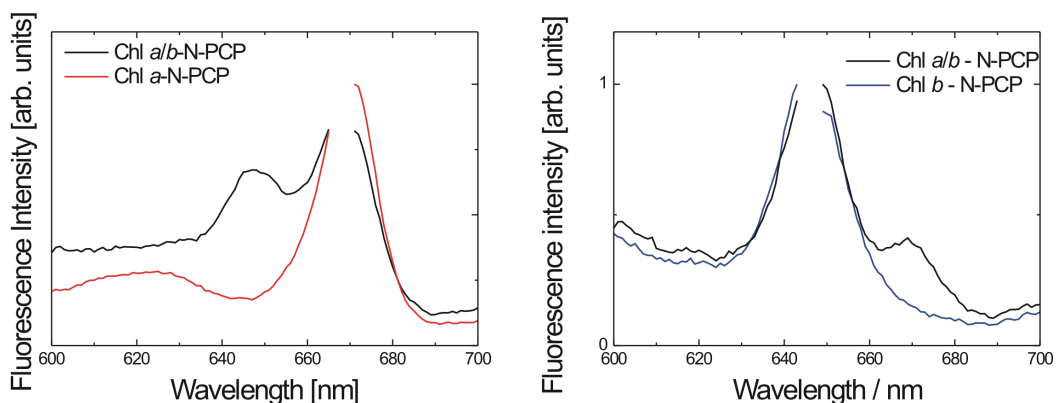


**Figure 6.5:** Room temperature fluorescence excitation spectra in the Q<sub>y</sub> region of N-PCP reconstituted with both Chl *a* and Chl *b* (black line). Left: detection at 668 nm ((Chl *a*)<sub>2</sub>-N-PCP in red) line Right: detection at 647 nm ((Chl *b*)<sub>2</sub>-N-PCP in blue).

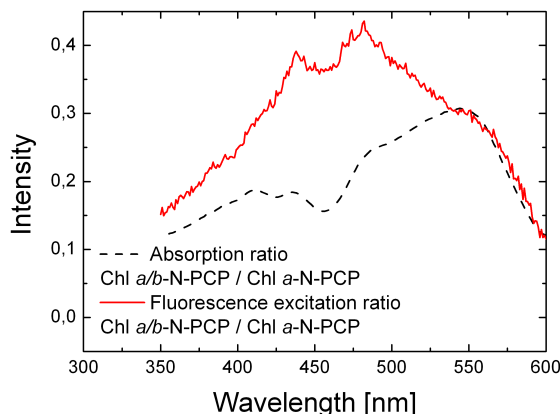


**Figure 6.6:** Comparison of absorption (dashed line) and fluorescence excitation (solid line) spectra of the N-PCP reconstituted with both Chl *a* and Chl *b* divided by respective spectra measured for (Chl *a*)<sub>2</sub>-N-PCP

Soret band of the Chls. The spectral indications of this coupling are clear resonances in the fluorescence excitation spectra detected on the longer-wavelength emitting Chls (Figure 6.4) that can be attributed to the shorter-wavelength Chls in all three samples. Particularly, the Soret band of Chl *b* at 460 nm [103] is clearly seen in the fluorescence excitation spectra detected at the Chl *a* (670 nm) and acChl *a* emissions (690 nm) for N-PCP reconstituted with Chl *b* and Chl *a* and Chl *b* and acChl *a*, respectively. Although in the case of homo-chlorophyllous complexes the excitation and absorption spectra are almost identical [103], the excitation spectrum of the N-PCP reconstituted with both Chl *a* and Chl *b* measured at the Chl *a* emission differs substantially from the absorption spectrum [95]. To display the difference Figure 6.6 compares the ratio of the absorption spectra measured for (Chl *a*)<sub>2</sub>-N-PCP and the N-PCP reconstituted with both Chl *a* and Chl *b* with the ratio of excitation spectra measured for these two systems detected at 670 nm. As can be seen, above 530 nm the curves are similar, whereas they deviate considerably at shorter wavelengths. This indicates that there is an equally good energy transfer from Per to both Chls only at  $\lambda > 530$  nm, whereas this is not true at higher excitation energies. The largest difference appears at around 455 nm, which corresponds to the Soret band of Chl *b*. This observation confirms the findings of molecular dynamics simulation [101], where the coupling between the pigments of native PCP has been calculated (see Chapter 3.5).

The strong excitonic interaction (on the order of  $100 \text{ cm}^{-1}$ ) occurs only for Per with excited state energies larger than  $18700 \text{ cm}^{-1}$  (535 nm). This spectral region is characterised also by very strong interactions between Per and the Soret bands of Chl *a*. The coupling is significantly weaker ( $\sim 10 \text{ cm}^{-1}$ ) for the two Per molecules in each cluster with excited state energies below  $18700 \text{ cm}^{-1}$ . One may therefore expect that at lower excitation energies, the two clusters are, within a good approximation, independent of each other. This conclusion is in good agreement with step-wise photo-bleaching discussed in Chapter 5.3. All single-molecule experiments presented in the following were carried out using excitation wavelength of 532 nm, i.e. the PCP complexes were excited below the threshold value. Therefore, each of the two Chls within

the monomer is excited predominantly through Per molecules that are in the same cluster, and the coupling between the clusters can be neglected (see Chapter 3.5).

## 6.2 Energy Transfer between Chlorophylls

Energy transfer between the different Chls can be described within the framework of Förster's theory [8] as presented in Chapter 2.2. Thus, the rate of the energy transfer between the donor and acceptor reads

$$\gamma_T(r) = \frac{9000(\ln 10)\kappa^2 q_d}{128\pi^5 N_A n^4 \tau_d R^6} \int_0^\infty F_d(\lambda) \varepsilon(\lambda) \lambda^4 d\lambda, \quad (6.1)$$

where  $\kappa$  is the orientation factor,  $q_d$  and  $\tau_d$  are the fluorescence quantum yield and the fluorescence lifetime of the donor,  $n$  is the refractive index of the solvent, and  $R$  is the distance between the donor and acceptor. The Förster energy transfer rates were calculated using fluorescence spectra (in the wavelength scale) of all homo-chlorophyllous reconstitutions normalised to unity area, and the absorption spectra of these complexes normalised to their respective extinction coefficients. In order to minimise potential influence of the different environments [141] absorption and emission spectra, as well as fluorescence lifetimes and quantum yields were measured experimentally for Chls embedded within the protein environment, instead of data obtained for pure Chl in organic solvents. Fluorescence lifetimes and quantum yields were measured as described in Section 5.1 and summarised in Table 5.1. The binding of all pigments other than Chl *a* to N-PCP apoprotein is assumed to be identical to that of Chl *a*. This implies an orientation factor  $\kappa = -0.394$  as reported for native PCP [66]. The rates calculated based on these assumptions are summarised in Table 6.1.

Förster energy transfer rates calculated for the Chl *b*-acChl *a* transfer is  $\gamma_T = (29 \text{ ps})^{-1}$  and the rate for the uphill transfer (acChl *a*-Chl *b*) is almost two times longer:  $\gamma_T = (63 \text{ ps})^{-1}$ . This largely inhibits the uphill energy transfer from acChl *a* to Chl *b*. A qualitatively similar behaviour is found for N-PCP reconstituted with Chl *a* and acChl *a*. In contrast, the analogous calculation performed for the Chl *a*-Chl *b* system yields a rate for the downhill transfer (Chl *b*-Chl *a*) of  $\gamma_T = (31 \text{ ps})^{-1}$ , while that for the uphill transfer (Chl *a*-Chl *b*) is  $\gamma_T = (47 \text{ ps})^{-1}$ . These values are relatively close, due to the comparably short fluorescence

Transfer rate to	Chl <i>b</i> [ $\text{ps}^{-1}$ ]	Chl <i>a</i> [ $\text{ps}^{-1}$ ]	acChl <i>a</i> [ $\text{ps}^{-1}$ ]
(Chl <i>a</i> /acChl <i>a</i> )-N-PCP	-	27	38
(Chl <i>a</i> / <i>b</i> -N-PCP	47	31	-
(Chl <i>b</i> /acChl <i>a</i> )-N-PCP	63	-	29

**Table 6.1:** Energy transfer rates calculated from ensemble spectra of hetero-chlorophyllous N-PCP

lifetime and smaller quantum yield of Chl *b* that compensate for the difference in spectral overlaps.

### 6.3 Single-Molecule Spectroscopy

The structural heterogeneity of the hetero-chlorophyllous samples makes it difficult to interpret ensemble spectroscopic data of such preparations. However, SMS allows to directly distinguish homo-chlorophyllous complexes from the hetero-chlorophyllous ones based on their individual spectra. Examples of such single molecule spectra of all hetero-chlorophyllous samples are shown in Figure 6.7. In contrast to homo-chlorophyllous N-PCP all hetero-chlorophyllous complexes feature spectra with two separated narrow emission lines. These lines are found close to the emission maxima obtained from ensemble spectroscopy and are therefore attributed to each respective Chl used in the preparation. For example Figure 6.8 compares the energy distributions of Chl emissions measured for (Chl *a*)<sub>2</sub>-N-PCP and (Chl *b*)<sub>2</sub>-N-PCP complexes with the respective lines in Chl *a/b*-N-PCP. Although individual complexes show some displacement the distributions of over 100 individual spectra resemble the ensemble fluorescence maxima (see Figure 6.3).

The simultaneous observation of two emission lines is a direct consequence of the excitation approach where the Chls are excited via sub-picosecond energy transfer from Per molecules. This strategy reduces the impact of Förster energy transfer between the Chl, which, as discussed above, is on the order of tens of picoseconds. Obviously for a system, where the energy transfer between Chls molecules were a dominant process, one would expect fast thermalisation from high-energy Chl to low-energy Chl. In such a case the fluorescence emission would originate almost exclusively from one Chl and demonstration of the presence of two different Chls

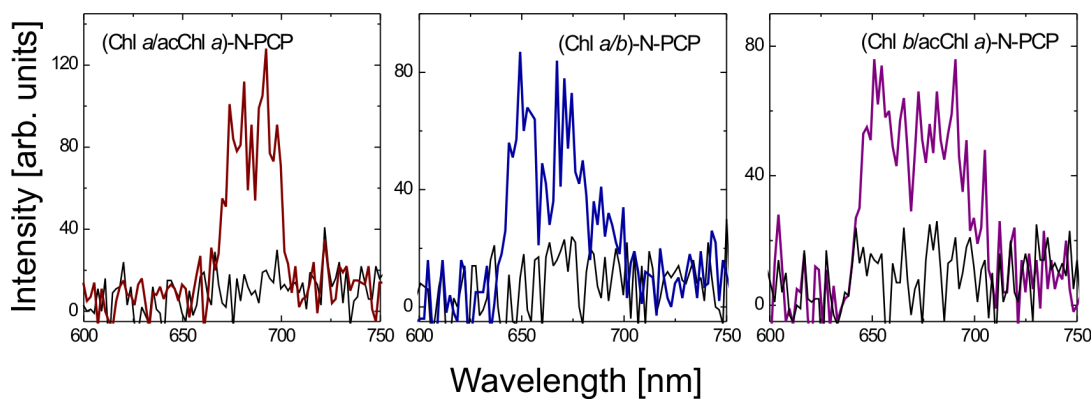


**Figure 6.7:** Single-molecule spectra measured at room temperature for (Chl *a*/acChl *a*)-N-PCP (in red), (Chl *a/b*)-N-PCP (in blue), and (Chl *b*/acChl *a*)-N-PCP (in purple). The emission of both Chl molecules in the respective complex is shown by solid lines, and black lines correspond to the background. The excitation power was 5  $\mu$ W.

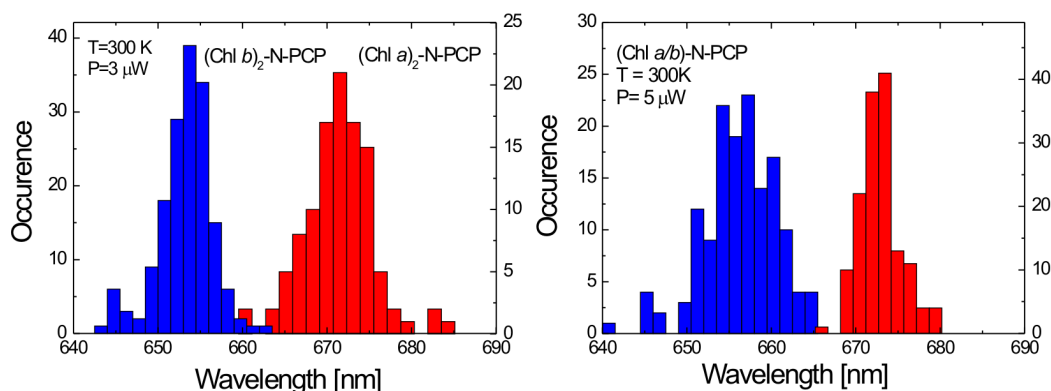


**Figure 6.8:** Distributions of emission wavelength measured for over 120 complexes of (a) homo-chlorophyllous  $(\text{Chl } a)_2\text{-N-PCP}$  (in red) and  $(\text{Chl } b)_2\text{-N-PCP}$  (in blue) samples, and (b) hetero-chlorophyllous  $\text{Chl } a/b\text{-N-PCP}$  sample for complexes showing both  $\text{Chl } a$  and  $\text{Chl } b$  emissions. The values were extracted using subsequent fluorescence bleaching of the two energetically distinguishable  $\text{Chl}$  molecules. The excitation power was  $3\ \mu\text{W}$  and  $5\ \mu\text{W}$  for homo- and hetero-chlorophyllous samples, respectively.

within the PCP monomer would require a more sophisticated analysis. In conclusion, the results demonstrate that in the hetero-chlorophyllous N-PCP complexes, one can independently monitor the fluorescence of the two different Chls within the monomer, analogous to the homo-chlorophyllous complexes.

In the hetero-chlorophyllous complexes, sequential bleaching of the two Chls in the complex is observed as well and indicates weak dipole-dipole interaction. Thus, both Chls in a complex are approximately independent and emission intensities of both emission lines can be attributed to each  $\text{Chl}$ . The correspondence of  $\text{Chl}$  emission in hetero-chlorophyllous complexes provides a basis for further analysing the fluorescence properties of reconstituted PCP complexes. As a consequence, the intensities of the Chls can be analysed separately. The left panel of Figure 6.9 shows the distributions of fluorescence intensities of each  $\text{Chl}$  pigment in  $(\text{Chl } a/\text{acChl } a)\text{-N-PCP}$ ,  $(\text{Chl } a/b)\text{-N-PCP}$ , and  $(\text{Chl } b/\text{acChl } a)\text{-N-PCP}$ . The intensities were obtained by fitting two Gaussians to single-molecule spectra of the respective complexes. The relative contribution of the different Chls to the overall fluorescence emission is obtained by dividing the distributions of individual Chls from one class of complex. The results are shown in the right panel of Figure 6.9. In general, the results of this analysis resemble the intensities apparent in the single-molecule spectra.

For most  $(\text{Chl } a/b)\text{-N-PCP}$  complexes the ratio falls in the range between 1.4 and 2.7, with the average value equal to  $1.9 \pm 0.2$ . This value is larger than the ratio of  $1.6 \pm 0.4$  between average intensities measured for single  $(\text{Chl } a)_2\text{-N-PCP}$  and  $(\text{Chl } b)_2\text{-N-PCP}$  complexes that implies the redistribution of the excitation between  $\text{Chl } a$  and  $\text{Chl } b$  due to the energy transfer. However, as the results displayed in Figure 6.9 were obtained for complexes containing both  $\text{Chl } a$  and  $\text{Chl } b$  they are more accurate. As can be seen, the  $\text{Chl } a/\text{Chl } b$  intensity ratio

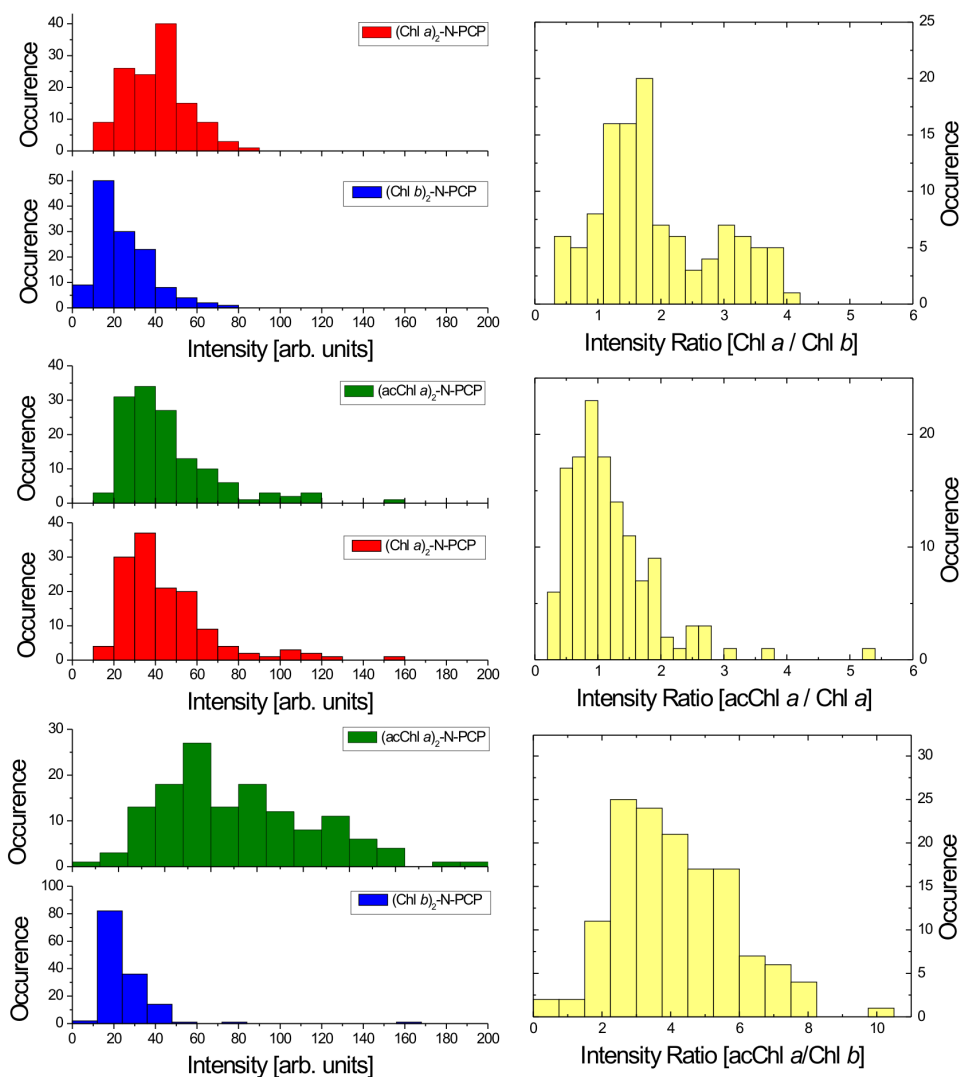


**Figure 6.9:** Left: Distributions of fluorescence intensity measured for Chl *a*, Chl *b*, and acChl *a* (Chl *a*/acChl *a*)-N-PCP, (Chl *a*/*b*)-N-PCP, and (Chl *b*/acChl *a*)-N-PCP. Right: Distribution of the fluorescence intensity ratios obtained for the same complexes. The excitation power was  $\approx 5 \mu\text{W}$ .

measured for Chl *a*/*b*-N-PCP complexes features quite a broad distribution. However, there is no obvious correlation of intensity ratio with the energy splitting between the emission lines attributed to Chl *a* and Chl *b* in a given complex. This suggests that the fluorescence intensity of the two Chls within the complex not only depends on the energy separation between Chl *a* and Chl *b* emissions but must also be a more complicated function of the fluorescence lifetime, quantum yield, and/or relative orientation of the Chl molecules in the complex.

Single (Chl *a*/acChl *a*)-N-PCP feature almost identical fluorescence intensities from each

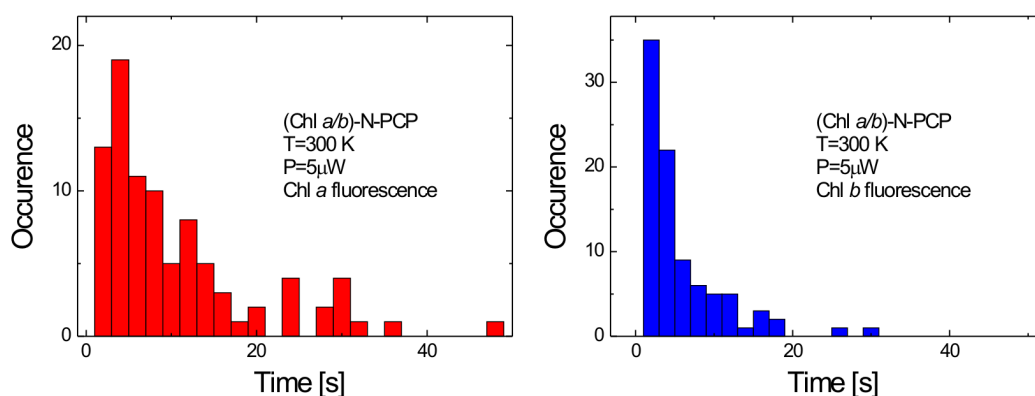


**Figure 6.10:** Survival times measured for single Chl *a/b*-N-PCP complexes. (a) Chl *a* fluorescence, and (b) Chl *b* fluorescence.

Chl. This is resembled in the average intensity ratio for (Chl *a*/acChl *a*)-N-PCP equal to  $1.2 \pm 0.2$ . Contribution of Chl *b* to spectra of (Chl *b*/acChl *a*)-N-PCP is weak and frequently close to background level. These circumstances make it difficult to achieve good spectral fits and explain the broader distribution apparent in Figure 6.9. However, the average intensity ration of  $4.1 \pm 0.6$  was obtained which is in good agreement with the experimental data.

An important photo-physical parameter accessible by SMS is the average number of photons emitted by Chl *a* and Chl *b* pigments in homo- and hetero-chlorophyllous PCP complexes. To estimate these numbers for homo-chlorophyllous PCP complexes, distributions of survival times together with average fluorescence intensities measured for these complexes are used. Generally, the fluorescence of Chl *b* can be observed over much shorter times than that of Chl *a*: average survival times measured for (Chl *a*)<sub>2</sub>-N-PCP and (Chl *b*)<sub>2</sub>-N-PCP are equal to  $7.4 \pm 0.7$  and  $3 \pm 0.5$  s, respectively. A qualitatively similar behaviour is seen for the hetero-chlorophyllous Chl *a/b*-N-PCP sample (see Figure 6.10), with average survival times estimated to be  $11 \pm 0.9$  and  $5.4 \pm 0.5$  s for Chl *a* and Chl *b*, respectively. These experiments have been performed in Tris EDTA buffer and thus feature shorter survival times as discussed in Chapter 5.5. Since the experiments were performed at slightly different excitation powers, the average survival times are multiplied by average intensities of Chl *a* and Chl *b* emissions measured for respective reconstituted homo-chlorophyllous complexes. Estimated in this way, the ratio of the number of photons emitted by Chl *a* and Chl *b* in homo-chlorophyllous and hetero-chlorophyllous PCP complexes is equal to 3.2 and 3.4, respectively. The insignificant difference indicates that the photophysics of either of the Chl pigments is very similar in homo- and hetero-chlorophyllous complexes.

## 6.4 Simulation of Chl-Chl Energy Transfer

The energy transfer rates calculated above are important parameters that allow to simulate the energy transfer dynamics of the weakly interacting Chls in hetero-chlorophyllous N-PCP complexes using a Monte Carlo approach. This procedure was applied previously for studying energy transfer in phycoerythrocyanin [142]. In general, two chromophores A and B feature fluorescence decay rates  $\gamma_A$  and  $\gamma_B$  as defined by the inverse of the respective fluorescence lifetimes. Energy transfer between them occurs at rates  $\gamma_{AB}$  and  $\gamma_{BA}$  from A to B and B to A, respectively. Random realisations of initial excitation, placed on either of the Chls, can only proceed via the two ways of fluorescence decay or energy transfer to the neighbouring chromophore. Thus, the normalised sum of depopulation rates corresponds to probability  $P=1$ :

$$P = \frac{1}{\gamma_{tot}} (\gamma_{AB} + \gamma_A) = 1, \quad (6.2)$$

where  $\gamma_{tot} = \gamma_{AB} + \gamma_A$ . The simulation starts randomly on one of the chromophores. Using the Mersenne-Twister algorithm [143] a random number  $i$  between 0 and 1 is generated. This number is compared with the probabilities of each way as determined by their rates. For example:

$$\text{if } i \in \left] 0, \frac{\gamma_{AB}}{\gamma_{tot}} \right] \quad \text{energy transfer to B} \quad (6.3)$$

or

$$\text{if } i \in \left[ \frac{\gamma_{AB}}{\gamma_{tot}}, 1 \right[ \quad \text{relaxation of A.} \quad (6.4)$$

The simulation runs until final relaxation via A or B. In order to achieve sufficient statistics the simulation is repeated  $10^7$  times.

For the (Chl *a/b*)-N-PCP complex the simulation shows that, regardless of whether initial excitation is placed on Chl *a* or Chl *b*, the emission occurs more frequently from Chl *b*, with a Chl *a*/Chl *b* ratio of 0.64. This ratio is considerably higher than the one calculated assuming complete thermal equilibration between the two Chls; in this case one obtains a ratio of 0.51. The discrepancy points toward the importance of excitation dynamics in determining the relative fluorescence of the Chls in the hetero-chlorophyllous complex. Moreover, the calculated values are considerably different from the experimentally observed ratio of 1.9. Similar analysis yields the ratios Chl *a*/acChl *a* of 1.31 and Chl *b*/acChl *a* of 0.76 in (Chl *a*/acChl *a*)-N-PCP and (Chl *b*/acChl *a*)-N-PCP, respectively.

The measured intensity ratios depend not only upon Förster energy transfer between the Chl pigments alone, but also on the efficiency of energy transfer from Per to the respective Chl. Recent time-resolved absorption experiments carried out on the ensembles of homo-chlorophyllous complexes discussed in Chapter 3.5 have shown that, when exciting at 530 nm, the energy transfer from Per to Chl is different for Chl *b*, Chl *a*, and acChl *a* ([87] and Table

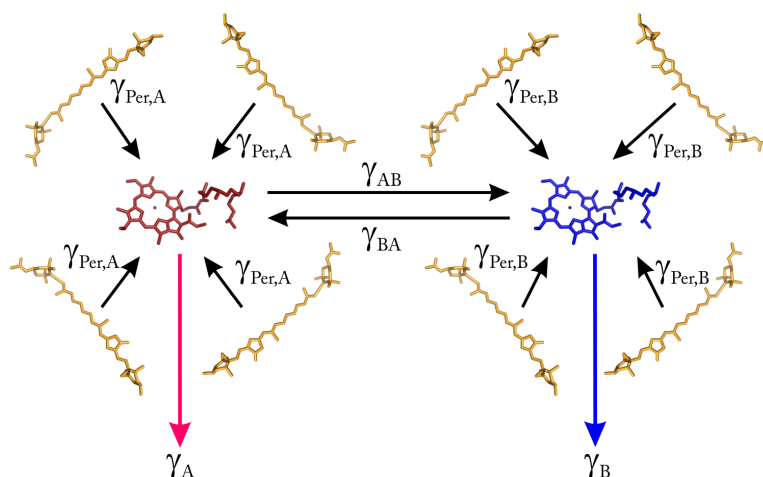


**Figure 6.11:** Schematic diagram of energy transfer pathways for a single hetero-chlorophyllous complex excited at 532 nm. The numbering of Per follows the nomenclature introduced in Chapter 3. The two Per (1 and 4) excited in each of the clusters transfer the excitation to the Chls and after bilateral energy transfer between the Chl the recombination takes place.

3.9). For example for Per-Chl *a* it is 2.7 times faster than the energy transfer from Per to Chl *b*. However, in order to completely explain energy transfer dynamics in the hetero-chlorophyllous complexes all relevant transfer pathways and characteristic times need to be considered (see Figure 6.11).

The ratios of energy transfer efficiency in the hetero-chlorophyllous complexes can be estimated using the average fluorescence intensity ratio obtained by SMS and the calculated excitation distributions. The results are summarised in Table 6.2. For example, the excitation distribution between Chl *a* and Chl *b* equal to 0.64, as calculated by the Monte Carlo simulations, implies a 2.96 times more efficient energy transfer from Per to Chl *a* than from Per to Chl *b*. The agreement between the value of 2.7 measured by Polivka *et al.* [87] and the one calculated with parameters derived from the Monte Carlo simulations suggests that the Chl *a*-Chl *b*

Complexes with	Chl <i>a</i> /acChl <i>a</i>	Chl <i>b</i> /Chl <i>a</i>	Chl <i>b</i> /acChl <i>a</i>
Intensity ratio [MC]	1.31	0.64	0.76
Intensity ratio [SMS]	1.2	1.9	4.1
Per-Chl efficiency [meas.]	1.39	2.70	3.69
Per-Chl efficiency [SMS+MC]	1.2	2.96	5.39

**Table 6.2:** Comparison of relative spectral intensities of hetero-chlorophyllous complexes. Intensity ratios have been estimated using the Monte-Carlo approach described in the text (MC) and measured by SMS. The combination of MC and SMS (SMS+MC) allows to estimate Per-Chl efficiency and compare it to results measured by [87]. Energy transfer rates were calculated from ensemble spectra of hetero-chlorophyllous N-PCP the

system in Chl *a/b*-N-PCP complexes does not reach thermal equilibrium within the excited state lifetime of the Chls. A similar situation is found for energy transfer to acChl *a* and Chl *a*, respectively. Calculation based on the Monte Carlo simulation suggests a ratio of 1.1 compared to 1.39 obtained experimentally. The larger deviation obtained for Chl *b* and acChl *a* is due to unfavourable intensity ratio in the (Chl *b*/acChl *a*)-N-PCP complex as mentioned above. The relative contribution of acChl *a* may therefore be overestimated.

## 6.5 Conclusion

In conclusion, ensemble fluorescence measurements were used to characterise hetero-chlorophyllous N-PCP reconstituted from binary mixtures of Chls. Energy transfer processes between Per and the different Chl molecules as well as between two Chl molecules is apparent in fluorescence excitation spectra. This provided proof that complexes with two different Chls are indeed formed by reconstitution. In N-PCP reconstituted with Chl *a* and Chl *b* the energy transfer takes place in both directions with similar efficiency, while it is mainly unidirectional in terms of the energetically preferable directions for N-PCP reconstituted with Chl *b* and acChl *a*, or with Chl *a* and acChl *a*. Förster energy transfer rates determined from the respective ensemble spectra of homo-chlorophyllous N-PCP allow to qualitatively interpret the results, assuming different population rates from Per to different Chl pigments.

The excitation dynamics in this system can be described quantitatively using the results of SMS, which provides a way to distinguish between homo- and hetero-chlorophyllous complexes in the reconstitution mixture. Analysis of fluorescence spectra of individual complexes yield an average ratio of fluorescence intensity. These findings are reproduced with Monte Carlo simulations performed with the assumption that the energy transfer from Per to Chl varies for different Chls as measured recently by time-resolved transient absorption.

# CHAPTER 7

---

## PCP at the Interface of Metallic Nanostructures

---

The previous chapter has shown how structural reconstitutions of chlorophylls in hetero-chlorophyllous PCP complexes influence spectral observables and energy transfer dynamics. These changes were the result of modified intrinsic transfer rates through reconstitution. One of the possibilities to extrinsically alter optical properties is to place a molecule near metal films and nanoparticles and use plasmon resonances. Plasmons are collective oscillations of electrons that can be the source of strong enhancement of electromagnetic fields. Plasmonic effects have generated considerable interest in recent years and cover research fields such diverse as optical spectroscopy, cell imaging, quantum information processing, nanophotonics, and bio-sensors [14, 15, 144–151]. The research field focused on these processes is called plasmonics.

Section 7.1 presents how plasmons determine the optical properties and local electromagnetic fields of metal nanoparticles. The optical response of an emitter coupled to a plasmonic structure depends upon several parameters like spatial arrangement and its spectral characteristics. Section 7.2 explains the theoretical foundations underlying fluorophore-metal interactions. Whether fluorescence is enhanced through plasmonic interactions is a result of a complicated interplay between radiative and non-radiative decay processes. Metal-enhanced fluorescence has been observed for many hybrid systems like semiconductor nanocrystals and nanowires close to metal nanoparticles [114, 152–157], dye molecules coupled to metal nanoparticles and nanocrystal-nanoparticle bio-conjugates [16, 158–163]. However, experimentally unexplored in this context are light-harvesting complexes. Sections 7.3 and 7.4 present single-molecule- and ensemble-spectroscopy of PCP placed on Silver Island Films (SIF), respectively. Individual silver island nanoparticles give rise to plasmonic interactions and enhance the fluorescence of PCP.

### 7.1 Metal Nanoparticles

The unique optical properties of metallic nanoparticles result from electrodynamic effects and from modification of the dielectric environment. The term “plasmonics” is used to manifest the

central role of plasmon resonances induced by optical excitation. Plasmons or surface plasmon waves are collective oscillations of free electrons located along the metal-dielectric interface. The simple model of a driven classical harmonic oscillator provides an intuitive picture of plasmons. In this model, the incident light field forces the electrons in the conduction band to oscillate with respect to the stationary ions. At times of maximum field amplitude at one side of the nanoparticle, electron excess is generated. The remaining ions establish excess of positive charges at the opposite side (see Figure 7.1). The oscillation of charges generates an electric dipole field outside the nanoparticle and is at maximum when the incident light field meets the resonance condition of the plasmon. This local field enhancement is the source of many photonic applications of metal nanoparticles and plays a major role in MEF effect as well. The model of a light driven harmonic oscillator is surprisingly accurate in explaining basic optical properties of metal nanoparticles. This is partly due to the fact that the overall displacement of the electrons leads to restoring forces that are approximately harmonic [164, 165]. However, as the incident light field penetrates homogeneously into the particle, depending on frequency and material properties, radiative and non-radiative losses lead to damping and need to be considered as well. In case of metal nanostructures, like metal nanoparticles used in this work, plasmon oscillations are localised. This is in clear contrast to plasmons on flat surfaces that can only be excited using special geometries (e.g. the Kretschmann geometry [15]) and require a matching wave vector. To excite plasmons in metal nanoparticles no special geometry, i.e. no matching of wave vector is needed. Plasmon modes in such particles are sometimes referred to as localised surface plasmons.

Metallic nanoparticles feature some unique optical properties [15, 145]. When significantly smaller than the wavelength of light they feature a narrow light absorption within the range of a few nanometres. The absorption peak maximum due to plasmon resonance depends on size and shape of the nanoparticle, as well as on the dielectric environment. The peak maximum of the surface plasmon band is red shifted with increasing particle size. While shift for small particles is rather small, larger particles feature a clear red shift which is accompanied by spectral broadening due to increased damping. The origin of these shifts is not due to quantum confinement but rather, like most other optical characteristics, describable in terms of electrodynamics [14].

Most of the physics involved in light-metal interactions is hidden in the frequency dependence of the metal's dielectric function. A number of theories have been developed, for example by Kelly *et al.*, to explain and predict optical properties of metals but still solutions to Maxwell equations, as provided by classic Mie theory [166, 167], describe most characteristics of metal nanoparticles. Mie theory starts from a dipole approximation similar to the intuitive picture of plasmons sketched above. Oscillation of conduction band electrons (i.e. plasmon oscillations), driven by the electromagnetic field, produces oscillating dipoles along the field direction, where the electrons are driven to the surface of the nanoparticles. A more rigorous theory by Kelly *et al.* [148] is supporting the approach of a dipolar displacement but shows that this model is mainly applicable to smaller-sized particles. The model demonstrates that the optical properties of metallic nanoparticles are mainly governed by their absorption and scattering profiles. As a measure of absorption and scattering strength collectively, the

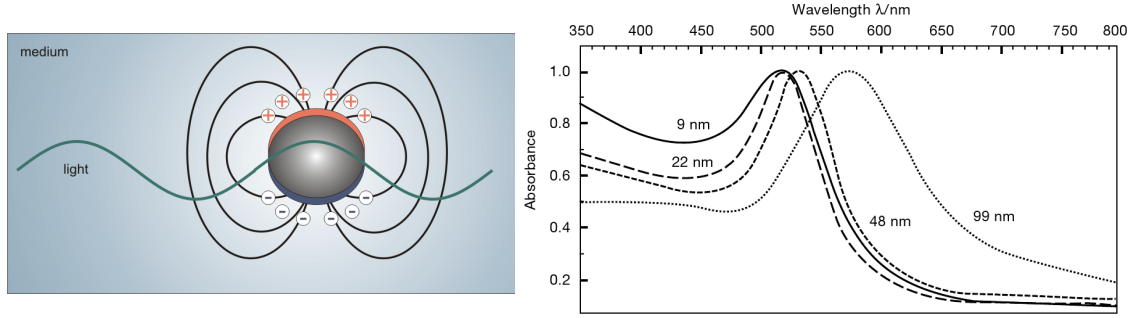


**Figure 7.1:** Left: Schematic plasmon oscillation in a metal nanoparticle. The laser excitation field (shown in green) induces electron oscillations inside the particle which leads to generation of a dipole field outside the nanoparticle. Right: Optical absorption spectra calculated for gold nanoparticles of different sizes; taken from [145]

extinction coefficient  $k_{\text{exc}}$  [168] is defined and reads

$$k_{\text{exc}} = \frac{18\pi N V \varepsilon_h^{3/2}}{\lambda} \frac{\varepsilon_2}{[\varepsilon_1 + 2\varepsilon_h]^2 + \varepsilon_2^2}, \quad (7.1)$$

where  $\lambda$  and  $\varepsilon_h$  correspond to the wavelength of light and the dielectric constant of the surrounding medium, respectively. The terms  $\varepsilon_1$  and  $\varepsilon_2$  represent the real and imaginary part of the dielectric constant of the metal

$$\varepsilon_m(\omega) = \varepsilon_1 + i\varepsilon_2, \quad (7.2)$$

which depends on the excitation frequency  $\omega$ . If  $\varepsilon_2$  is small or only weakly depending on  $\omega$ , maximum absorption, i.e. plasmon resonance condition, is given by  $\varepsilon_1 = -2\varepsilon_h$  and the dominator in Equation (7.2) vanishes. The size dependence of the surface plasmon resonance is determined by the size dependence of the dielectric constant  $\varepsilon$  of the metal, which is frequently called intrinsic size effect [169]. For noble metals, like gold and silver, two contributions to the dielectric constant are distinguished: firstly, from inter-band transitions of inner d-electrons to the conduction band and secondly, from free conduction electrons described in the Drude model [167, 168]. The latter contributions read

$$\varepsilon_D(\omega) = 1 - \frac{\omega_p^2}{\omega^2 + i\Gamma\omega}, \quad (7.3)$$

where  $\omega_p$  and  $\Gamma$  are the plasmon frequency of bulk material and the damping constant related to the width of the plasmon resonance band, respectively. Scattering from particle surfaces becomes important in small nanoparticles and produces the damping term  $\Gamma$  which is inversely proportional to particle radius  $r$ . Via this relation damping introduces the size dependence in  $\varepsilon_D(\omega)$  and thus in  $\varepsilon_1$ . Consequently, the surface plasmon resonance condition also becomes dependent on size. For larger particles (e.g. diameters >25 nm for gold), higher order effects become important. Quadrupolar charge cloud distortion introduce an even more pronounced red shift with particle size, which is often referred to as extrinsic size

effect [169]. Spectral position as well as the shape of plasmon absorption also depends on dielectric constant of surrounding medium  $\epsilon_h$  (see above). An increased constant increases absorption, broadening and red shift as well [168]. Numerical models such as discrete dipole approximation (DDA) have been developed to describe optical properties of large particle sizes and shapes [170] where no analytical expression like the ones presented above can be found.

## 7.2 Fluorophore Metal Interactions

Enhanced electromagnetic fields near metallic nanostructures due to localised plasmon resonances can alter optical properties like fluorescence intensity and lifetime of fluorophores placed in the vicinity of metallic interfaces. The fluorescence of molecules in contact or at small distances to a nanoparticle can also be quenched. Whether fluorescence intensity and fluorescence lifetime of a dye molecule is enhanced or quenched depends on several factors. The most important ones are the geometry of the metal, molecule-metal separation, excitation wavelength and relative spectral position between absorption and emission of the dye with respect to the plasmon resonance of the metal. Depending on these parameters the absorption rate, radiative and non-radiative decay rates of the fluorescent dye are changed.

The interactions between a fluorophore and a metal nanostructure are of three basic types, as described in [15, 171] and references therein:

- **Local Field Enhancement**  
Depending on their size and shape metallic nanostructures exhibit dipole and higher multipole resonances. Excitation of these resonances leads to electron oscillations driven by the incident light. This creates an enhanced local electric field external to the particles.
- **Metal - Dipole Interaction**  
This type of interaction opens an additional channel of non-radiative decay. Similar to Förster type energy transfer it exhibits a strong distance dependence. For fluorophore distances smaller than 5 nm to the metal nanoparticle this decay channel is dominant and most emission is quenched.
- **Enhancement of Radiative Rate**  
Interaction between fluorophore and metal nanostructure can also lead to an increased radiative rate. This is mainly due to an increased density of quantum states corresponding to the energy gap between initial and final states of an optical transition.

Following closely a model presented by Novotny and co-workers [16, 172] this section describes the different types of fluorophore-metal interactions. For this matter, a single molecule located at position  $\mathbf{r}_m$  is represented as a two-level system with a transition dipole moment  $\boldsymbol{\mu}$  and transition frequency  $\omega$ . Furthermore, weak excitation power is assumed, i.e. no saturation effects are considered. Then, the fluorescence rate  $\gamma_{em}$  is a two-step process which

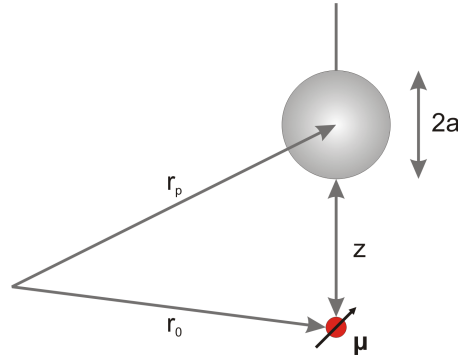


**Figure 7.2:** Definition of coordinate system used in the theoretical model.

involves the excitation rate  $\gamma_{exc}$  and the emission probability, as represented by the quantum yield  $q$ . The fluorescence rate  $\gamma_{em}$  of a single molecule is given by

$$\gamma_{em} = \gamma_{exc} \cdot q = \gamma_{exc} \left[ \frac{\gamma_r}{\gamma} \right], \quad (7.4)$$

with  $\gamma_r$  and  $\gamma$  being the radiative decay rate and the total decay rate, respectively. As there is no coherence between excitation and emission, these two processes can be treated as independent from each other. In terms of the afore introduced rates fluorescence enhancement is expressed as

$$\frac{\gamma_{em}}{\gamma_{em}^0} = \frac{\gamma_{exc}}{\gamma_{exc}^0} \cdot \frac{q}{q^0}, \quad (7.5)$$

with the superscript '0' indicating the corresponding free-space quantity. The term  $\gamma_{exc}/\gamma_{exc}^0$  accounts for enhancement of local fields due to the presence of a metal nanostructure. The excitation rate  $\gamma_{exc}$  is proportional to  $|\mathbf{E} \cdot \mathbf{p}|^2$ , with  $\mathbf{E}(\mathbf{r}_m, \omega)$  being the local excitation field. The term  $q/q^0$  accounts for both changes in radiative and non-radiative decay rates. In the presence of a metallic interface the total decay rate  $\gamma$  is altered and an additional non-radiative decay channel, represented by the decay rate  $\gamma_{metal}$ , is introduced. Thus, the total decay rate reads

$$\gamma = \gamma_r + \gamma_{nr} + \gamma_{metal}. \quad (7.6)$$

Consequently, changed decay rates change the quantum yield as well. Using the definition of  $q^0$  and recasting leads to

$$q = \frac{\gamma_r}{\gamma_r + \gamma_{nr} + \gamma_{metal}} = \frac{\gamma_r/\gamma_r^0}{\gamma_r/\gamma_r^0 + \gamma_{metal}/\gamma_r^0 + (1 - q^0)/q^0}. \quad (7.7)$$

While generally the radiative rate  $\gamma_r$  is changed due to nearby metal interfaces, i.e.  $\gamma_r \neq \gamma_r^0$ , the intrinsic non-radiative rate is assumed to be unaffected, i.e.  $\gamma_{nr} = \gamma_{nr}^0$ . It is instructive to consider the limits of Equation (7.7). At large separations  $d$  between fluorophore and

metal interface, influence of metal interactions can be neglected:  $\gamma_{metal} \rightarrow 0$  and  $\gamma_r \rightarrow \gamma_r^0$ , hence  $q = q^0$ . This result is expected but highlights the explicit distance dependence of metal-fluorophore interactions. At high intrinsic quantum yield  $q^0 = 1$  metal interaction represents the only non-radiative decay channel:  $q = \gamma_r / (\gamma_r + \gamma_{metal})$ . This result indicates that metal enhanced fluorescence should be favourable to dyes of low to medium (intrinsic) quantum yield [173].

The different decay rates and quantum yields for a given particle-molecule as well as particle-material configuration can be derived from multiple multipole (MMP) method [22] as outlined in [16]. Figure 7.3 shows fluorescence enhancement for  $q^0 = 1$  as a function of distance derived in this way (solid curves). The blue curve in Figure 7.3(a) shows how energy transfer depends on distance. For small distances clearly the quantum yield drops to small values, indicating quenching of fluorescence. This effect is largely independent on particle size as for small distances the particle surface can be approximated by a plane boundary. Thus, the means to minimise losses due to energy transfer are the choice of material, excitation frequency and control of the distance between fluorophore and metal nanostructure. On the contrary, radiative decay rate (not shown) and excitation rate (shown in red) are strongly dependent on geometry and can therefore be optimised by design of optical antennae [16, 172]. The dependence of excitation rate on distance however is quite reversed. The highest enhancement occurs at small distances. For a given metal-fluorophore hybrid system enhancement and quenching effects are competing. Figure 7.3(b) shows such a case assuming  $q^0 = 1$  (shown in black). Maximum enhancement is achieved only at an optimal distance [16, 152, 174]. In the following discussion the exact numerical solutions given by MMP are approximated by

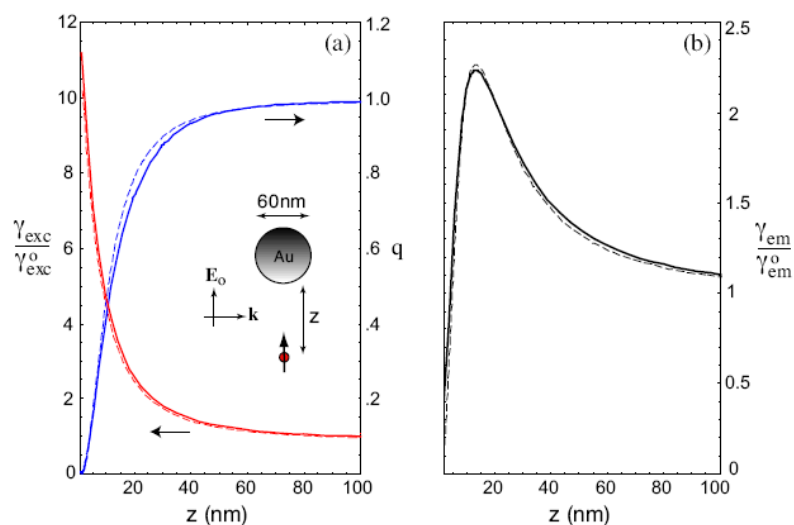


**Figure 7.3:** Fluorescence enhancement near a 60 nm gold nanoparticle excited with wavelength  $\lambda=650$  nm. (a) Quantum yield (blue) and excitation rate enhancement (red) (b) Emission enhancement. The wavelength is taken to be the same as the excitation wavelength. The solid curves are exact results based on the MMP method and the dashed curves are approximations derived in the text (taken from [172]).

modeling the underlying physical principles in Equation (7.5).

### 7.2.1 Local Field Enhancement

Plasmon oscillations are induced by an electromagnetic field  $\mathbf{E}_0 \sim e^{i\omega t}$ , e.g. an incident laser, and damped by scattering processes  $\Gamma$ . The periodic displacement of electrons leads to a secondary field  $\mathbf{E}_s$ , i.e. the enhanced field surrounding the nanoparticle. Overall, the local field in close proximity to the nanoparticle is given by  $\mathbf{E}_{local} = \mathbf{E}_0 + \mathbf{E}_s$  and determines the excitation rate  $\gamma_{exc}$  via

$$\gamma_{exc} \sim |\boldsymbol{\mu} \cdot [\mathbf{E}_0(\mathbf{r}_0, \omega_1) + \mathbf{E}_s(\mathbf{r}_0, \omega_1)]|^2, \quad (7.8)$$

where  $\omega_1$  is the excitation frequency. Treated as a classical oscillator plasmon field amplitude is maximised if the frequency of the incident field corresponds to the resonance frequency of the oscillator  $\omega_0$ , i. e. for small damping  $\omega_{max} \approx \omega_0$ . The smaller the damping  $\Gamma$  the higher the enhancement. The plasmon can be seen as a nano-amplifier of the incident light field. If a fluorophore is situated in close vicinity to a metal nanoparticle it couples to the enhanced plasmon field. As a consequence, the interaction leads to enhanced absorption, i.e. increased  $\gamma_{exc}$ . If this effect is dominant it could enhance fluorescence intensity. Both radiative and non-radiative decay rates remain unchanged, and consequently, so do fluorescence lifetime and quantum yield [174].

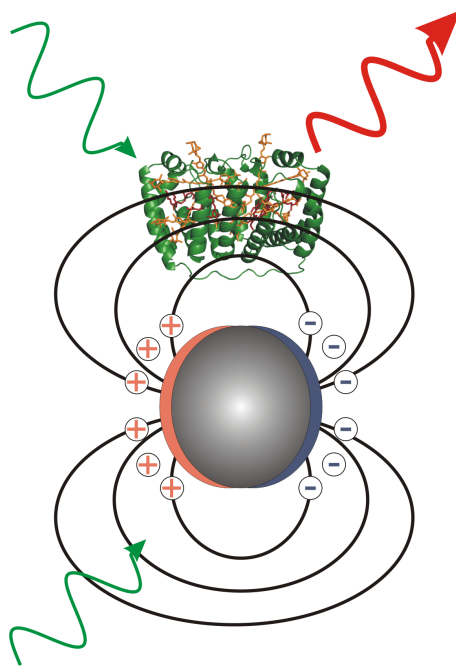


**Figure 7.4:** PCP placed in the enhanced local field of a plasmon. Interaction with the induced plasmon field acts as a nano-amplifier and leads to enhanced absorption of PCP.

The theoretical framework presented in 2.1 allows to derive an analytical expression for the enhancement of the excitation rate. For that matter the nanoparticle is represented by its polarisability  $\bar{\alpha}$ . The secondary field  $\mathbf{E}_s$  is expressed in terms of Green's function and is depending on distance  $\mathbf{r}_0$  and excitation wavelength  $\omega_1$ . For a spherical particle with polarisability  $\bar{\alpha}$  having a diameter  $a \ll \lambda$  the excitation rate enhancement reads

$$\frac{\gamma_{exc}}{\gamma_{exc}^0} = \left| 1 + 2 \frac{a^3}{(a+z)^3} \frac{\varepsilon(\omega_1) - 1}{\varepsilon(\omega_1) + 2} \right|^2 \quad (7.9)$$

where only near-field terms in  $\bar{\mathbf{G}}$  are retained and  $\mu_x = \mu_y = 0$ . The equation highlights the explicit dependence of local field enhancement on geometry and plasmon resonance of the nanoparticle as well as the distance to the chromophore.

### 7.2.2 Metal-Dipole Interaction

Fluorescence enhancement is competing with non-radiative decay caused by energy transfer to the metal nanoparticle which is dominant for small molecule-metal distances ( $d < 10$  nm). The excited dipole of the fluorophore induces plasmon resonances in the nearby nanoparticle. In turn, the induced plasmons feature dipoles themselves that allow them to act as acceptors to energy transfer, removing excitation energy from the donor, i.e. the fluorophore. The dipole-dipole interaction is accounted for by introducing an additional non-radiative decay channel denoted as  $\gamma_{metal}$ . Similar to the discussion of Förster energy transfer in Section 2.2, the corresponding rates are derived from Equation (2.17) which reads

$$\frac{\gamma_{metal}}{\gamma_r^0} = \frac{P_{metal}}{P_0}. \quad (7.10)$$

Thus, the normalised change in energy transfer rates is determined by the ratio of  $P_{metal}$ , the power radiated by the molecule and absorbed in the particle, and  $P_0$ , the power irradiated by a classic dipole with frequency  $\omega_2$  and wave-vector  $k_2 = \omega_2/c$ . In the limit of very small distances the curvature of the nanoparticle can be neglected and the environment, as seen by the molecule, is to a good approximation a plain interface. This allows the use of electrostatic image theory as shown in [22] and to calculate the power emitted by the molecule and absorbed inside a half-space with a dielectric constant  $\varepsilon(\omega_2)$ . The energy transfer rate follows as

$$\frac{\gamma_{metal}}{\gamma_r^0} = \frac{3}{16} \text{Im} \left( \frac{\varepsilon(\omega_2) - 1}{\varepsilon(\omega_2) + 1} \right) \frac{1}{k_2^3 z^3} \frac{(\mu_x^2 + \mu_y^2 + \mu_z^2)}{|\boldsymbol{\mu}|^2}, \quad (7.11)$$

where  $z$  corresponds to the molecule-surface separation and  $\boldsymbol{\mu} = [\mu_x, \mu_y, \mu_z]$ . Equation (7.11) was derived by integrating over the dissipated power density  $(\omega_2 \varepsilon_0 / 2) \text{Im}\{\varepsilon\} \mathbf{E}^* \cdot \mathbf{E}$ ,  $\mathbf{E}$  being the electrostatic dipole field over the volume of the half-space. Higher-order multipole correction terms can be considered and are discussed in [175–177]. In contrast to the effect of enhanced

absorption, quenching due to energy transfer between fluorophore and metal nanoparticle changes both fluorescence lifetime and quantum yield.

An optimal distance for highest fluorescence enhancement is determined by the interplay between enhanced absorption and quenching. Both processes show a distinct distance dependence. Given a spherical particle of radius  $a=2.5$  nm and a distance of  $d=1$  nm with respect to the fluorophore quenching would be  $\sim 43$  times higher than enhancement in absorption. For  $d=15$  nm the ratio drops down to  $\sim 1.6$  [171]. A more detailed description of metal-dipole interactions and quenching due to energy transfer to metal nanoparticles was derived by Gersten and Nitzan [178]. They showed that quenching depends as well on the shape of the nanoparticle. In their model two limits are of special interest. For large particles (as compared to the wavelength) they predict  $\gamma_{metal}/\gamma_r^0$  to depend on distance as in Equation (7.9). The case  $a \rightarrow \infty$  is equivalent to continuous metal films [175, 179]. However, in the limit of infinite particle radius, i.e.  $a=0$ , they find

$$\frac{\gamma_{metal}}{\gamma_r^0} \sim d^{-6}, \quad (7.12)$$

which is similar to a Förster type description of energy transfer.

Equation (7.9) shows that maximum fluorescence enhancement is achieved if the plasmon is excited exactly at its resonance frequency  $\omega_0$ . If however, the fluorophore happens to emit at that same frequency, i.e.  $\omega_0 = \omega_2$  energy transfer efficiently competes with excitation enhancement. At  $\omega_2$  the total dipole moment of the fluorophore is at maximum and accordingly the overall power irradiated by the molecule and the nanoparticle is maximised. At the same time losses due to energy transfer are at maximum, as well [171]. Thus, in order to achieve optimal fluorescence enhancement, plasmon and fluorophore absorption should overlap but overlap with fluorescence emission should be as small as possible [171, 174, 180].

### 7.2.3 Enhancement of Radiative Rate

Another source of possible fluorescence enhancement is through change of radiative decay rate  $\gamma_r$ . The radiative rate is defined by the transition dipole moment (see Equation 2.15). The photon mode density  $\rho$  at frequency  $\omega$  corresponds to the energy gap between initial and final states of an optical transition. This density term can be substantially increased by localising a fluorophore within nanoscopic distances from a metal surface. The fluorophore does not have to be in direct contact with the particle. The effect can be understood as a microcavity effect that enhances the density of photon states [15].

The enhancement of radiative rates is expressed in terms of classic physics using again Equation (2.17) which reads

$$\frac{\gamma_r}{\gamma_r^0} = \frac{P_r}{P_0}. \quad (7.13)$$

The transition dipole moment of the fluorophore  $\boldsymbol{\mu}$  irradiates the overall power  $P_0$ . The plasmon is excited through the scattered light originating at the fluorophore of power  $P_r$ . If only dipole terms are considered, the normalised radiative decay rate is determined by Green's function of the system and reads

$$\frac{\gamma_r}{\gamma_r^0} = \frac{|\boldsymbol{\mu}_{induced} + \boldsymbol{\mu}|^2}{|\boldsymbol{\mu}|^2} = \left| 1 + 2 \frac{a^3}{(a+z)^3} \frac{\varepsilon(\omega_2) - 1}{\varepsilon(\omega_2) + 2} \right|^2. \quad (7.14)$$

For simplicity  $\mu_x = \mu_y = 0$  and a spherical particle of polarisability  $\bar{\alpha}$  was assumed. Enhancement is at a maximum at  $z = 0$  and amounts to  $|3\varepsilon/(\varepsilon + 2)|^2$  for vertically aligned molecule ( $\mu_x = \mu_y = 0$ ) and  $|3/(\varepsilon + 2)|^2$  for a horizontally aligned molecule ( $\mu_z = 0$ ). It is instructive to note that for small distances  $z$  the competing energy transfer rate goes to infinity and the quantum yield drops to zero. Enhancement due to a changed radiative decay rate can be omitted for small distances and quantum yield in Equation (7.7) becomes a function of material and distance only. As pointed out in [172] maximum fluorescence occurs if the fluorophore emission is slightly red-shifted with respect to the plasmon resonance of the metal nanoparticle. Equations (7.14) and (7.9) appear identical because of the restricted dipole orientations. In general however, arbitrary dipole orientations result in different expressions as dipoles interfere in Equation (7.9) whereas in (7.14) they don't. From Equation (7.6) it is apparent that a changed radiative decay rate results in changed lifetimes and quantum yields. Equations (7.11) and (7.14) show that the quantum yield next to a nanoparticle as defined in Equation (7.7) is a function of dielectric constant  $\varepsilon$  and polarisability  $\bar{\alpha}$ , i. e. shape of the particle. Whereas the radiative rate  $\gamma_r$  depends on both shape and material of the particle, i.e.  $\varepsilon$  and  $\bar{\alpha}$ , the energy transfer rate  $\gamma_{metal}$  depends on material properties ( $\varepsilon$ ) only.

### 7.3 Single PCP Complexes on SIF

Metal-enhanced fluorescence has been frequently reported for fluorophores deposited near silver islands [152, 153, 178, 181, 182]. Such films can be produced as described in Chapter 4.2 and are constituted of irregularly spread nano-scale spherical and elliptical silver particles (see Figure 7.5). The inherent coarseness of such films gives rise to strong surface curvature leading to high electric fields as, in analogy, are known to form at metal tips as a function of their surface shape as well. In many cases the proximity to SIF results in a preferential increase in intensity of low quantum yield fluorophores, and lifetime has been reported to decrease as the intensities increase [181]. In order to study plasmonic interactions between SIF and PCP complexes SMS is highly advantageous [13]. Both the inherent heterogeneity of SIFs and the sensitivity of MEF to distance and orientation in the metal-PCP system (see Figure 7.5) render it difficult to gain detailed insight into plasmonic interactions based only on ensemble spectroscopy. Nevertheless, the latter allows for qualitative analysis of the plasmonic effects and thus accompanies SMS.

Cover-slips prepared with highly diluted PCP samples used for these experiments were covered

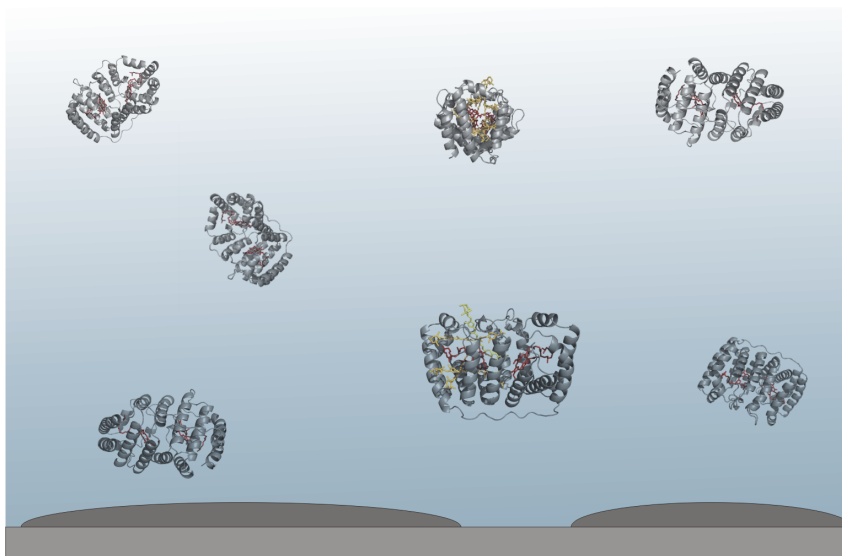


**Figure 7.5:** PCP monomers on SIF embedded in PVA polymer matrix. The cover-slip (shown in grey) is covered with silver islands (dark grey). Their diameters range from 70 to 140 nm, and their heights are between 30 and 40 nm. PCP complexes feature different orientation and distance with respect to the SIF.

with SIF on both sides. Absorption of fluorescence emission of PCP at 673 nm by the SIF was insignificant. However, excitation with 532 nm is effectively absorbed by the SIF layer. The laser was adjusted to yield identical excitation powers for PCP on SIF and the reference on glass. Power was measured right after the cover-slip. As discussed in Chapter 3 the excitation wavelength of 532 nm corresponds to the Per absorption, therefore the Chls are excited via the energy transfer, which randomises any polarisation of the excitation. Figure 7.6 shows representative spectra, measured with identical laser power of 15  $\mu\text{W}$  for individual PCP complexes deposited on SIF (red) and glass (green) cover-slips. The single molecule spectrum in green is the same in each graph and serves as a reference. The emission of the PCP complexes on the glass cover-slips are comparable to results presented in Chapter 5 and [132, 140]. By contrast, the fluorescence intensity of the complexes placed close to SIF show enhanced fluorescence intensity but individual complexes feature different intensities which are due to different enhancement factors.

Figure 7.7 shows the intensities measured for over sixty PCP complexes on glass (green) and SIF surfaces (red). On average, the fluorescence increases by a factor of 6 (average intensities for PCP on glass and on SIF are 90 and 540 counts per second, respectively), but some complexes show even an 18-fold increase with respect to the average intensity on glass. The significant broadening of the intensity distribution obtained for PCP complexes on SIF layer provides not only a clear proof for efficient coupling between metal and bio-molecule but is also a direct consequence of inhomogeneities characteristic for the chosen geometry [114]. First, the size variation of silver nanoparticles in the SIF layer, as observed using AFM (see Figure 4.1), results in a broad distribution of fluorescence enhancement factors for individual PCP complexes. Therefore, the PCP fluorescence intensity is expected

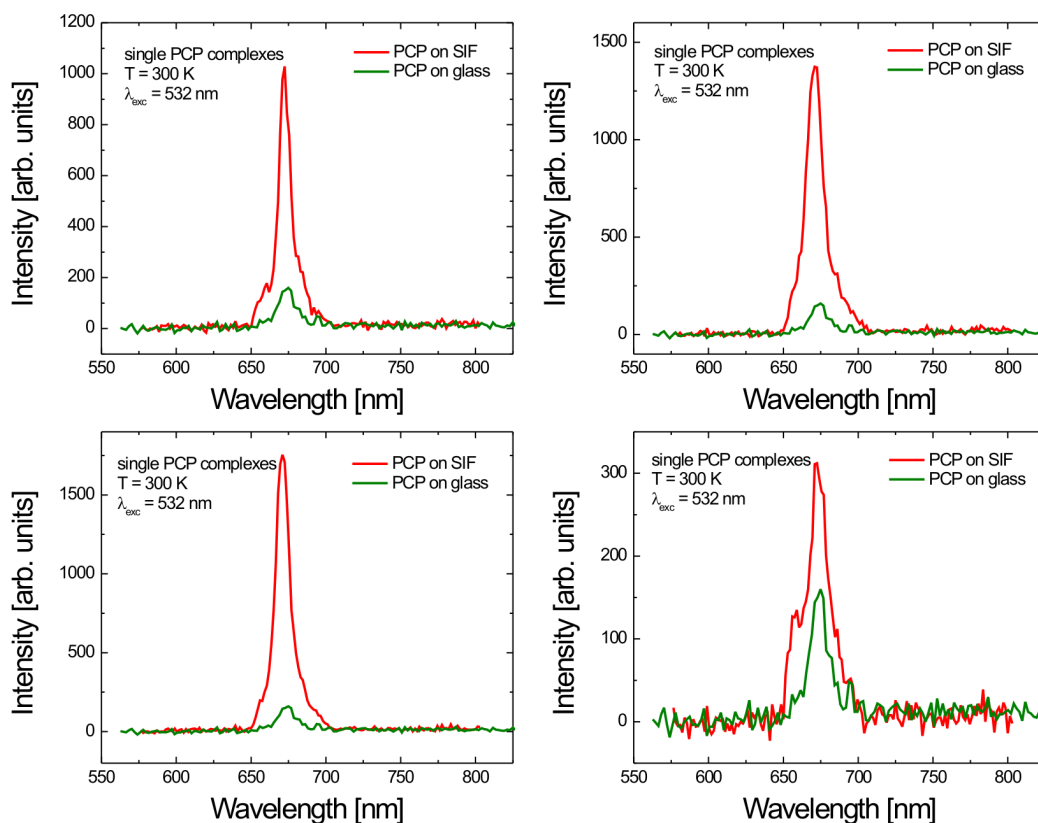


**Figure 7.6:** Typical fluorescence spectra of individual PCP complexes SIF cover-slips (in red) excited at 532 nm. For reference the same spectrum of a single PCP complex on glass is depicted in each graph (in green).

to reflect the heterogeneity of the system. In addition, the interaction mechanisms between the metal surface and the pigments (Per and Chl), as discussed in Section 7.2, depend on the distance [183]: fluorescence is quenched for PCP complexes located directly on the SIF surface, while fluorescence of the ones separated by approximately 50 nm or more should remain unaffected. A signature of the latter is presumably the fraction of PCP complexes on SIF with intensities below 200 counts per second, which is comparable to signals measured for the reference sample. On the other hand, an indirect indication for the quenching could be smaller (by approximately 15%) number of PCP molecules per unit area observed for SIF cover-slips.

Importantly, neither the linewidth nor the wavelength of the PCP fluorescence are affected by the proximity of the silver metal film. The distribution of maximum emission wavelengths measured for over sixty PCP complexes on SIF (see Figure 7.7) is centred at 673 nm, and matches almost perfectly the distribution obtained for PCP on the glass surface in Chapter 5 and [140]. Therefore it is safe to conclude that the protein surrounding the pigments remains intact

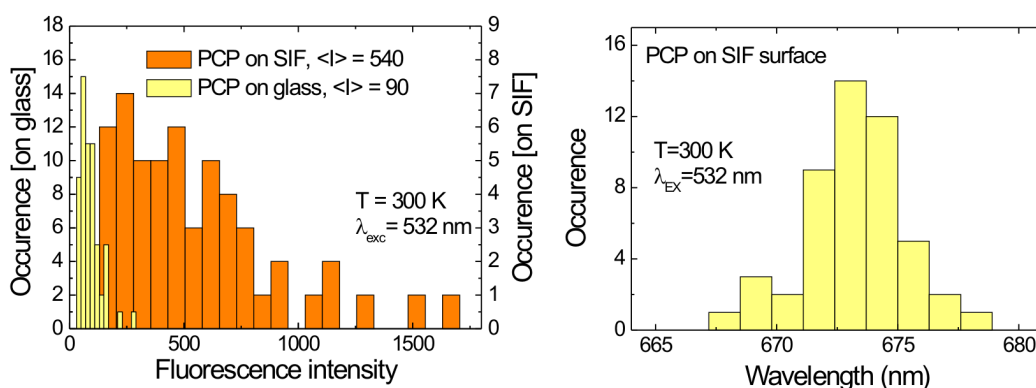


**Figure 7.7:** Left: Distribution of fluorescence intensity measured for over sixty single PCP complexes on glass (green) and SIF-coated cover-slips. Right: Distribution of maximum emission energies for PCP complexes deposited on SIF-covered cover-slip.

during the experiment, and the complex as a whole maintains its light-harvesting function. This is also supported by the efficient energy transfer between Per and Chl (used for Chl excitation), which critically depends on the distance between the pigments.

## 7.4 Ensemble Characterisation

MEF is also apparent from ensemble spectroscopy measured on more concentrated PCP samples deposited under otherwise identical conditions on SIF and bare glass cover-slips. The samples were excited at 532 and 633 nm (see Figure 7.8). As discussed in Chapter 3 these two excitation wavelengths excite PCP via Per and subsequent energy transfer to Chl or via direct Chl absorption, respectively (see Figure 7.8). In each case, 10 spectra were collected at different locations on the cover-slip to judge the influence of local fluctuations of PCP concentration. The preparations were found homogeneous with standard intensity deviations of less than 15%. The spectra shown in Figure 7.8 are close to average ones with red and green lines representing PCP complexes deposited on SIF and bare glass cover-slips, respectively. For both excitation wavelengths, the fluorescence intensity of PCP complexes on SIF is clearly increased compared to the reference samples. For PCP excited into Per absorption (532 nm), a 6-fold enhancement of the fluorescence intensity is observed which is in perfect agreement with the single molecule results. The enhancement is even larger (8.5-fold), when the light-harvesting complexes are excited directly into the blue wing of the Chl  $Q_y$ -band (633 nm).

Both the wavelength and the linewidth of the emission remain unaffected by the support, as observed on a single molecule level, and by the excitation wavelength. The curves obtained by multiplying the spectra measured for the reference samples by the respective enhancement factors (black points in Figure 7.8), match perfectly the fluorescence spectra of PCP complexes

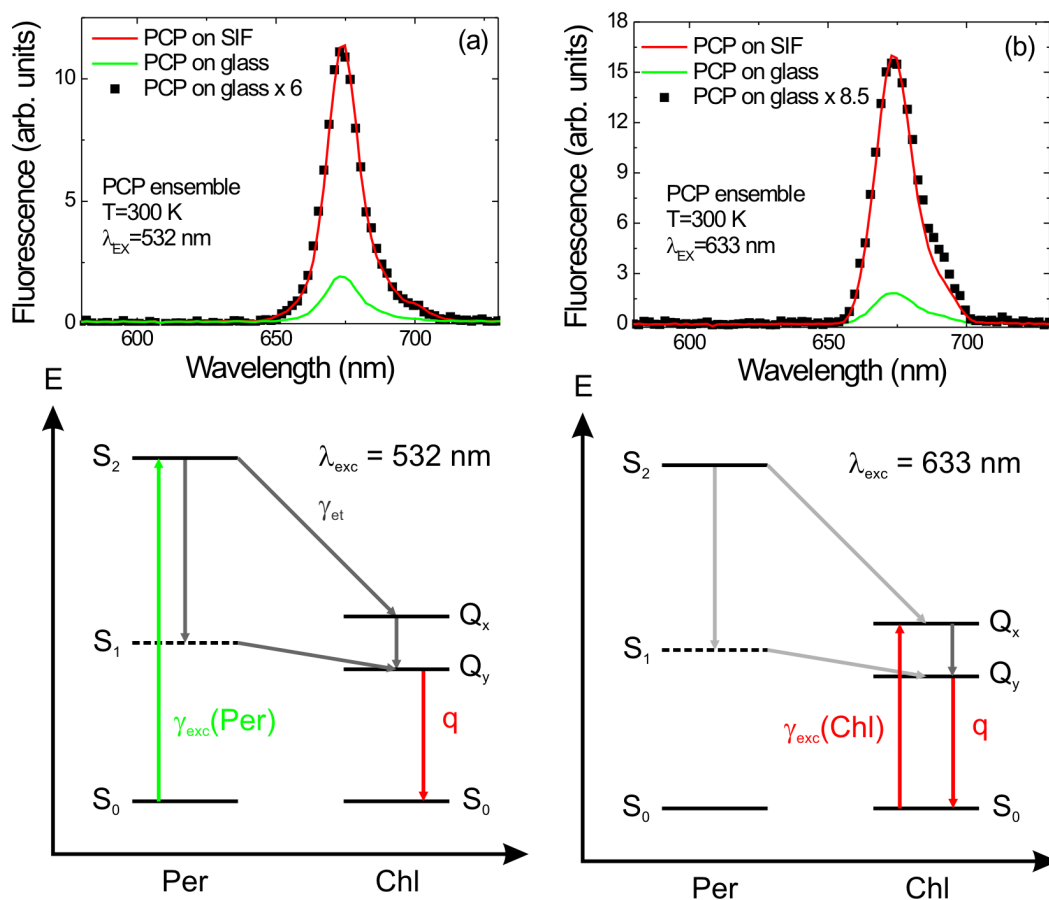


**Figure 7.8:** (a) Average fluorescence emission spectra measured for PCP ensembles on bare glass (green) and SIF-coated cover-slips (red) excited at 532 nm. Black points correspond to the spectrum measured for PCP on glass multiplied by a factor of six. (b) Average fluorescence emission spectra measured for PCP ensembles on bare glass (green) and SIF-coated cover-slips (red) excited at 633 nm. Black points correspond to the spectrum measured for PCP on glass multiplied by a factor of 8.5. The bottom row shows the excitation pathways and involved rates at 532 and 633 nm, respectively.

on SIF substrates. This reinforces the conclusion reached based on single-molecule data that the protein structure of PCP complexes is unaffected in any significant way by the presence of metal nanostructures in its vicinity and that observed fluorescence enhancement is due to extrinsic effect caused by the SIF.

## 7.5 Enhancement Mechanism

The optical effects observed both with SMS and ensemble spectroscopy are associated with MEF of PCP near silver islands. Additional observations presented in this sections allow to

conclude on possible enhancement mechanisms. In general, as discussed above, the observed effects are the result of the interplay between excitation by the incident local field and emission of radiation as a consequence of radiative and non-radiative decay [16]. In other words, the source of these processes is the external radiation field or the complexes themselves, respectively.

Photo-stability is an important photo-physical quantity and roughly proportional to the time a fluorophore remains in the excited state [173]. Thus, the rate of photo-bleaching could provide clues on the impact of radiative rate upon the observed fluorescence enhancement of PCP near silver islands. Figure 7.9 (see above) examines the time evolution of the fluorescence intensity measured for PCP ensembles excited at 532 nm. The emission intensity of the reference sample decreases by  $\sim 10\%$  over the first 30 s, that of the PCP complexes coupled to SIF decreases during this time by  $\sim 50\%$ . The increased photo-bleaching on SIF indicates a dominant role of enhanced local fields in the vicinity of SIFs. The Chls in PCP could realise a larger number of photo-cycles leading to enhanced emission intensity. In contrast, an enhanced radiative decay rate would increase photo-stability and compete with the influence of local fields. Thus, the data suggests that radiative decay rate could change but on average does not play a prominent role in the chosen geometry. The rate of photo-bleaching of PCP on SIF surface increases also if PCP is excited directly into the Chl absorption at 633 nm. However, the effect is less pronounced. Interestingly, direct excitation of Chls leads already to a faster photo-bleaching of the PCP complexes deposited on the glass surface, as compared to excitation via Per. This can be qualitatively understood by an incomplete energy transfer from Per to Chl [181], resulting in a smaller number of photo-cycles in a given time. The dominant influence of local fields to the metal enhanced fluorescence of PCP near SIFs is in good agreement with its spectral properties. PCP complexes feature large spectral overlap of their Per related absorption bands and plasmon absorption of SIF. As a result of efficient energy transfer from to the chlorophylls PCP's fluorescence emission occurs highly red-shifted. As discussed in Section 7.2 quenching effects are due to energy transfer between dipoles. Small spectral overlap with the red-shifted emission dipole moment effectively decreases in the influence of non-radiative decay rates due to the presence of the metal.

Further information about the exact mechanism of fluorescence enhancement can be deduced from the excited-state dynamics. As discussed in Section 7.2 non-radiative and radiative decay rates of a fluorophore are influenced in the vicinity of a metal. Changes in these rates are apparent in the fluorescence lifetime. Figure 7.9 shows the fluorescence decay of PCP complexes on SIF (red line) and that of the reference sample (green line). The fluorescence signal of PCP on glass, as discussed in Chapter 5.1, decays mono-exponentially with a lifetime of  $\tau = 3.68$  ns. In contrast, the fluorescence of PCP complexes deposited on SIF decays much faster and features a multiexponential behaviour. The lifetime of the high-intensity component is as short as 200 ps. At later times, the trajectory gradually approaches that of PCP on glass cover-slips. At times  $> 1$  ns both curves are parallel to each other. The complex and multiexponential decay of lifetime mirrors the sample heterogeneity. It shows contributions from PCP complexes interacting with metal nanostructures of different sizes, as well as distribution of the interaction strength due to changes in distances between the SIF layer and the pigments in the complex. Because of this structural heterogeneity it is not

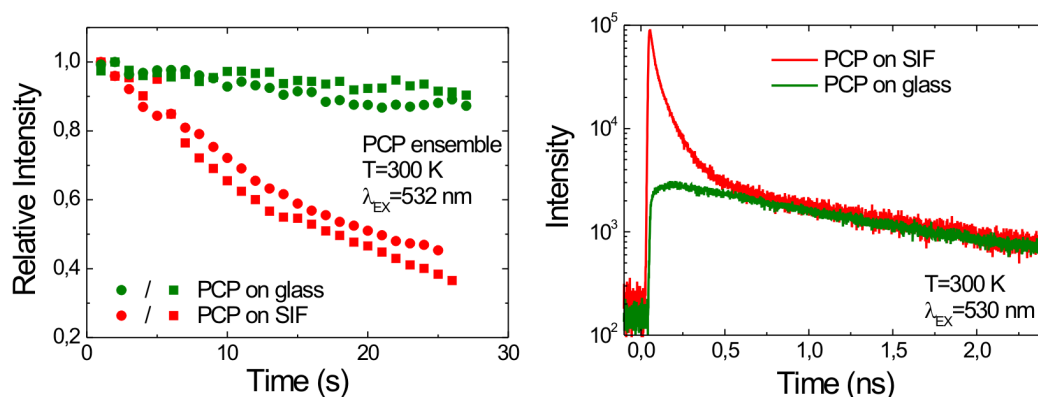


**Figure 7.9:** Left: Temporal evolution of the fluorescence intensity of PCP ensembles on bare glass (green) and SIF-coated cover-slips (red). The excitation wavelength was 532 nm. Dots and squares represent two independent measurements for each configuration. Right: Time-resolved fluorescence of PCP on bare glass (green) and SIF-coated cover-slips (red). The excitation wavelength was 532 nm, and the pulse width was 150 fs.

possible to separate the individual contribution of changes of non-radiative and radiative decay rates to the shortening of lifetimes. This would demand an increased control of distances as well as relative orientations in the PCP-Silver system. However, even in such a geometry it remains a difficult task to separate the individual contributions of non-radiative and radiative decay rates to the shortening of lifetimes. As discussed in Chapter 7.2, the radiative decay rate could increase the quantum yield whereas non-radiative rates always shortens the lifetime. An upper boundary of the quantum yield can be deduced from SMS by measuring the number of photons emitted per time [9].

The higher fluorescence enhancement found for PCP on SIF excited at 633 nm may indicate changes in energy transfer rates. As discussed above, the extended overlap of the absorption spectrum of PCP and SIF suggests a dominant influence of enhanced local fields at 532 nm excitation. At 633 nm this effect should be considerably decreased due to smaller spectral overlap. However, the excitation mechanism is qualitatively different as shown in Chapter 3. With the laser wavelength of 633 nm, only Chl molecules are excited and thus the increase of the fluorescence intensity is only due to plasmonic interaction with Chls. On the other hand, the excitation at 532 nm corresponds almost exclusively to Per absorption and the excited states of the Chls are populated via subsequent energy transfer [140]. It has been shown that plasmonic interactions alter the apparent Förster distances for donors and acceptors bound to DNA [181]. Thus, because the Per absorption as well as the efficiency of energy transfer could be affected by the proximity of the metal film [181], both these processes contribute to the experimentally observed fluorescence enhancement. As they cannot be separated from each other, it is not possible to directly compare the results obtained for the two excitation wavelengths of 532 and 633 nm.

The experimentally observed MEF of single light-harvesting complexes can be qualitatively anal-

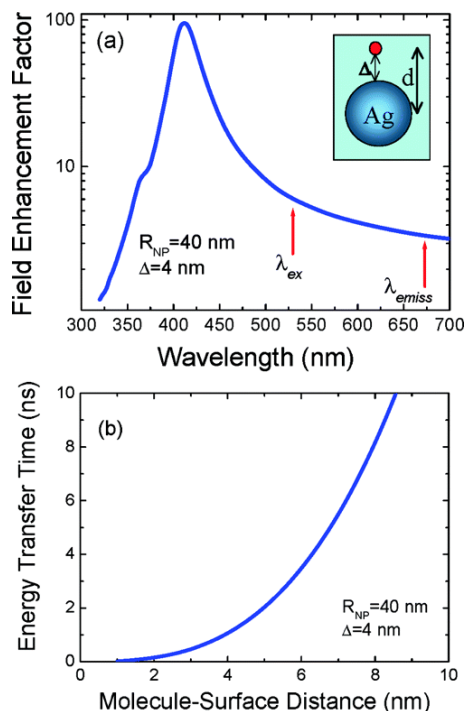


**Figure 7.10:** (a) Electric-field enhancement calculated for Ag NP with radius  $R = 40$  nm and an Ag NP-PCP distance = 4 nm. The inset shows the geometry used in the calculations. (b) Dependence of the energy transfer time on the distance between the PCP complex and an Ag NP of radius  $R = 40$  nm.

used with a simple model that has been applied previously to metal nanoparticle-nanocrystal assemblies [156, 181]. Based on the discussion presented in Section 7.2, it offers a way to obtain numerical expressions to estimate enhancement factors due to metal-fluorophore interactions. The analysis also provides an intuitive scenario, where an increased absorption in the presence of the metal film is the dominant mechanism of fluorescence enhancement. For simplicity, the plasmonic interaction is calculated between a PCP complex and a silver nanoparticle with a diameter of 40 nm and assumed that the fluorescence of PCP is non-polarised. This neglects the size distribution of the metal nanoparticles in SIF, as well as any polarisation and anisotropy effects of PCP emission, i.e. two Chl molecules are approximated by a single dipole. Details are published in [184].

Figure 7.10(a) shows the electric-field enhancement  $P(\lambda_{exc})P(\lambda_{em})$  calculated numerically for a PCP complex placed 4 nm away from a spherical silver nanoparticle with a radius of  $R_{NP} = 40$  nm.  $P(\lambda_{em})$  accounts for changes in emission and  $P(\lambda_{exc})$  for absorption properties of the fluorophore. The obtained enhancement factors for the absorption and emission are  $P(\lambda_{exc} = 532\text{nm}) \sim 6$  and  $P(\lambda_{em} = 673\text{nm}) \sim 3.4$ , respectively. These values indicate that the fluorescence enhancement observed for single PCP molecules on SIF surface is primarily due to increased probability of photon absorption,  $P(\lambda_{exc})$ , which results from an excitation wavelength that is closer to the plasmon resonance of the silver nanoparticle ( $\sim 450$  nm) than the emission wavelength of 673 nm. Of course, the enhancement factor  $P(\lambda_{exc})P(\lambda_{em})$

depends strongly on the distance between the silver nanoparticle and the PCP complex and on the size of the nanoparticle. Keeping the nanoparticle radius constant at  $R_{NP} = 40$  nm, effective enhancement factors of  $P(\lambda_{exc} = 532\text{nm})P(\lambda_{em} = 673\text{nm}) \sim 19\text{-}2$  are obtained for silver nanoparticle-PCP distances of  $\Delta = 4\text{-}20$  nm. On the other hand, for larger sizes of  $R_{NP} = 100$  nm, the total fluorescence increase factor of the PCP complex separated by a constant 4 nm is larger than 30. These values agree well with fluorescence enhancements observed experimentally. The fluorescence decay measured for PCP on SIF (see Figure 7.9) shows strongly shortened lifetime of PCP complexes that are presumably very close to the silver surface. Taking an average decay rate of  $1\text{ ns}^{-1}$  results at fluorescence decrease by a factor of  $\gamma/\gamma^0 \sim 4$ . Because the experimentally observed fluorescence is increased by an average factor of  $I_{em}/I_{em}^0 \sim 6$  (excitation at 532 nm), the effective enhancement factor for PCP complexes in the vicinity of silver nanoparticles is remarkably high, reaching  $P(\lambda_{exc})P(\lambda_{em}) \sim 24$ .

Strongly shortened lifetimes measured for PCP molecules placed on SIF are also consistent with the picture of Förster-like interactions with metal. The averaged energy transfer time can be estimated similarly to Equation (7.11) as shown in [184]. Using an optical dipole moment of PCP  $p_{exc} \approx 1\text{ \AA}$  and  $\Delta = 4$  nm results at  $\gamma_{metal} = 1\text{ ns}^{-1}$  and  $\gamma = 1.4\text{ ns}^{-1}$ . This corresponds to the lifetime of  $\tau = 1/\gamma = 0.7$  ns, which agrees well with the experimental values. The dependence of the energy transfer time on the distance between a PCP complex and the silver nanoparticle plotted in Figure 7.10(b) suggests that the complexes exhibiting very short lifetimes must be located within a few nanometres from the metal surface.

## 7.6 Conclusion

In conclusion, fluorescence of single light-harvesting PCP complexes deposited on an SIF surface can be enhanced by plasmonic interactions. On average fluorescence intensity increases by a factor of 6, in some cases up to 18-fold compared to the average reference without metal. The PCP complexes remain intact despite the presence of the metal film, but they photo-bleach more rapidly due to increased number of photocycles. This indicates a dominant influence of local plasmonic fields on the overall enhancement mechanism. Fluorescence lifetime is considerably shortened attributable to changes in non-radiative and radiative decay rates. An increased control of distances and relative orientation between PCP and silver nanoparticles is needed to characterise the relative contributions of these rates to the enhancement of fluorescence.

The experimental findings are supported by model calculations of the electric-field enhancement of both absorption and emission, which outweigh any fluorescence quenching due to the silver nanoparticles. Thus, under the experimental conditions, the observed fluorescence enhancement is mainly due to the absorption increase, although it is also possible that the presence of silver nanoparticles affects the energy transfer from Per to Chl.

# CHAPTER 8

---

## Summary and Conclusions

---

Light-harvesting complexes like the water-soluble Peridinin-Chlorophyll-Protein (PCP) play a central role during the very first steps of photosynthesis. PCP is a unique system within the vast variety of known complexes. In contrast to most other light-harvesting complexes where Chlorophylls (Chl) play a central role, in PCP the main light-harvesting pigment is a carotenoid, Peridinin (Per). Pers lend PCP a broad absorption ranging from 450 to 550 nm filling the green gap not all accessible to Chls. In its native form PCP from dinoflagellate *Amphidinium (A.) carterae* is a trimer which was solved with 2 Å resolution by E. Hofmann *et al.* in 1996 [7]. Each monomer is comprised of two subunits each carrying one Chl *a* and four Pers. The Pers are in van der Waals contact to Chl *a*. The Chls *a* in a single monomer feature a distance of 17.4 Å, distances between Chls *a* in different monomers range from 40 to 54 Å. All pigments are enclosed in a hydrophobic protein cavity.

Work initially conducted by D. J. Miller *et al.* in 2005 [94] showed that PCP can be reconstituted with different Chls. N-domain apoproteins expressed in *Escherichia coli* are topologically equivalent to one half of a native PCP monomer. Mixed with Per and Chl pigments such apoproteins refold and yield “halfmers” that dimerise to form complexes homolog to native monomers. This way complexes form that only contain Chl *a* ((Chl *a*)<sub>2</sub>-N-PCP), Chl *b* ((Chl *b*)<sub>2</sub>-N-PCP) and [3-acetyl]-Chl *a* ((acChl *a*)<sub>2</sub>-N-PCP), so called homo-chlorophyllous N-PCP complexes. These samples have been produced in close collaboration with the group of H. Scheer (Department of Biology, LMU München). Furthermore, PCP can be reconstituted with binary mixtures of different Chls, so called hetero-chlorophyllous complexes. In order to achieve this, halfmers containing different Chls were mixed and dimerised to form a monomer [95]. Complexes containing Chl *a*/Chl *b*, Chl *b*/acChl *a* and Chl *a*/acChl *a* were produced. One of the central questions addressed in this thesis was whether such complexes indeed form during reconstitution and how the non-native pigments alter properties like energy transfer and pigment interactions in the complexes. Ensemble spectroscopy alone could not sufficiently answer this question as it provides no means to separate contributions of homo-chlorophyllous complex. Reconstitution produced both hetero- and homo-chlorophyllous complexes in a single mixture. Thus, single molecule spectroscopy (SMS) was used to not only complement

ensemble spectroscopy but to gain a very direct insight into pigment interactions and energy transfer of single PCP complexes.

The broad absorption related to Pers and very efficient energy transfer from Per to Chl provided an interesting possibility to excite Chl fluorescence [139]. Using this excitation scheme it was possible to perform experiments both at the ensemble and single molecule level. Single PCP complexes featured high photo-stability and their fluorescence emission could be followed for tens of seconds without any significant blinking. This property allowed for construction of trajectories of emission spectra of a great number of single complexes. The majority of traces of homo-chlorophyllous complexes showed characteristic step-wise photo-bleaching [132]. Interestingly, bleaching of one chromophore didn't leave any measurable effect on the spectral properties of the remaining one. These findings indicate weak dipole-dipole coupling of the two Chls embedded in a single PCP monomer and are in good agreement with recent literature. Similar step-wise bleaching is apparent for native PCP as well. However, due to the three times bigger number of Chls assignment of steps to individual Chls is only tentative. Nevertheless, fluorescence trajectories of native PCP are as well in agreement with weak dipole-dipole coupling between all Chls embedded in the trimer. As a consequence of these experiments it can be concluded that individual Chls in PCP are essentially independent from each other and can thus be monitored individually. Using just a single laser for excitation the two Chls in a homo-chlorophyllous PCP complexes could be distinguished from each other. The data indicated that the two Chls in a single complex are not isoenergetic which was previously discussed in the literature. This is probably due to slightly different local environments the Chls experience within the protein cavity. The Chls act as local reporters of their local chemical surroundings and indicate pigment-protein interactions [139]. Most importantly, the spectra of single hetero-chlorophyllous complexes showed emission lines of two different Chls are clearly separable in all samples. This clearly proves that such complexes indeed form as a result of reconstitution with mixtures of Chls.

The different hetero-chlorophyllous N-PCP complexes are interesting model systems that allow to study energy transfer processes in a well characterised and biologically relatively simple structure. SMS allowed for detailed investigations of such processes as a function of the reconstituted pigments for single complexes. The individual contributions of the different Chls could be readily distinguished by the narrow single molecule emission spectra and interpreted based on Förster theory of energy transfer. Fluorescence excitation spectra revealed the most prominent energy transfer pathways. The complexes containing either Chl *b* and acChl *a* or Chl *a* and acChl *a* predominantly showed unidirectional transfer towards the energetically favourable pigment. In contrast to that, in (Chl *a*/Chl *b*)-N-PCP a bidirectional transfer between both Chls was apparent. SMS allowed to record the relative fluorescence of each Chl in single hetero-complexes and simulations based on the Monte-Carlo approach resembled the average intensities [140, 185]. Based on Förster-type energy transfer rates extracted from ensemble absorption and emission spectra, as well as fluorescence lifetimes and quantum yield measured for the homo-chlorophyllous samples the relaxation pathways could be modelled. The rates for (Chl *a*/Chl *b*)-N-PCP are comparable and suggest that energy transfer is indeed bidirectional. However, the observed relative fluorescence intensities can only be explained considering energy transfer from Per to Chls as well. More precisely, the data suggests that

energy transfer from Per to Chl *a* is 2.96 times more efficient than the respective transfer from Per to Chl *b*. Similar results were obtained for all hetero-chlorophyllous samples. The deduced differences in energy transfer efficiencies between Per and Chls are in good agreement with results obtained by time-resolved transient absorption spectroscopy published by T. Polivka *et al.* in 2005 [87]. For example, these measurements indicate a 2.7 times more efficient energy transfer from Per to Chl *a* than from Per to Chl *b*.

Proteins are complicated systems that dynamically change their conformational states. Such conformations are defined by complex potential hyper-surfaces with multiple barriers separating potential energy valleys associated with different substates. Transitions between these states are usually driven by temperature, but can as well be photo-induced. Pigment-protein complexes are especially well-suited to study protein dynamics because of their intrinsic fluorescence properties. The embedded Chl molecules act as reporters of their immediate environment and change their spectral properties as a function of protein dynamics. The fluorescence spectra of single (Chl *a*)<sub>2</sub>-N-PCP revealed photo-induced spectral dynamics attributed to structural changes in the surrounding protein cavity [186]. Fluorescence linewidth recorded for many single (Chl *a*)<sub>2</sub>-N-PCP complexes changed considerably as a function of excitation power. Broadening of the inhomogeneous linewidth indicates changes of protein conformation. This result is further enforced by the distribution of emission maxima recorded for some 100 single complexes. The distributions broaden as a function of excitation power as well.

In recent years plasmonic interactions between metal nanoparticles and fluorophores have gathered a lot of attention. Many examples in literature showed how the vicinity to metal nanostructures changes the spectral properties of dye molecules. Plasmonic interactions between PCP and silver nano-islands considerably increased the excitation rate of PCP apparent as enhanced fluorescence [184]. Ensemble spectroscopy as well as SMS showed an average six-fold increase of fluorescence intensity. Some cases showed even an 18-fold increase as compared to reference data without silver influence. Metal-enhanced fluorescence didn't leave any measurable impact on the protein structure and is observable for both direct excitation and excitation via Per to Chl energy transfer. A simple theoretical model suggests that enhancement is mainly due to increased absorption caused by electric local fields induced by plasmon resonances. These lead to increased fields internal to the PCP light-harvesting antennae. Changes in radiative and non-radiative decay rates are apparent in reduced lifetimes and photo-stability.

In conclusion, the results obtained in the course of thesis contribute to an increased understanding of light-harvesting strategies based on carotenoids in general, and in particular deepened the understanding of pigment interactions and energy transfer in PCP. T. Polivka *et al.* [84] showed by investigation of the Fucoxanthin-Chlorophyll-Protein (FCP) antenna that certain structural characteristics of carotenoids are a recurring theme in the photosynthesis of marine algae (unpublished results). Furthermore, FCP highlights ways to construct artificial light-harvesting systems based on carotenoids. The metal-enhanced fluorescence of PCP near metal nanoparticles suggests similar applications. However, for such approaches to be successful an increased control of distances and relative orientations in the light-harvesting-metal

hybrid is essential. This would allow to control optical properties of light-harvesting complexes, natural or artificial. Future directions could lie in the application of bio-conjugates employing e.g. streptavidin-biotin linkers.

---

## Bibliography

---

- [1] Blankenship, R. *Molecular Mechanisms of Photosynthesis*; Blackwell Publishers, 2001. [1](#), [17](#), [25](#), [27](#), [55](#)
- [2] Emerson, R.; Arnold, W. J. *Gen. Physiol.* **1932**, *15*, 391–420. [1](#)
- [3] Emerson, R.; Arnold, W. J. *Gen. Physiol.* **1932**, *16*, 191–205. [1](#)
- [4] Deisenhofer, J.; Epp, O.; Miki, K.; Huber, R.; Michel, H. *Nature* **1985**, *318*, 618–624. [1](#)
- [5] *For the determination of the three-dimensional structure of a photosynthetic reaction centre*, Press release of The Royal Swedish Academy of Sciences, 1988. [1](#)
- [6] McDermott, G.; Prince, S. M.; Freer, A. A.; Hawthornthwaite-Lawless, A. M.; Papiz, M. Z.; Cogdell, R. J.; Isaacs, N. W. *Nature* **1995**, *374*, 517 – 521. [1](#)
- [7] Hofmann, E.; Wrench, P. M.; Sharples, F. P.; Hiller, R. G.; Welte, W.; Diederichs, K. *Science* **1996**, *272*, 1788–1791. [2](#), [34](#), [39](#), [44](#), [45](#), [57](#), [59](#), [65](#), [68](#), [70](#), [107](#)
- [8] Förster, T. *Annalen der Physik* **1948**, *437*, 55–75. [2](#), [81](#)
- [9] Demtröder, W. *Laserspektroskopie: Grundlagen und Techniken*; Springer, Berlin, 2007. [2](#), [104](#)
- [10] Valeur, B. *Molecular Fluorescence: Applications and Principles*; Wiley-VCH Verlag, 2002. [2](#), [66](#), [67](#)
- [11] multiple authors, *Single Molecule Detection in Solution*; Wiley-VCH Verlag, 2003. [3](#), [16](#), [51](#)
- [12] multiple authors, *Single Molecule Optical Detection, Imaging and Spectroscopy*; VCH, Weinheim, 1997. [16](#)
- [13] multiple authors, *Single Molecule Spectroscopy-Nobel Conference Lectures*; , Eds.; Springer: Berlin, 2001.; Springer, 2001. [3](#), [98](#)
- [14] Maier, S. A. *Plasmonics. Fundamentals and Applications*; Springer, Berlin, 2007. [3](#), [89](#), [90](#)
- [15] Prasad, P. N. *Nanophotonics*; John Wiley & Sons, 2004. [3](#), [89](#), [90](#), [92](#), [97](#)
- [16] Anger, P.; Bharadwaj, P.; Novotny, L. *Phys. Rev. Lett.* **2006**, *96*, 113002. [3](#), [89](#), [92](#), [94](#), [103](#)

- [17] Plakhotnik, T.; Donley, E. A.; Wild, U. P. *Annu. Rev. Phys. Chem.* **1997**, *48*, 181–212. [5](#), [51](#)
- [18] Tamarat, P.; Maali, A.; Lounis, B.; Orrit, M. *J. Phys. Chem. A* **2000**, *104*, 1–16. [9](#)
- [19] Moerner, W. J. *Phys. Chem. B* **2002**, *106*, 910–927. [58](#)
- [20] Kulzer, F.; Orrit, M. *Annu. Rev. Phys. Chem.* **2004**, *55*, 585–611. [17](#), [20](#)
- [21] Butter, J. Y. P.; Hecht, B.; Crenshaw, B. R.; Weder, C. *The Journal of Chemical Physics* **2006**, *125*, 154710. [5](#)
- [22] Novotny, L.; Hecht, B. *Principles of Nano-Optics*; Cambridge University Press, 2006. [5](#), [7](#), [8](#), [9](#), [10](#), [13](#), [15](#), [18](#), [20](#), [21](#), [23](#), [94](#), [96](#)
- [23] Stratton, J. A. *Electromagnetic Theory*; McGraw-Hill, New York, 1946. [6](#)
- [24] Banavar, J. R.; Maritan, A. *Annu. Rev. Biophys. Biomol. Struct.* **2007**, *36*, 261–280. [9](#), [71](#)
- [25] Frauenfelder, H. *Proc. Natl. Acad. Sci. USA* **2002**, *99 Suppl 1*, 2479–2480. [9](#)
- [26] Atkins, P.; Friedman, R. *Molecular Quantum Mechanics*, 4th ed.; Oxford University Press, USA, 2005. [10](#)
- [27] Levine, I. N. *Quantum Chemistry*, 5th ed.; Prentice Hall, 1999. [10](#), [14](#), [16](#)
- [28] Davydov, A. S. *Am. J. Phys.* **1963**, *31*, 220–220. [10](#)
- [29] Grondelle, R. V.; Valkunas, L.; Amerongen, H. V. *Photosynthetic Excitons*; World Scientific Publishing Co Pte Ltd, 2000. [11](#)
- [30] Knox, R. S.; Gulen, D. *Photochem. Photobiol.* **1993**, *57*, 40–43. [11](#)
- [31] Jensen, F. *Introduction to Computational Chemistry*; John Wiley & Sons, 1998. [14](#)
- [32] Scholes, G. D. *Annu. Rev. Phys. Chem.* **2003**, *54*, 57–87. [16](#)
- [33] Scholes, G. D.; Fleming, G. R. *Adv. Chem. Phys.* **2005**, *132*, 132.
- [34] Scholes, G. D.; Rumbles, G. *Nature Mat.* **2006**, *5*, 683–696. [16](#)
- [35] Moerner, W. E.; Orrit, M. *Science* **1999**, *283*, 1670–1676. [17](#)
- [36] Eggeling, C.; Widengren, J.; Rigler, R.; Seidel, C. *Analytical Chemistry* **1998**, *70*, 2651–2659. [17](#)
- [37] Kong, X.; Nir, E.; Hamadani, K.; Weiss, S. *J. Am. Chem. Soc.* **2007**, *129*, 4643–4654.
- [38] Eggeling, C.; Widengren, J.; Brand, L.; Schaffer, J.; Felekyan, S.; Seidel, C. A. M. *J Phys Chem A* **2006**, *110*, 2979–2995. [17](#)
- [39] Christ, T.; Kulzer, F.; Bordat, P.; Basché, T. *Angew. Chem., Int. Ed.* **2001**, *40*, 4192–4195. [17](#)
- [40] Murphy, D. B. *Fundamentals of Light Microscopy and Electronic Imaging*; John Wiley & Sons, Inc., New York, 2001. [19](#)
- [41] Abbé, E. *Arch. Mikrosk. Anat.* **1873**, *9*, 413–468. [19](#)
- [42] Rayleigh, L. *Philosophical Magazine* **1896**, *5*, 167–195. [19](#)

- [43] Hell, S. W. *Nature Biotechnol.* **2003**, *21*, 1347–1355. [20](#)
- [44] Hell, S. W.; Dyba, M.; Jakobs, S. *Curr. Opin. Neurobiol.* **2004**, *14*, 599–609.
- [45] Hell, S. W. *Science* **2007**, *316*, 1153–1158. [20](#)
- [46] Axelrod, D. *Methods. Enzymol.* **2003**, *361*, 1–33. [20](#), [23](#)
- [47] Wazawa, T.; Ueda, M. *Adv. Biochem. Eng. Biotechnol.* **2005**, *95*, 77–106. [20](#), [23](#)
- [48] Moerner, W. E.; Fromm, D. P. *Rev. Scient. Inst.* **2003**, *74*, 3597–3619. [20](#)
- [49] Minsky, M. *Scanning* **1988**, *10*, 128–138. [20](#)
- [50] Pawley, J. B. *Handbook of Biological Confocal Microscopy*; Springer, 2006. [20](#)
- [51] Webb, R. *Reports on Progress in Physics* **1996**, *59*, 427–471(45). [20](#), [21](#), [22](#), [23](#)
- [52] Richards, B.; Wolf, E. *Proceedings of the Royal Society of London. Series A, Mathematical and Physical Sciences (1934-1990)* **1959**, *253*, 358–379. [21](#), [23](#)
- [53] Kirstein, J. Ph.D. thesis, LMU München: Faculty of Chemistry and Pharmacy, 2007. [23](#), [48](#)
- [54] Sitte, P.; Ziegler, H.; Ehrendorfer, F. *Strasburger - Lehrbuch der Botanik für Hochschulen*; Spektrum Akad. Vlg., 2002. [25](#), [27](#)
- [55] Berg, J.; Tymoczko, J.; Stryer, L. *Biochemistry*; W. H. Freeman, New York, 2002. [26](#)
- [56] Nield, J. *Cartoon model: structures of the protein complexes involved in the Z-scheme of photosynthesis*, <http://www.photosynthesis.sbc.sqmul.ac.uk/nield/index.html>, 2007, Queen Mary, University of London. [27](#)
- [57] Green, B. R.; Anderson, J. M.; Parson, W. W. In *Light-Harvesting Antennas in Photosynthesis*; Green, B. R., Parson, W. W., Eds.; Kluwer Academic Publishers, 2003; Vol. 13, Chapter 1: Photosynthetic membranes and their light-harvesting Antennas, pp 1–28. [28](#)
- [58] Willstätter, R.; Stoll, A. *Untersuchungen über Chlorophyll*; Springer, Berlin, 1913. [28](#)
- [59] Scheer, H. In *Chlorophylls and Bacteriochlorophylls: Biochemistry, Biophysics, Functions and Applications*. Springer Verlag; Grimm, B., Porra, R. J., Rüdiger, W., Scheer, H., Eds.; Springer, 2005; Chapter An Overview of Chlorophylls and Bacteriochlorophylls: Biochemistry, Biophysics, Functions and Applications, pp 1–26. [28](#)
- [60] Scheer, H. In *Light-Harvesting Antennas in Photosynthesis*; Green, B. R., Parson, W. W., Eds.; Kluwer Academic Publishers, 2003; Vol. 13, Chapter 2: The pigments, pp 29–81. [28](#), [31](#), [33](#)
- [61] Weiss, C. In *The Porphyrins*; Dolphin, D., Ed.; Academic Press, New York, 1978; Chapter Optical spectra of chlorophylls, pp 211–224. [30](#)
- [62] Mantoura, R. F. C.; Wright, S. W. E. *Phytoplankton pigments in oceanography*; UNESCO Publications, Paris, 1997. [29](#)
- [63] multiple authours, *Chlorophylls and Bacteriochlorophylls*; Advances in Photosynthesis and Respiration; Springer, 2006. [29](#)

- [64] Gouterman, M. *J. Mol. Spec.* **1961**, *6*, 138–163. [30](#)
- [65] Weiss, C. *J. Mol. Spectr.* **1972**, *44*, 37–80. [30](#)
- [66] Kleima, F. J.; Hofmann, E.; Gobets, B.; van Stokkum, I. H.; van Grondelle, R.; Diederichs, K.; van Amerongen, H. *Biophys. J.* **2000**, *78*, 344–353. [30](#), [40](#), [57](#), [62](#), [66](#), [81](#)
- [67] Scheer, H. Personal Communication, 2008. [31](#)
- [68] Krane, J.; Aakermann, T.; Liaaen-Jensen, S. *Magn. Reson. Chem.* **1992**, *30*, 1169–1177. [31](#)
- [69] Yamano, Y.; Ito, M. *J. Chem. Soc.* **1993**, *Perkin Trans. 1*, 1599 – 1610. [31](#)
- [70] Polívka, T.; Sundström, V. *Chem. Rev.* **2004**, *104*, 2021–2071. [32](#), [33](#)
- [71] Mimuro, M.; Nagashima, U.; Takaichi, S.; Nishimura, Y.; Yamazaki, I.; Katoh, T. *Biochim. Biophys. Acta. - Bioenergetics* **1992**, *1098*, 271–274. [32](#)
- [72] Bautista, J.; Connors, R.; Raju, B.; Hiller, R.; Sharples, F.; Gosztola, D.; Wasielewski, M.; Frank, H. *J. Phys. Chem. B* **1999**, *103*, 8751–8758. [32](#), [36](#), [37](#), [39](#), [44](#)
- [73] Frank, H.; Bautista, J.; Josue, J.; Pendon, Z.; Hiller, R.; Sharples, F.; Gosztola, D.; Wasielewski, M. *J. Phys. Chem. B* **2000**, *104*, 4569–4577. [32](#), [36](#), [37](#)
- [74] Zigmantas, D.; Polivka, T.; Hiller, R.; Yartsev, A.; Sundstrom, V. *J. Phys. Chem. A* **2001**, *105*, 10296–10306. [32](#)
- [75] Zigmantas, D.; Hiller, R. G.; Sharples, F. P.; Frank, H. A.; Sundström, V.; Polívka, T. *Phys. Chem. Chem. Phys.* **2004**, *6*, 3009 – 3016. [32](#), [33](#)
- [76] Polívka, T.; Herek, J. L.; Zigmantas, D.; Akerlund, H. E.; Sundström, V. *Proc. Natl. Acad. Sci. USA* **1999**, *96*, 4914–4917. [32](#)
- [77] Vaswani, H.; Hsu, C.-P.; Head-Gordon, M.; Fleming, G. *J. Phys. Chem. B* **2003**, *107*, 7940–7946. [33](#)
- [78] Zigmantas, D.; Hiller, R.; Yartsev, A.; Sundstrom, V.; Polivka, T. *J. Phys. Chem. B* **2003**, *107*, 5339–5348. [39](#)
- [79] Papagiannakis, E.; Larsen, D.; vanStokkum, I.; Vengris, M.; Hiller, R.; vanGrondelle, R. *Biochemistry* **2004**, *43*, 15303–15309. [33](#)
- [80] Papagiannakis, E.; Vengris, M.; Larsen, D.; vanStokkum, I.; Hiller, R.; vanGrondelle, R. *J. Phys. Chem. B* **2006**, *110*, 512–521. [36](#), [38](#), [39](#)
- [81] Shima, S.; Ilagan, R.; Gillespie, N.; Sommer, B.; Hiller, R.; Sharples, F.; Frank, H.; Birge, R. *J. Phys. Chem. A* **2003**, *107*, 8052–8066.
- [82] Premvardhan, L.; Papagiannakis, E.; Hiller, R. G.; van Grondelle, R. *J. Phys. Chem. B* **2005**, *109*, 15589–15597.
- [83] Zimmermann, J.; Linden, P.; Vaswani, H.; Hiller, R.; Fleming, G. *J. Phys. Chem. B* **2002**, *106*, 9418–9423. [32](#), [37](#)
- [84] Polívka, T.; Hiller, R. G.; Frank, H. A. *Arch. Biochem. Biophys.* **2007**, *458*, 111–120. [32](#), [37](#), [39](#), [41](#), [57](#), [109](#)

- [85] Linden, P.; Zimmermann, J.; Brixner, T.; Holt, N.; Vaswani, H.; Hiller, R.; Fleming, G. J. *Phys. Chem. B* **2004**, *108*, 10340–10345. [33](#), [38](#)
- [86] Zigmantas, D.; Hiller, R. G.; Sundstrom, V.; Polivka, T. *Proc. Natl. Acad. Sci. USA* **2002**, *99*, 16760–16765. [37](#), [38](#), [39](#)
- [87] Polivka, T.; Pascher, T.; Sundström, V.; Hiller, R. G. *Photosynth. Res.* **2005**, *86*, 217–227. [33](#), [39](#), [56](#), [78](#), [86](#), [87](#), [109](#)
- [88] Frank, H. A.; Cogdell, R. J. *Photochem. Photobiol.* **1996**, *63*, 257–264. [33](#)
- [89] Cogdell, R. J.; Howard, T. D.; Bittl, R.; Schlodder, E.; Geisenheimer, I.; Lubitz, W. *Philos Trans R Soc Lond B Biol Sci* **2000**, *355*, 1345–1349. [33](#)
- [90] Cogdell, R. J.; Isaacs, N. W.; Freer, A. A.; Arrelano, J.; Howard, T. D.; Papiz, M. Z.; Hawthornthwaite-Lawless, A. M.; Prince, S. *Prog. Biophys. Mol. Biol.* **1997**, *68*, 1–27. [33](#)
- [91] Alexandre, M. T. A.; Lührs, D. C.; van Stokkum, I. H. M.; Hiller, R.; Groot, M.-L.; Kennis, J. T. M.; van Grondelle, R. *Biophys. J.* **2007**, *93*, 2118–2128. [33](#)
- [92] Taylor, F. J. R. *The Biology of Dinoflagellates*; Blackwell Science Inc, 1987. [34](#)
- [93] Macpherson, A. N.; Hiller, R. G. In *Light-Harvesting Antennas in Photosynthesis*; Green, B. R., Parson, W. W., Eds.; Kluwer Academic Publishers, 2003; Vol. 13, Chapter 11: Light Harvesting Systems in Chlorophyll c-Containing Algae, pp 323–352. [34](#)
- [94] Miller, D. J.; Catmull, J.; Puskeiler, R.; Tweedale, H.; Sharples, F. P.; Hiller, R. G. *Photosynth. Res.* **2005**, *86*, 229–240. [34](#), [37](#), [38](#), [40](#), [43](#), [44](#), [54](#), [76](#), [107](#)
- [95] Brotosudarmo, T. H. P.; Hofmann, E.; Hiller, R. G.; Wörmke, S.; Mackowski, S.; Zumbusch, A.; Bräuchle, C.; Scheer, H. *FEBS Lett* **2006**, *580*, 5257–5262. [35](#), [43](#), [77](#), [78](#), [80](#), [107](#)
- [96] Brotosudarmo, T. H. P.; Mackowski, S.; Hofmann, E.; Hiller, R. G.; Bräuchle, C.; Scheer, H. *Photosynth. Res.* **2008**, *95*, 247–252. [35](#), [77](#)
- [97] Song, P. S.; Koka, P.; Prézelin, B. B.; Haxo, F. T. *Biochemistry* **1976**, *15*, 4422–4427. [35](#), [38](#)
- [98] Prézelin, B. B.; Haxo, F. T. *Planta* **1976**, *128*, 133–141. [35](#)
- [99] Ogata, T.; Kodama, M.; Nomura, S.; Kobayashi, M.; Nozawa, T.; Katoh, T.; Mimuro, M. *FEBS Lett.* **1994**, *356*, 367–371. [35](#)
- [100] Kleima, F. J.; Wendling, M.; Hofmann, E.; Peterman, E. J.; van Grondelle, R.; van Amerongen, H. *Biochemistry* **2000**, *39*, 5184–5195. [35](#), [36](#), [53](#), [54](#), [55](#), [62](#), [65](#), [66](#), [68](#), [76](#)
- [101] Carbonera, D.; Giacometti, G.; Segre, U.; Hofmann, E.; Hiller, R. *J. Phys. Chem. B* **1999**, *103*, 6349–6356. [36](#), [54](#), [55](#), [80](#)
- [102] Ilagan, R. P.; Shima, S.; Melkozernov, A.; Lin, S.; Blankenship, R. E.; Sharples, F. P.; Hiller, R. G.; Birge, R. R.; Frank, H. A. *Biochemistry* **2004**, *43*, 1478–1487. [36](#), [37](#), [40](#)
- [103] Ilagan, R. P.; Chapp, T. W.; Hiller, R. G.; Sharples, F. P.; Polivka, T.; Frank, H. A. *Photosynth. Res.* **2006**, *90*, 5–15. [36](#), [37](#), [56](#), [80](#)

- [104] Damjanović, A.; Ritz, T.; Schulten, K. *Biophys. J.* **2000**, *79*, 1695–1705. [37](#), [38](#), [62](#)
- [105] Akimotoa, S.; Takaichib, S.; Ogatac, T.; Nishimuraa, Y.; Yamazakia, I.; Mimurod, M. *Chem. Phys. Lett.* **1996**, *260*, 147 – 152. [37](#), [38](#)
- [106] Bautista, J.; Hiller, R.; Sharples, F.; Gosztola, D.; Wasielewski, M.; Frank, H. *J. Phys. Chem. A* **1999**, *103*, 2267–2273. [38](#)
- [107] Krueger, B. P.; Lampoura, S. S.; van Stokkum, I. H.; Papagiannakis, E.; Salverda, J. M.; Gradinaru, C. C.; Rutkauskas, D.; Hiller, R. G.; van Grondelle, R. *Biophys. J.* **2001**, *80*, 2843–2855. [38](#), [39](#)
- [108] Krikunova, M.; Lokstein, H.; Leupold, D.; Hiller, R. G.; Voigt, B. *Biophys. J.* **2006**, *90*, 261–271. [39](#), [64](#)
- [109] Polívka, T.; Pascher, T.; Hiller, R. G. *Biophys. J.* **2008**, *94*, 3198–3207. [40](#)
- [110] Robert, B.; Cogdell, R. J.; van Grondelle, R. In *Light-Harvesting Antennas in Photosynthesis*; Green, B. R., Parson, W. W., Eds.; Kluwer Academic Publishers, 2003; Vol. 13, Chapter 5: The Light-Harvesting System of Purple Bacteria, pp 169–194. [40](#)
- [111] Omata, T.; Murata, N. *Photochem. Photobiol.* **1986**, *31*, 183–185. [44](#)
- [112] Struck, A.; Cmiel, E.; Katheder, I.; Scheer, H. *FEBS Lett.* **1990**, *268*, 180–184. [44](#)
- [113] Schulte, T.; Hiller, R. G.; Hofmann, E. unpublished data. [45](#), [59](#)
- [114] Ray, K.; Badugu, R.; Lakowicz, J. R. *J. Am. Chem. Soc.* **2006**, *128*, 8998–8999. [46](#), [89](#), [99](#)
- [115] Seebacher, C. F. Ph.D. thesis, LMU München: Faculty of Chemistry and Pharmacy, 2002. [48](#), [49](#)
- [116] Hellriegel, C. Ph.D. thesis, LMU München: Faculty of Chemistry and Pharmacy, 2005. [48](#)
- [117] Rutkauskas, D.; Novoderezhkin, V.; Cogdell, R. J.; van Grondelle, R. *Biophys. J.* **2005**, *88*, 422–435. [51](#), [63](#), [71](#), [74](#)
- [118] Scherz, A.; Rosenbach-Belkin, V.; Michalski, T.; Worcester, D. In *Chlorophylls*; Scheer, H., Ed.; CRC Press, Boca Raton, FL, 1991; Chapter Chlorophyll aggregates in aqueous solutions, p 237–268. [54](#)
- [119] Hanson, L. In *Chlorophylls*; Hugo Scheer, H., Ed.; CRC Press, Boca Raton, FL, 1991; Chapter Molecular orbital theory of monomer pigments, p 993–1014. [54](#)
- [120] Kobayashi, M.; Akiyama, M.; Kano, H.; Kise, H. In *Chlorophylls and Bacteriochlorophylls: Biochemistry, Biophysics, Functions and Applications*; Grimm, B., Porra, R., Rüdiger, W., Scheer, H., Eds.; Springer, Berlin, 2006; Chapter Spectroscopy and structure determination, p 79–94. [54](#)
- [121] Williams, A. T. R.; Winfield, S. A.; Miller, J. N. *Analyst.* **1983**, *108*, 1067 – 1071. [57](#)
- [122] Law, C. J.; Cogdell, R. J. *FEBS Lett.* **1998**, *432*, 27–30. [63](#), [67](#)
- [123] Ying, L.; Xie, X. *J. Phys. Chem. B* **1998**, *102*, 10399–10409. [63](#)

- [124] Bopp, M. A.; Jia, Y.; Li, L.; Cogdell, R. J.; Hochstrasser, R. M. *Proc. Natl. Acad. Sci. USA* **1997**, *94*, 10630–10635. [63](#)
- [125] Bopp, M. A.; Sytnik, A.; Howard, T. D.; Cogdell, R. J.; Hochstrasser, R. M. *Proc. Natl. Acad. Sci. USA* **1999**, *96*, 11271–11276. [63](#), [71](#)
- [126] Forkey, J. N.; Quinlan, M. E.; Goldman, Y. E. *Prog. Biophys. Mol. Biol.* **2000**, *74*, 1–35. [66](#)
- [127] Ha, T.; Laurence, T. A.; Chemla, D. S.; Weiss, S. *J. Phys. Chem. B* **1999**, *103*, 6839–6850. [66](#)
- [128] Cotlet, M.; Hofkens, J.; Köhn, F.; Michiels, J.; Dirix, G.; Guyse, M. V.; Vanderleyden, J.; Schryver, F. C. D. *Chem. Phys. Lett.* **2001**, *336*, 415–423. [66](#)
- [129] Loos, D.; Cotlet, M.; Schryver, F. D.; Habuchi, S.; Hofkens, J. *Biophys. J.* **2004**, *87*, 2598–2608. [66](#)
- [130] Lieb, M. A.; Zavislan, J. M.; Novotny, L. *J. Opt. Soc. Am. B* **2004**, *21*, 1210–1215. [66](#)
- [131] Böhmer, M.; Enderlein, J. *J. Opt. Soc. Am. B* **2003**, *20*, 554–559. [66](#)
- [132] Wörmke, S.; Mackowski, S.; Brotsudarmo, T. H. P.; Jung, C.; Zumbusch, A.; Ehrl, M.; Scheer, H.; Hofmann, E.; Hiller, R. G.; Bräuchle, C. *Biochim. Biophys. Acta* **2007**, *1767*, 956–964. [69](#), [70](#), [99](#), [108](#)
- [133] Lu, H. P.; Xie, X. S. *Nature* **1997**, *385*, 143 – 146. [71](#)
- [134] Bout, D. A. V.; Yip, W.-T.; Hu, D.; Fu, D.-K.; Swager, T. M.; Barbara, P. F. *Science* **1997**, *277*, 1074 – 1077.
- [135] Blum, C.; Stracke, F.; Becker, S.; Mullen, K.; Meixner, A. *J. Phys. Chem. A* **2001**, *105*, 6983–6990. [71](#)
- [136] Frauenfelder, H. The Complexity of Proteins. In *Physics of Biological Systems: From Molecules to Species, Lecture Notes in Physics*; Springer-Verlag: Heidelberg, Germany, 2003; pp 29–60. [71](#)
- [137] Valkunas, L.; Janusonisa, J.; Rutkauskas, D.; van Grondelle, R. *J. Lumin.* **2007**, *127*, 269–275. [71](#), [72](#)
- [138] Spezia, R.; Aschi, M.; Nola, A. D.; Valentin, M. D.; Carbonera, D.; Amadei, A. *Biophys. J.* **2003**, *84*, 2805–2813. [72](#)
- [139] Wörmke, S.; Mackowski, S.; Brotsudarmo, T. H. P.; Bräuchle, C.; Garcia, A.; Braun, P.; Scheer, H.; Hofmann, E. *Appl. Phys. Lett.* **2007**, *90*, 193901. [72](#), [108](#)
- [140] Mackowski, S.; Wörmke, S.; Brotsudarmo, T. H. P.; Jung, C.; Hiller, R. G.; Scheer, H.; Bräuchle, C. *Biophys. J.* **2007**, *93*, 3249–3258. [78](#), [79](#), [99](#), [100](#), [104](#), [108](#)
- [141] Knox, R. S. *Photochem. Photobiol.* **2003**, *77*, 492–496. [81](#)
- [142] Zehetmayer, P.; Kupka, M.; Scheer, H.; Zumbusch, A. *Biochim. Biophys. Acta* **2004**, *1608*, 35–44. [86](#)
- [143] Matsumoto, M.; Nishimura, T. *ACM Trans. Model. Comput. Simul.* **1998**, *8*, 3–30. [86](#)

- [144] Elghanian, R.; Storhoff, J. J.; Mucic, R. C.; Letsinger, R. L.; Mirkin, C. A. *Science* **1997**, *277*, 1078–1081. [89](#)
- [145] Link, S.; El-Sayed, M. J. *Phys. Chem. B* **1999**, *103*, 8410–8426. [90](#), [91](#)
- [146] Dubertret, B.; Calame, M.; Libchaber, A. J. *Nature Biotechnol.* **2001**, *19*, 365 – 370.
- [147] Barnes, W. L.; Dereux, A.; Ebbesen, T. W. *Nature* **2003**, *424*, 824–830.
- [148] Kelly, K.; Coronado, E.; Zhao, L.; Schatz, G. J. *Phys. Chem. B* **2003**, *107*, 668–677. [90](#)
- [149] Ozbay, E. *Science* **2006**, *311*, 189–193.
- [150] Lakowicz, J. R. *Plasmonics* **2006**, *1*, 5–33.
- [151] Slocik, J. M.; Tam, F.; Halas, N. J.; Naik, R. R. *Nano Letters* **2007**, *7*, 1054–1058. [89](#)
- [152] Kulakovich, O.; Strekal, N.; Yaroshevich, A.; Maskevich, S.; Gaponenko, S.; Nabiev, I.; Woggon, U.; Artemyev, M. *Nano Letters* **2002**, *2*, 1449–1452. [89](#), [94](#), [98](#)
- [153] Shimizu, K. T.; Woo, W. K.; Fisher, B. R.; Eisler, H. J.; Bawendi, M. G. *Phys. Rev. Lett.* **2002**, *89*, 117401. [98](#)
- [154] Farahani, J. N.; Pohl, D. W.; Eisler, H.-J.; Hecht, B. *Phys. Rev. Lett.* **2005**, *95*, 017402.
- [155] Lee, J.; Javed, T.; Skeini, T.; Govorov, A. O.; Bryant, G. W.; Kotov, N. A. *Angew. Chem., Int. Ed.* **2006**, *45*, 4819 – 4823.
- [156] Govorov, A. O.; Bryant, G. W.; Zhang, W.; Skeini, T.; Lee, J.; Kotov, N. A.; Slocik, J. M.; Naik, R. R. *Nano Letters* **2006**, *6*, 984–994. [105](#)
- [157] Pons, T.; Medintz, I.; Sapsford, K.; Higashiya, S.; Grimes, A.; English, D.; Mattoussi, H. *Nano Letters* **2007**, *7*, 3157–3164. [89](#)
- [158] Liu, G. L.; Yin, Y.; Kunchakarra, S.; Mukherjee, B.; Gerion, D.; Jett, S. D.; Bear, D. G.; Gray, J. W.; Alivisatos, A. P.; Lee, L. P.; Chen, F. F. *Nature Nanotechnol.* **2006**, *1*, 47–52, 10.1038/nnano.2006.51. [89](#)
- [159] Chen, Y.; Munechika, K.; Ginger, D. S. *Nano Letters* **2007**, *7*, 690–696.
- [160] Muskens, O. L.; Giannini, V.; Sanchez-Gil, J. A.; Rivas, J. G. *Nano Letters* **2007**, *7*, 2871–2875.
- [161] Dulkeith, E.; Ringler, M.; Klar, T. A.; Feldmann, J.; Javier, A. M.; Parak, W. J. *Nano Letters* **2005**, *5*, 585–589.
- [162] Kuhn, S.; Hakanson, U.; Rogobete, L.; Sandoghdar, V. *Phys. Rev. Lett.* **2006**, *97*, 017402.
- [163] Gerber, S.; Reil, F.; Hohenester, U.; Schlagenhaufen, T.; Krenn, J. R.; Leitner, A. *Phys. Rev. B (Condensed Matter and Materials Physics)* **2007**, *75*, 073404. [89](#)
- [164] Schlipper, R.; Kusche, R.; von Issendorff, B.; Haberland, H. *Phys. Rev. Lett.* **1998**, *80*, 1194–1197. [90](#)
- [165] Hagino, K. *Phys. Rev. B* **1999**, *60*, R2197–R2199. [90](#)
- [166] Mie, G. *Annalen der Physik* **1908**, *25*, 377–445. [90](#)
- [167] Born, M.; Wolf, E. *Principles of Optics*; Pergamonn Press, Oxford, 1998. [90](#), [91](#)

- [168] Kreibig, U.; Vollmer, M. *Optical Properties of Metal Clusters, Springer Series in Materials Science*; Springer, Berlin, 1995. [91](#), [92](#)
- [169] Link, S.; El-Sayed, M. A. *Annu. Rev. Phys. Chem.* **2003**, *54*, 331–366. [91](#), [92](#)
- [170] Hao, E.; Schatz, G. C. *J. Chem. Phys.* **2004**, *120*, 357–366. [92](#)
- [171] Dulkeith, E. Ph.D. thesis, LMU München: Faculty of Physics, 2004. [92](#), [97](#)
- [172] Bharadwaj, P.; Novotny, L. *Opt. Express* **2007**, *15*, 14266–14274. [92](#), [94](#), [98](#)
- [173] Lakowicz, J. R.; Gryczynski, Z.; Shen, I.; Malicka, Y.; Auria, J. D.; S., S.; Gryczynski, Z. In *Fluorescence Spectral Engineering - Biophysical and Biomedical Applications*; Kraayenhof, R., Ed.; Springer, 2002; Vol. 2, Chapter 2, pp 43–68. [94](#), [103](#)
- [174] Aussenegg, F.; Leitner, A.; Lippitsch, M.; Reinisch, H.; Riegler, M. *Surface Science* **1987**, *189-190*, 935–945, Proceedings of the Ninth European Conference on Surface Science. [94](#), [95](#), [97](#)
- [175] Ford, G. W.; Weber, W. H. *Physics Reports* **1984**, *113*, 195–287. [96](#), [97](#)
- [176] Moskovits, M. *Rev. Mod. Phys.* **1985**, *57*, 783–826.
- [177] Klimov, V. V.; Ducloy, M.; Letokhov, V. S. *Quantum Electron* **2001**, *31*, 569–586. [96](#)
- [178] Gersten, J.; Nitzan, A. *J. Chem. Phys.* **1981**, *75*, 1139–1152. [97](#), [98](#)
- [179] Chance, R.; Prock, A.; Silbey, R. Molecular fluorescence and energy transfer near interfaces. *Adv. Chem. Phys.*, 1978. [97](#)
- [180] Wokaun, A.; Bergman, J. G.; Heritage, J. P.; Glass, A. M.; Liao, P. F.; Olson, D. H. *Phys. Rev. B* **1981**, *24*, 849–856. [97](#)
- [181] Lakowicz, J. R.; Shen, Y.; D'Auria, S.; Malicka, J.; Fang, J.; Gryczynski, Z.; Gryczynski, I. *Anal. Biochem.* **2002**, *301*, 261–277. [98](#), [103](#), [104](#), [105](#)
- [182] Sokolov, K.; Chumanov, G.; Cotton, T. *Anal. Chem.* **1998**, *70*, 3898–3905. [98](#)
- [183] Wokaun, A. *Mol. Phys.* **1985**, *56*, 1–33. [100](#)
- [184] Mackowski, S.; Wörmke, S.; Maier, A.; Brotosudarmo, T.; Harutyunyan, H.; Hartschuh, A.; Govorov, A.; Scheer, H.; Bräuchle, C. *Nano Letters* **2008**, *8*, 558–564. [105](#), [106](#), [109](#)
- [185] Mackowski, S.; Wörmke, S.; Brotosudarmo, T. H. P.; Scheer, H.; Bräuchle, C. *Photosynth. Res.* **2008**, *95*, 253–260. [108](#)
- [186] Wörmke, S.; Mackowski, S.; Schaller, A.; Brotosudarmo, T.; Johanning, S.; Scheer, H.; Bräuchle, C. *J. Fluoresc.* **2008**. [109](#)



# APPENDIX A

---

## Miscellaneous

---

### A.1 Source Code

#### A.1.1 Förster Energy Transfer

Source code of calculation of Förster energy transfer rates written in Matlab.

```
%% CALCULATION OF TRANSFER RATES
% using interpolated data

% parameters needed by Förster Theory

%% constants
K=0.155236;           % kappa square
n=1.6;                % index of refraction
r=17.4;               % distance between chromophores
NA=6.022*10^(23);    % Avogadro number

%% donor: Chl a
q=0.24;               % quantum yield
tau=3.6*10^(-9);     % lifetime

% normalize emission to area unity
x=linspace(600,750,151)';
emData=load('em_PCPa.dat');
em=1/trapz(x,emData(:,2)).*emData(:,2);

%% acceptor: acChl a
epsilon=65.2e3;       % extinction coefficient
% absorption spectrum
```

```

absData=load('abs_PCPaca.dat');

% scale absorption to extinction coefficient in max
abs_scale=epsilon/max(absData(:,2));
abs=abs_scale.*absData(:,2);

%% calculation of overlap integral
overlap=em.*abs.*x.^4;
%overlapInt=quadl(overlap,650,750);
overlapInt=trapz(x,overlap);

% calculation of transfer rate
R0=0.2108*((K*q)/(n^4)*overlapInt)^(1/6);
transferRate=1/tau*(R0/r)^6;

hold on
plot(x,abs)
plot(x,em)
hold off

%% speichern
save('et_AAcA.dat', 'overlapInt', 'R0', 'transferRate', '-ascii');

```

### A.1.2 Monte Carlo Simulation

Source code of Monte-Carlo simulations written in Python.

```

## Monte Carlo Simulation of Energy Distribution
# Chlorophylls only
#

# Energy Transfer Rates in 1/ps
kAB = 0.038401252
kBA = 0.027183122

# inverse Fluorescence lifetimes in ps
kA = 1/3.6e3
kB = 1/3.86e3

# first round
# Counter of Relaxation on Zero
a=0
b=0

```

```
# Use the Mersenne twister generator, with the
# default initial state used by Nishimura and Matsumoto:
import random
random.seed(5489)

while a+b < 1000000:
    kA_tot = kAB + kA          # excitation on A
    x = random.random()*kA_tot
    if x <= kAB:
        kB_tot = kBA+kB
        x=random.random()*kB_tot
        if x > kBA:          # excitation on B
            b=b+1
        else:
            a=a+1
    print a
```

## A.2 List of Publications

1. Wörmke, S.; Mackowski, S.; Scheer, H. and Bräuchle, C. *Nachrichten der Chemie*, **2008**, in press
2. Mackowski, S.; Wörmke, S.; Ehrl, M. and Bräuchle, C.: Low-Temperature Spectral Dynamics of Single TDI Molecules in n-Alkane Matrixes. *J. Fluoresc.*, **2008**, 18, 625-631
3. Wörmke, S.; Mackowski, S.; Schaller, A.; Brotosudarmo, T.; Johanning, S.; Scheer, H. and Bräuchle, C.: Single Molecule Fluorescence of Native and Refolded Peridinin-Chlorophyll-Protein Complexes. *J. Fluoresc.*, **2008**, 18, 611-617
4. Wörmke, S.; Mackowski, S.; Scheer, H. and Bräuchle, C.: Solarzellen der Zukunft nach biologischem Vorbild? *Physik in unserer Zeit*, **2008**, 3, 113-114
5. Mackowski, S.; Wörmke, S.; Maier, A.; Brotosudarmo, T.; Harutyunyan, H.; Hartschuh, A.; Govorov, A.; Scheer, H. and Bräuchle, C.: Metal-Enhanced Fluorescence of Chlorophylls in Single Light-Harvesting Complexes. *Nano Letters*, 45701, **2008**, 8, 558-564
6. Mackowski, S.; Wörmke, S.; Brotosudarmo, T. H. P.; Scheer, H. and Bräuchle, C.: Fluorescence spectroscopy of reconstituted peridinin-chlorophyll-protein complexes. *Photosynth. Res.*, **2008**, 95, 253-260
7. Mackowski, S.; Wörmke, S.; Brotosudarmo, T. H. P.; Jung, C.; Hiller, R. G.; Scheer, H. and Bräuchle, C.: Energy transfer in reconstituted peridinin-chlorophyll-protein complexes: ensemble and single-molecule spectroscopy studies. *Biophys. J.*, **2007**, 93, 3249-3258
8. Wörmke, S.; Mackowski, S.; Brotosudarmo, T. H. P.; Jung, C.; Zumbusch, A.; Ehrl, M.; Scheer, H.; Hofmann, E.; Hiller, R. G. and Bräuchle, C.: Monitoring fluorescence of

- individual chromophores in peridinin-chlorophyll-protein complex using single molecule spectroscopy. *Biochim. Biophys. Acta.*, **2007**, 1767, 956-964
9. Wörmke, S.; Mackowski, S.; Brotosudarmo, T. H. P.; Bräuchle, C.; Garcia, A.; Braun, P.; Scheer, H. and Hofmann, E.: Detection of single biomolecule fluorescence excited through energy transfer: Application to light-harvesting complexes. *Applied Physics Letters*, **2007**, 90, 193901
  10. Brotosudarmo, T. H. P.; Hofmann, E.; Hiller, R. G.; Wörmke, S.; Mackowski, S.; Zumbusch, A.; Bräuchle, C. and Scheer, H. Peridinin-chlorophyll-protein reconstituted with chlorophyll mixtures: preparation, bulk and single molecule spectroscopy. *FEBS Lett.*, **2006**, 580, 5257-5262
  11. Wörmke, S.; Brendel, K.; Andresen, U. and Mäder, H.: A molecular beam Fourier transform microwave study of 2-methylpyridine and its complex with argon: structure, methyl internal rotation and  $^{14}\text{N}$  nuclear quadrupole coupling. *Molecular Physics*, **2004**, 102, 1625-1639
  12. Perrin, A.; Flaud, L.; Demaison, J.; Mäder, H. and Wörmke, S.: Microwave and Submillimeter-Wave Measurements of  $\text{HD}_{12}\text{C}_{16}\text{O}$  in the  $\nu_4$ ,  $\nu_5$ , and  $\nu_6$  Bands: Evidence of Vibrational Induced Rotational Axis Switching ("VIRAS"). *Journal of Molecular Spectroscopy*, **2002**, 216, 214-224

### A.3 Contributions to Conferences and Seminars

(Authored and co-authored)

- S. Wörmke, S. Mackowski, A. Maier, T. Brotosudarmo, H. Harutyunyan, A. Hartschuh, A. Govorov, H. Scheer, and C. Bräuchle: *Metal-enhanced fluorescence of chlorophylls in single light-harvesting complexes*, Poster presentation at NIM-workshop on "Interactions in Hybrid Nanosystems", Frauenwörth, Chiemsee, May 1st-4th, 2008
- S. Mackowski, S. Wörmke, A. Maier, T. Brotosudarmo, H. Harutyunyan, A. Hartschuh, A. Govorov, H. Scheer, and C. Bräuchle: *Metal-enhanced fluorescence of chlorophylls in single light-harvesting complexes*, Oral presentation at "DPG-Frühjahrstagung", Berlin, February 25th-29th, 2008
- S. Wörmke: *Single Molecule Spectroscopy of peridinin chlorophyll protein (PCP) reconstituted with various chlorophyll mixtures*, Oral presentation at "Physikalisch-Chemisches Kolloquium", LMU, January 30th, 2008
- S. Mackowski, S. Wörmke, T. Brotosudarmo, E. Hofmann, R. Hiller, H. Scheer and C. Bräuchle: *Single molecule spectroscopy of peridinin-chlorophyll-protein complex*, Oral presentation at "Light-Induced Dynamics of Proteins", SFB 533, Freising, September 30th- October 5th, 2007
- T. Brotosudarmo, S. Mackowski, S. Wörmke, E. Hofmann, R. Hiller, C. Bräuchle and H. Scheer: *Modified Peridinin-Chlorophyll-Proteins: Heterochlorophyllous reconstitution and*

*binding affinities*, Poster presentation at "Light-Induced Dynamics of Proteins", SFB 533, Freising, September 30th - October 5th, 2007

- S. Mackowski, S. Wörmke, M. Ehrl and C. Bräuchle: *Low-temperature spectral dynamics of single TDI molecules in alkane matrixes*, Poster presentation at "Light-Induced Dynamics of Proteins", SFB 533, Freising, September 30th - October 5th, 2007
- S. Wörmke, S. Mackowski, T. Brotsudarmo, H. Scheer and C. Bräuchle: *Energy transfer in peridinin-chlorophyll-protein reconstituted with chlorophyll mixtures*, Poster presentation at "Light-Induced Dynamics of Proteins", SFB 533, Freising, September 30th - October 5th, 2007
- S. Wörmke, S. Mackowski, T. Brotsudarmo, H. Scheer, and C. Bräuchle: *Single Molecule Spectroscopy of Peridinin-Chlorophyll-Protein Complex Reconstituted with Chlorophyll Mixtures*, Poster presentation at the 10th Conference on "Methods and Applications of Fluorescence: Spectroscopy, Imaging and Probes", Salzburg, Austria, September 9th-12th, 2007
- S. Mackowski, S. Wörmke and C. Bräuchle: *Low-Temperature Spectral Dynamics of Single TDI Molecules in Alkane Matrixes*, Poster presentation at the 10th Conference on "Methods and Applications of Fluorescence: Spectroscopy, Imaging and Probes", Salzburg, Austria, September 9th-12th, 2007
- S. Mackowski, S. Wörmke, T. Brotsudarmo, R Hiller, H. Scheer and C. Bräuchle: *Single Molecule Studies of Energy Transfer in Peridinin-Chlorophyll-Protein Reconstituted with Hetero-Chlorophyllous Mixtures*, Poster presentation at "14th International Congress on Photosynthesis: Satellite Workshop on Photosynthetic Light-Harvesting Systems", Drymen, Scotland, UK, July 18th-21st, 2007
- T. Brotsudarmo, S. Mackowski, S. Wörmke, E. Hofmann, R.G. Hiller, C. Bräuchle and H. Scheer: *Modified Peridinin-Chlorophyll-Proteins: Heterochlorophyllous Reconstitution and Binding Affinities*, Poster presentation at "14th International Congress on Photosynthesis: Satellite Workshop on Photosynthetic Light-Harvesting Systems", Drymen, Scotland, UK, July 18th-21st, 2007
- H. Scheer, T. Brotsudarmo, S. Mackowski, S. Wörmke, E. Hofmann, R. Hiller and C. Bräuchle: *Binding Affinities of Chlorophylls in Hetero-Chlorophyllous Complexes of Peridinin-Chlorophyll-Protein as Revealed by Ensemble and Single Molecule Spectroscopy*, Oral presentation at "14th International Congress on Photosynthesis", Glasgow, Scotland, UK, July 22nd-27th, 2007
- S. Mackowski, S. Wörmke, M. Ehrl and C. Bräuchle: *Low-Temperature Spectral Dynamics of Single TDI Molecules in Alkane Matrixes*, Oral presentation at "DPG - Frühjahrstagung", Regensburg, March 26th-30th, 2007
- S. Wörmke, S. Mackowski, T. Brotsudarmo, C. Bräuchle, H. Scheer, E. Hofmann, *Fluorescence Spectroscopy of Single Peridinin-Chlorophyll a-Protein Light-Harvesting Complexes*, Oral presentation at "DPG-Frühjahrstagung", Regensburg, March 26th-30th, 2007
- S. Mackowski, S. Wörmke, T. Brotsudarmo, C. Bräuchle, H. Scheer, E. Hofmann, A. Zumbusch, *Fluorescence Spectroscopy of Single Peridinin-Chlorophyll a-Protein Light-*

*Harvesting Complexes*, Oral presentation at the conference "Light Harvesting Processes", Kloster Banz, March 21st-24th, 2007

- S. Wörmke, S. Mackowski, T. Brotsudarmo, E. Hofmann, H. Scheer and C. Bräuchle: *Single Molecule Spectroscopy of Peridinin-Chlorophyll- Protein Light-Harvesting Complexes Reconstituted with Various Chlorophyll Mixtures*, Poster presentation at the conference "Light Harvesting Processes", Kloster Banz, March 21st-24th, 2007
- S. Mackowski, S. Wörmke, C. Jung, M. Ehrl, A. Zumbusch, C. Bräuchle, T. Brotsudarmo, H. Scheer, E. Hofmann, *Single Molecule Spectroscopy of Wild Type and Reconstituted Peridinin-Chlorophyll-Protein Complexes*, Oral presentation at "DPG-Frühjahrstagung", Dresden, March 26th-31st, 2006

## A.4 Lebenslauf

### **Persönliche Daten**

---

Name	Stephan Wörmke
Geburtsdatum	24. Juni 1976
Geburtsort	Flensburg

### **Schulbildung**

---

06/1996	Allgemeine Hochschulreife Goethe-Schule, Gymnasium der Stadt Flensburg
---------	---

### **Studium an der Christian-Albrechts-Universität zu Kiel**

---

10/1997 - 10/2003	Physik (Diplom)
10/2002 - 10/2003	Diplomarbeit "Mikrowellen Spektroskopische Untersuchungen am 2-Methyl-Pyridin und seinem Komplex mit Argon"

### **Auslandsstudium**

---

08/2001 - 05/2002	Royal Institute of Technology (KTH), Stockholm (Schweden)
06/2005	Technisches Lizenziat (Tekn. Lic.) Schwedischer Abschluß zwischen Master und Doktor in Technischer Physik

### **Promotion an der Ludwig-Maximilians-Universität München**

---

seit 04/2004	wissenschaftlicher Mitarbeiter am LS Prof. Dr. Ch. Bräuchle (Physikalische Chemie), Bearbeitung des vorliegenden Themas
--------------	---

---

## Danksagung

---

Am Ende dieser Arbeit möchte ich die Chance nutzen, all denjenigen zu danken, die mich auf dem Weg hierher begleitet haben. Das sind insbesondere all meine Lehrer, die mir den Blick auf eine faszinierende Welt ermöglichten, die sich durch die Beschäftigung mit der Wissenschaft eröffnet.

Ich danke Herrn Prof. Dr. C. Bräuchle für die Chance in seiner Arbeitsgruppe und dem außergewöhnlichen Forschungsumfeld, daß er in Großhadern geschaffen hat, ein spannendes Thema bearbeiten zu können. Nicht genug danken kann ich dabei Dr. Sebastian Mackowski, der mich als Betreuer und Freund begleitet hat und mir kritisch, aber auch herzlich, das Handwerk der wissenschaftlichen Arbeit beigebracht hat. Ich danke Herrn Prof. Dr. H. Scheer für die wunderbare Kooperation im SFB 533 und die spannenden Fragestellungen rund um PCP, die das Fundament dieser Arbeit darstellen. Tatas Brotosudarmo danke ich für die grandiose Arbeit, die hinter den Rekonstitutionen des PCP verborgen ist.

Aus dem AK Bräuchle danke ich weiterhin Moritz Ehrl, der stets an mich geglaubt hat, auch als die Zeiten einmal schwierig waren. Ebenso Prof. Dr. A. Zumbusch, der mich von dem PCP-Projekt überzeugte. So vielen anderen ist noch zu danken für wissenschaftliche, aber auch unwissenschaftliche Diskussionen oder einfach nur ein angenehmes Klima: Peter Schlüsche, Ralf Bausinger, John Briggs, Johanna Kirstein, Christophe Jung, Karla de Bruin, Alexandra Scherer, Peter Schwaderer, Robert Lewis, Timo Lebold, Christian Hellriegel und vielen anderen.

Ich danke insbesondere meinen Freunden Pem und Lydia, Javi und Conxita und vielen anderen für ihre Freundschaft, die mir immer den nötigen Rückhalt gegeben hat. Für einen Flensburger im fernen bayrischen Süden ist es wichtig immer wieder einmal tief Luft zu holen. Die Besuche am Meer bei meiner Familie, meinen Eltern und meiner Großmutter, halfen dabei sehr und ich danke euch, daß ihr mich zu jeder Zeit meines Weges unterstützt habt.